EPI MRI OF SKELETAL MUSCLE
FOLLOWING EXERCISE

ECHO PLANAR MAGNETIC RESONANCE IMAGING OF SKELETAL MUSCLE FOLLOWING EXERCISE

By

ANDREW D. DAVIS, B.Sc., M.Sc.

A Thesis
Submitted to the School of
Graduate Studies
in Partial Fulfilment of the Requirements
for the Degree
Doctor of Philosophy

McMaster University

Doctor of Philosophy (2018) McMaster University
(Radiation Sciences – Medical Physics) Hamilton, Ontario, Canada

TITLE:	Echo Planar Magnetic Resonance Imaging of Skeletal Muscle Following Exercise
AUTHOR:	Andrew D. Davis B.Sc. (Honours, Physics), Brock University, Canada M.Sc. (Medical Physics), McMaster University, Canada
SUPERVISOR:	Michael D. Noseworthy, Ph.D., LEL
NUMBER OF PAGES:	xvi, 171

Lay Abstract

Adequate blood circulation to muscles is important for good health. Researchers have used magnetic resonance imaging (MRI) techniques to assess blood and oxygen supply to muscles. The work in this thesis improves upon the analysis methods in prior work, especially in the areas of motion correction of the images and selection of individual muscle regions for analysis.

Previous techniques could sometimes make motion in muscle images worse. This work provides valuable motion and distortion correction for muscle imaging, ensuring that measurements truly reflect muscle physiology. It also describes a method to remove an unwanted signal from post-exercise muscle data, and create a map of the internal muscle motion that occurred.

Finally, an advanced mathematical technique was used to extract signals of interest and important spatial features from muscle image data automatically. The technique produced reliable results within and among subjects.

Abstract

In recent years, researchers have increasingly used magnetic resonance imaging (MRI) to study temporal skeletal muscle changes using gradient echo (GRE) echo planar imaging (EPI). These studies, typically involving exercise or ischemic challenges, have differentiated healthy subjects from athletic or unhealthy populations, such as those with peripheral vascular disease. However, the analysis methodologies have been lacking.

In this thesis, two sessions of post-exercise GRE EPI data were collected from six subjects' lower legs using a 3 Tesla MRI scanner and a custom built ergometer. Past studies used common medical imaging software for motion correction. This work shows that such tools degrade leg image data by introducing motion, increasing root mean squared error in rest data by 22%. A new approach decreased it by 12%. EPI distortion correction in muscle images was also achieved, with the correlation ratio of functional and structural images increasing by up to 8%.

In addition, a brief but intense artifact in GRE EPI muscle images results from muscle tissue moving in and out of the imaged volume. This through-plane artifact was successfully modelled as a mono-exponential decay for regression analysis, increasing the utility of the residual signal. The regression parameters were also leveraged to produce muscle displacement maps, identifying 44% of voxels as displaced. The maps were validated in a motion phantom and in-vivo using ultrasound.

Finally, independent component analysis (ICA) was applied to post-exercise GRE EPI images to detect features in a data-driven, multivariate way and improve on conventional ROI selection methods. ICA produced parametric maps that were spatially correlated to working muscles from every trial (most with $|R| > 0.4$). The components were also separated from the susceptibility, motion, and blood vessel signals, and temporally reliable within individuals.

These methodological advances represent increased rigour in the analysis of muscle GRE EPI images.

Preface and Acknowledgements

The following document is submitted for consideration as a thesis. It has three research chapters, in the *sandwich* style. The three research chapters all have as their authors myself (A.D.), and Dr. Michael D. Noseworthy, my Ph.D. supervisor. In contributing to the work, Dr. Noseworthy made significant contributions to the conception and design of experiments, the revising of manuscripts and final approval for publication of papers. My contributions were in conception and design of the experiments, acquisition, analysis and interpretation of data, preparation of figures, and drafting and revising the article content.

I owe a debt of gratitude to many people for the help and support I've received in completing my studies. My supervisor, Dr. Michael Noseworthy, played a crucial role in this process, of course. His guidance allowed me to acquire valuable imaging knowledge and research skills. My committee members are also thanked for their time and advice: Dr. Nicholas Bock, Dr. Dinesh Kumbhare, Dr. Thomas Farrell, Dr. Michael Patterson, and Dr. Stuart Phillips. Dr. Conrad Rockel played a key role in helping modify the ergometer and acquire data. Dr. Bareket Falk and Mr. Raffy Dotan deserve many thanks for help in designing and building the ergometer, and advising on its use. I would like to thank all the members of the IRC at St Joseph's Healthcare Hamilton and friends in the Medical Physics department for companionship and useful discussions (Mr. Norm Konyer, Dr. Alexander Weber, Mr. Evan McNabb, Dr. Olga Dona Lemus, Mr. Benjamin Geraghty, Mr. Steve Madison, Dr. Mohammed Ali Warsi, Dr. Alyaa Elzibak, Dr. Oi Lei Wong, Dr. Sergei Obruchkov, Dr. Ali Fatemi, Mr. Aravinthan Jegatheesan, Mr. Michael Chamberlain, Dr. Graeme Wardlaw, Dr. Baochang Liu), especially those who volunteered their time (and legs) in service of this work. I would also like to thank the administrators of the Medical Physics and Applied Radiation Sciences department, and the MRI technologists in the IRC, who were instrumental to this work: Dr. Fiona McNeill, Mrs. Fiona Ahlang, Mrs. Cheryl Contant, Mrs. Julie Lecomte, Mrs. Carol Awde, Mrs. Toni Cormier and Mrs. Janet Burr. Finally, this thesis would not have been possible without the support of my wife, Mollie, and my parents, Jack and Claire. My sons, Owen and Eric, must also be acknowledged for bringing so much joy.

Contents

List of Figures

List of Tables

Abbreviations and Symbols

1RM	one repetition maximum. 35, 79, 80, 91, 106, 110
2D	two dimensional. 4, 58, 72, 95
3D	three dimensional. 56, 72
4D	four dimensional (space + time). 72

α	flip angle of RF excitation pulse. 57, 80, 92, 107
AP	anterior-posterior. 123–125

BASH	Bourne-again shell. 82, 107
BIC	Bayesian information criterion. 17, 18
BMI	body mass index. 106, 110
B_0	static magnetic field of the MRI scanner. 2, 3, 54–57, 61, 63, 67, 68, 80–82, 107, 126, 130
BOLD	blood oxygenation level dependent. 1, 2, 4–8, 12, 20, 23, 34–37, 54, 57, 75, 77, 80, 103–106, 121, 130, 132, 166
BSS	blind source separation. 28, 36, 106, 129
BV	blood volume. 7, 12, 19–22

CR	correlation ratio. 60, 61, 63, 64, 68
CSA	cross sectional area. 10

DA	deep aponeuroses of the triceps surae; see Fig. 3.3. 9, 82–84, 86–90
DTI	diffusion tensor imaging. 56, 105

EM	extensor digitorum and hallucis longus muscles; see Fig. 3.3. 83, 86, 87, 89
EPI	echo planar imaging. 4–7, 34–37, 53–61, 63, 67, 68, 77, 78, 80–82, 87, 90–93, 95, 103, 105, 107, 108, 110, 114, 126, 127, 129, 130, 163–166, 169

FA	factor analysis. 26–29, 32
FATSAT	chemical fat saturation. 80
FFS	feet-first supine. 81
fMRI	functional magnetic resonance imaging. 4, 23, 25, 27, 28, 31, 32, 36, 104, 106, 128, 165, 168
FOV	field of view. 57, 72, 80, 90, 107, 131
FSPGR	fast spoiled gradient echo. 57, 80, 81
FWHM	full width at half maximum. 82, 107
GLM	general linear model. 23
GM	gastrocnemius muscle; see Fig. 3.3. 9–12, 36, 107, 110, 111, 119, 121, 123, 126–129
GRE	gradient echo. 3, 4, 6, 7, 34–37, 53–57, 59–61, 63, 67, 77, 78, 80–82, 87, 90–92, 95, 103, 105, 107–109, 114, 126, 127, 129, 163–166, 169
Hb	hemoglobin. 20
[Hb]	hemoglobin concentration. 18, 20–22
HHb	deoxy-hemoglobin. 4, 19, 21, 104, 121, 130
HMb	deoxy-myoglobin. 19, 20
IC	independent component. 114, 119, 121, 127
ICA	independent component analysis. 28–35, 37, 38, 106–109, 111–113, 122, 128, 129, 131–133, 165–167
ICC	intraclass correlation coefficient. 111
LDF	laser doppler flowmetry. 168
LGM	lateral gastrocnemius muscle; see Fig. 3.3. 9, 11, 83, 86, 89
LR	left-right. 123–125
Mb	myoglobin. 20, 21
[Mb]	myoglobin concentration. 20
mfMRI	muscle functional magnetic resonance imaging. 6
MGM	medial gastrocnemius muscle; see Fig. 3.3. 9, 36, 83–86, 89, 90
MR	magnetic resonance. 1–3, 7, 9, 55, 56, 80, 92, 106
MRI	magnetic resonance imaging. 1, 2, 9, 10, 13, 34, 53, 77, 79, 81, 88, 95, 104, 164
MRS	magnetic resonance spectroscopy. 20

MS	matrix size. 57, 80, 107
MVC	maximum voluntary contraction. 16, 19
MVU	miscrovascular unit. 14, 15
NIRS	near-infrared spectroscopy. 6, 7, 18–22, 36, 129, 130, 166
O_2Hb	oxy-hemoglobin. 4, 19
O_2Mb	oxy-myoglobin. 19, 20
PC	phase contrast. 9, 10
PCA	principal component analysis. 23–36, 107, 131, 133, 134
PCC	Pearson correlation coefficient. 112, 114, 119, 123–125
PET	positron emission tomography. 20
PF	plantar flexion. 6, 8, 10, 11, 17, 19, 21, 77–79, 88–90, 105, 106, 119, 121
PICA	probabilistic independent component analysis. 29, 30, 37, 107–109, 111, 121, 126, 129–132, 165, 166
PM	peroneus longus and brevis muscles; see Fig. 3.3. 83, 90, 119
PO_2	partial pressure of oxygen. 20
PPCA	probabilistic principal component analysis. 30
PSD	power spectral density. 60, 62, 63, 66, 72
PVD	peripheral vascular disease. 163, 165
RAM	random access memory. 59, 66
RBC	red blood cells. 14, 15
rBW	bandwidth of receive radio-frequency coil. 57, 80, 107
RF	radio-frequency. xii, 2–5, 56, 95
RMSE	root mean squared error. 59–61, 64, 65
$RMSE_G$	global root mean squared error. 62, 65
ROI	region of interest. 8, 35, 36, 56, 61, 82–84, 86, 87, 101, 105, 107–110, 112, 114, 116, 121, 126, 128, 129, 131, 133, 164, 165, 167
S_{aO_2}	arterial oxygen saturation. 18, 22
SD	standard deviation. 63, 64, 68, 86, 123, 127
SE	standard error. 11, 95

SICA	spatial independent component analysis. 29
SM	soleus muscle; see Fig. 3.3. 9, 11, 12, 36, 83, 84, 86, 89, 90, 107, 111, 121, 123, 126, 128, 129
S_{mO_2}	muscle oxygen saturation. 6, 7, 18, 19, 22
ΔS_{mO_2}	relative muscle oxygen saturation. 19
SNR	signal-to-noise ratio. 105
ST	spin tagging. 9, 10
SVD	singular value decomposition. 25–27, 29
S_{vO_2}	venous oxygen saturation. 6, 18, 19, 22
T_1	spin-lattice relaxation time constant. 1–3, 13, 60, 68, 75, 77, 80, 81, 105, 122, 131
T_2	spin-spin relaxation time constant. 1–4, 6, 9, 13, 105
T_2^*	measured signal decay time constant. 3, 4, 6, 13, 21, 36, 60, 92, 105, 165
TAM	tibialis anterior muscle; see Fig. 3.3. 83, 84, 86, 87, 89, 90
T_E	echo time. 5, 7, 13, 21, 57, 77, 80, 92, 107
tHb	total hemoglobin. 19
ΔtHb	relative total hemoglobin. 19
TOF	time-of-flight. 55, 61, 64
TPM	tibialis posterior muscle; see Fig. 3.3. 83, 90
T_R	repetition time. 5, 57, 61, 64, 80, 81, 91, 93, 107
TS	triceps surae. 8, 105, 107, 110, 111, 119, 121
VC	Vascular conductance. 16
$\dot{V}O_2$	rate of oxygen consumption. 15, 16, 18, 19

Chapter 1

Introduction

The focus of this thesis is the use of magnetic resonance imaging (MRI) for examining skeletal muscle. This chapter provides background material related to the later research chapters, along with a review of prior research in the field. Each chapter has a self-contained referencing scheme with its own bibliography. Though the research chapters have distinct approaches and analysis schemes, there is some commonality among them, in that all three draw on the same MRI data. The data set is comprised of two repeated sessions of muscle functional imaging data from six subjects. The first research chapter uses data from one session of each subject to detail important considerations in motion and distortion correction of the images. The next chapter uses a short section of data from both sessions of each subject, and adds data from a motion phantom and in-vivo ultrasound imaging to describe a displacement quantification scheme. The third research chapter examines the bulk of the data acquired from each subject using a signal processing analysis strategy. An effort has been made to keep a coherent notation scheme, conforming to standard textbooks. In particular, vector variables are represented in bold typeface.

Core muscle MRI techniques used by clinicians for identifying disease states include T_1, T_2, and proton density-weighted imaging, diffusion imaging, contrast agent enhanced imaging, and various fat-water weighting schemes (Kumar et al., 2016). MR techniques based on muscle function, such as blood oxygenation level dependent (BOLD) imaging and phosphorous spectroscopy, are not routinely used clinically. Yet they show promise for researchers and clinicians examining muscle tissue in health and disease (Tonon et al., 2012; Noseworthy et al., 2010). BOLD imaging, in particular, uses the intrinsic contrast associated with oxygenation and perfusion in tissue to reveal functional changes. This is an alternative to imaging with extrinsic agents such as those containing gadolinium (Gd). Drugs containing Gd are expensive, and carry some risk. Especially in persons with compromised renal function, exposure to Gd can lead to nephrogenic systemic fibrosis (Broome, 2008). However, Gd injections have the advantage of large image contrast changes that follow relatively well characterized behaviours (Galbraith et al., 2002). BOLD imaging, which has been studied extensively in the brain (Buxton, 2009), requires further study before it can be considered clinically useful for muscle disorders (Jacobi et al., 2012). In particular, this thesis details some confounds associated with muscle BOLD imaging that have not previously been described, and their solutions. This leads to a framework for characterizing typical results in healthy individuals. Such work is crucial in order for the muscle BOLD technique to be effectively used in clinical populations.

1.1 T_2^*-weighted imaging techniques

The core material properties that produce contrast in MRI are proton density, T_1, and T_2. The interpretation of proton density contrast is fairly straightforward, deriving from the number of mobile protons in a voxel. T_1 and T_2 are more esoteric MR terms, however, and thus require some explanation. The protons in tissues and solutions under examination with MRI can be thought of as spinning tops, with magnetic moments that precess at the Larmor frequency:

$$\omega_0 = \gamma B_0 \tag{1.1}$$

where B_0 is the magnitude of the externally applied field, usually 1.5 or 3.0 T for clinical MRI systems, and γ is a proportionality constant unique to the isotope under examination called the *gyromagnetic ratio* (Bushberg et al., 2012). Both T_1 and T_2 are time constants associated with the net magnetization of a group of spins following the application of radio-frequency (RF) energy in the MRI scanner. Initially, this magnetization forms in the direction of the main magnetic field of the MR scanner, so $\boldsymbol{M_0} = \boldsymbol{M_z}$. An RF pulse is used to tip the magnetization into the transverse (x-y) plane, creating measurable transverse magnetization, M_{xy}. Spins manipulated by RF in this way are said to be in an excited state. It is important to note that the MR effects of T_1 and T_2 arise from quantum mechanical properties, but that a classical physics picture may be used to describe these properties in MR imaging. This is possible because the classical view correctly describes the behaviour of the average of many spins, and the number of protons that gives rise to the signal in an imaging voxel is very large, on the order of 10^{15} (Buxton, 2009).

T_1, the *spin-lattice* relaxation time constant, refers to the return of energy from excited spins to the surrounding environment. This loss of energy causes a regrowth of the $\boldsymbol{M_z}$ magnetization, according to the following equation:

$$M_z(t) = M_0\,(1 - e^{-t/T_1}) \tag{1.2}$$

where M_0 is the initial magnetic moment before RF is applied (Bushberg et al., 2012). Protons are said to have a *tumbling* rate, which varies depending on their local environment. Environments may be categorized in three types: *free*, as in fluids; *bound* as in the vicinity of large macromolecules; or *structured*, which is an intermediate state. The transfer of the precessional energy of a spin to the environment occurs most efficiently when the tumbling rate of nearby protons is similar to the Larmor frequency (McRobbie et al., 2006). More protons tend to tumble with a frequency close to ω_0 in structured environments than those in either free states or bound states. Therefore protons in these intermediate environments tend to have the shortest T_1, and T_1 depends on B_0.

T_2 is the time constant of the decrease in signal due to loss of phase coherence in the M_{xy} magnetization (Bushberg et al., 2012). This decay is described by the equation:

$$M_{xy}(t) = M_0\,e^{-t/T_2} \tag{1.3}$$

where M_0 is the transverse magnetic moment immediately after the RF pulse. The phase dispersion occurs because of small differences in the local magnetic field environment of spins due to the presence of large molecules organized in structures. Thus T_2 is a property of the local environment, with liquids such as synovial fluid having T_2 values about 20 times longer than muscle tissue, and thus brighter signal on T_2-weighted images (Gold et al., 2004). T_2 does not have a strong dependence on B_0.

T_2^* is a time constant related to T_2. It is measured using gradient echo (GRE) pulse sequences, while T_2 is measured by application of a spin echo sequence. T_2^* is sensitive to subject morphometry and the homogeneity of the magnetic field, which is influenced by shim quality of a particular scanner during data acquisition. These effects are included in the $T_2^{'}$ term of the equation:

$$\frac{1}{T_2^*} = \frac{1}{T_2} + \frac{1}{T_2^{'}} \tag{1.4}$$

The quantity $1/T_2^{'}$ is sometimes expressed as $\gamma \cdot \Delta B_0$ (Haacke et al., 1999). This emphasizes the origin of the term in external background field variations that are sample and scanner dependent, as opposed to the local *spin-spin* interactions that bring about T_2 relaxation. For example, the large difference in susceptibility at the bone-tissue interface of the tibia in the lower leg leads to poor homogeneity of the shim, and faster T_2^* relaxation in the region.

Along with such macroscopic effects as tissue interfaces, T_2^* also varies with perturbations in the magnetic field at smaller scales. In particular, off-resonance effects detectable in GRE images are created by the presence of deoxy-hemoglobin (HHb), which is paramagnetic (i.e. possesses unpaired electrons), unlike oxy-hemoglobin (O_2Hb) (Pauling and Coryell, 1936) which is diamagnetic and has all electrons in pairs. This is the basis of BOLD imaging, which was originally described in rat brains by Ogawa et al. (1990). The technique has come to be used extensively in brain functional magnetic resonance imaging (functional magnetic resonance imaging (fMRI)) to locate areas of increased neural activity during functional tasks.

In principle, a simple approach to BOLD imaging would be to acquire a single volume T_2^*-weighted image from various subjects and look for group differences. The prior discussion should make it clear that this strategy is ill-advised because of the dependency of T_2^* on subject morphometry. Thus, a time series of images is typically acquired under conditions of rest and intervention in order to provide an internal reference and measure relative changes. The images are normally acquired using a single-shot GRE echo planar imaging (EPI) scheme. This method fills two dimensional (2D) k-space, thus acquiring all the data for one imaging slice, after each repetition of the RF pulse. It was first described in the literature as a zigzag through k-space (Mansfield, 1977), and later modified to get a true Cartesian readout (Ljunggren, 1983). EPI has the advantage of acquiring data very quickly

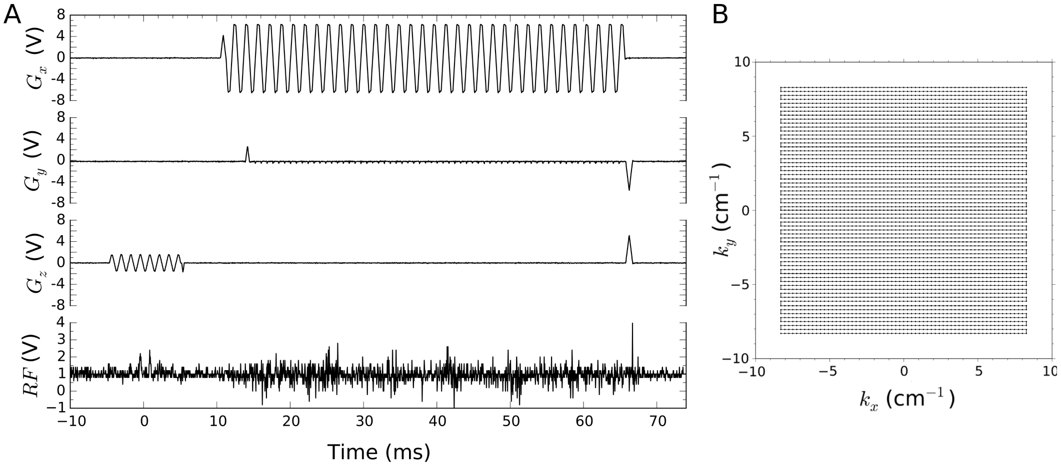

Figure 1.1: Gradient echo echo planar imaging scheme. (**A**) Pulse sequence diagram, recorded using an oscilloscope. Ramp sampling was turned on during the receive portion. A spectral-spatial pulse was used, as indicated by the oscillating G_z gradient. The RF channel recording suffered from low signal-to-noise, but some elements of the imaging pulse are visible near 0 ms. The sub-pulses and the gradient determine spatial (slice) selection, while the envelope of the RF sub-pulses determines spectral selection. The gradient oscillation avoids a spatial offset in the excitation profiles of lipids and water (Bernstein et al., 2004). T_E occurs when the central k-space line is acquired, at 40 ms. Spoiler gradients are present at the end of the sequence. A large RF spike is also visible for spoiling near 67 ms. (**B**) Idealized k-space filling scheme for this Cartesian EPI sequence, with data acquisition beginning in the top right corner. One full slice of image data is acquired per T_R, with no under-sampling. Similar plots previously appeared in Davis (2009).

compared to conventional read-outs, such that a series of images may be acquired sequentially with good time resolution. For example, in the studies that follow, three slices of image data were acquired from the leg every 250 ms. However, EPI requires a very homogeneous background field and can introduce artifacts. A pulse sequence diagram and the k-space filling scheme are shown in Figure 1.1.

1.2 Muscle T_2^*-weighted imaging literature review

In the brain, the intervention producing BOLD contrast would typically come in the form of sensory input or a cognitive task. In muscle, several options are available, with the most commonly used being ischemia-reactive hyperemia paradigms, discussed below. Exercise is also frequently employed, most commonly as single contractions, and this literature will be discussed. Finally, a small number of studies have used hyperoxia, hypercapnia, or vasomodulating drugs, sometimes following exercise (Noseworthy et al., 2003; Bulte et al., 2006).

T_2-weighted techniques may also be useful for characterizing muscle oxygenation, and relevant to the discussion here, since T_2^* effects include T_2 intrinsically. T_2-weighted muscle studies are sometimes referred to as mfMRI, with signal changes being regarded as markers of muscle recruitment. T_2 studies do not typically have the high time resolution of BOLD studies, and require a more intense exercise challenge to see effects (Meyer et al., 2001). Muscle activation in plantar flexion (PF) exercise with various knee angles has been examined with this technique (Price et al., 2003). More recently, muscle oxygen saturation (S_{mO_2}) has been measured using T_2-weighted imaging (Decorte et al., 2014).

Ischemia intervention

This technique entails the total occlusion of blood supply to an extremity, usually using an inflated blood pressure cuff for several minutes. GRE EPI images are acquired continuously during occlusion and after the pressure is released, when a hyperemic state of reperfusion is induced. The first studies of muscle BOLD imaging used this intervention in conjunction with myoglobin spectroscopy to reveal the existence of the muscle BOLD effect (Lebon et al., 1998a), and distinguish it from simple perfusion (Lebon et al., 1998b).

Later studies sought to compare the BOLD signal with other modalities such as perfusion measures from arterial spin labelling (Duteil et al., 2006; Englund et al., 2013), laser Doppler flowmetry and transcutaneous oxygen pressure (Ledermann et al., 2006a), as well as venous oxygen saturation (S_{vO_2}) from multiple GRE echoes (Englund et al., 2013), and near-infrared spectroscopy (NIRS) (Sanchez et al., 2010). Though the BOLD signal has been shown to have elements in common with the other techniques, a quantitative model for the BOLD reperfusion peak has not been described. The peak is typically described in terms of timing and magnitude compared to other measures (Englund et al., 2013), and a curve fitting scheme has been proposed for the signal shape (Schewzow et al., 2013). It has been shown that the BOLD effect in skeletal muscle is almost completely determined by intravascular blood (Sanchez et al., 2010), and that calculated short T_E images (i.e. interpolated to 0 ms) have a different time course from long T_E (45 ms) (Nishii et al., 2015b).

Subject populations have also been studied using the technique, including those with peripheral vascular disease (Ledermann et al., 2006b; Englund et al., 2013), smokers (Nishii et al., 2015a), systemic sclerosis (Partovi et al., 2012a), aged subjects compared to younger ones (Schulte et al., 2008), and subjects with differing bone density (Ma et al., 2014). A well designed study also showed that athletes and sedentary controls had significantly different hyperemic responses in the lower leg (Stacy et al., 2016). The muscle BOLD contrast has been shown to be much greater at 3T than 1.5T (Partovi et al., 2012b), and greater still at 7T (Towse et al., 2016a).

Muscle contraction intervention

Studying muscles after contraction is likely to lead to novel information, since exercise generates large, dynamic changes in blood flow and oxygenation in muscle. The exercise changes in muscle compared to rest are discussed in section 1.5. Exercise studies are also likely to be relevant to subject populations, as intermittent claudication during walking is a common complaint in peripheral vascular disease (Labs et al., 1999). Previous studies have used brief single contractions and isometric contractions to modulate muscle physiology for study.

In single contractions, the muscle BOLD signal intensity was found to depend strongly on field strength and contraction force (Meyer et al., 2004). Shorter T_E GRE data was found to have good correlation with perfusion measures (Wigmore et al., 2004). Later, GRE EPI muscle BOLD data was found to have greater contributions from blood volume (BV) at low T_E (6 ms) and blood oxygenation at longer T_E (46 ms) (Damon et al., 2007). A model was further developed that described the relative contributions of BV and oxygenation to the muscle BOLD signal following single dorsiflexion contractions (Towse et al., 2011). The signal was predicted from arterial blood flow and S_{mO_2} measured by Doppler ultrasound and NIRS, respectively, with excellent agreement to measured results. Within the realm of MR, a proof-of-concept paper has been published with data from both muscle BOLD imaging and phosphorous spectroscopic imaging during exercise with a dual-tuned coil (Brown et al., 2016). The signal time courses from the two methods were not directly compared.

Populations of active compared to sedentary individuals have been shown to exhibit differing temporal signal characteristics of muscle BOLD after single contractions (Towse et al., 2005). No group differences in BOLD signal following single contractions were seen in a study of diabetics; however, a significant age effect occurred (Slade et al., 2011). Pilot data of post-exercise muscle BOLD has been acquired at 7T (Towse et al., 2016b).

Aside from single contractions, a novel dynamic PF exercise protocol with interleaved imaging has been developed (Muller et al., 2016), with the BOLD signal showing good stability over 14 min and emphatic differentiation between two mild workloads. Also, the BOLD signal time course in small regions of interest (ROIs) in the quadriceps muscle following repeated contractions has been described, with curve fitting to an empirical function (Caterini et al., 2015).

1.3 Muscle motion and strain

Muscle strain, which can be assessed by mapping muscle displacement, is a key biomechanical measurement for understanding muscle function and plasticity (Monti et al., 1999; Oomens et al., 2009; Trotter, 2002). Although muscle tissue strain can be assessed in vitro, changes in muscle architecture due to voluntary contractions differ significantly from passive motion, necessitating in vivo imaging techniques to truly understand muscle function. Especially in muscles with a pennate structure such as those of the triceps surae, it is difficult to relate joint movement to muscle fibre contraction by external observation or cadaver examination alone (Fukunaga et al., 1997). Furthermore, even relatively simple muscles experience heterogeneous strain throughout a muscle contraction (Pappas et al., 2002), both spatially and temporally (Drost et al., 2003). Complex strain distributions may result from stretching of passive connective tissue associated with the muscle and lateral transmission of force among individual fibres. Non-uniform strains may also be influenced by variation in fascicle length and curvature within a muscle (Blemker et al., 2005).

The research in this thesis involves PF contractions in the lower leg. This exercise is primarily driven by the triceps surae (TS) muscle group, composed of the soleus muscle (SM) and the two heads (lateral and medial) of the gastrocnemius muscle (LGM and MGM, respectively; together GM) (Murray et al., 1976; Fukunaga et al., 1996; Finni et al., 2006). Although the soleus muscle is complex, with three distinct parts (Agur et al., 2003), the muscle fibres of the posterior soleus generally extend proximally from an aponeurosis on the anterior side of the muscle towards insertions which are more distal on the posterior side (see Fig. 3.3 on page 83). The gastrocnemius fibres, on the other hand, extend proximally from a superficial aponeurosis to a distal insertion on the deeper side of the muscle (Hodgson et al., 2006). Both the posterior soleus and the gastrocnemius muscles have a relatively uniform intramuscular structure.

At the distal ends of the gastrocnemius and soleus muscle fibres, attachment occurs at acute angles to sheet-like aponeuroses (Gray, 1918). Though the two aponeuroses are separate and move independently (Bojsen-Møller et al., 2004), they are difficult to distinguish with MRI due to their proximity, thin cross-section, and the general lack of MR signal from connective tissues with short T_2 (Robson and Bydder, 2006). Towards the inferior end of the lower leg, the two aponeuroses join to form the achilles tendon. This is illustrated to some extent in figure 3.3A as the connective tissue labelled *DA* becomes increasingly thick in the distal direction. Significant individual variation exists in the lengths of the gastrocnemius and soleus aponeuroses before the common attachment (Blitz and Eliot, 2008, 2007).

Muscle motion and strain imaging

Given the complexity of the muscle length and angle changes that lead to displacement of the achilles tendon, *in vivo* imaging studies are warranted. The techniques of velocity encoded phase contrast (PC) and spin tagging (ST, sometimes known as SPAtial Modulation of Magnetization, SPAMM) have been developed to study muscle kinematics using MRI (Sinha et al., 2004). Spatial ST is employed in muscle displacement studies as a *ground truth* measure. The technique applies saturation pulses to create a stripe or grid pattern over a region of interest, then acquires a series of images. ST has been used with single-shot imaging to describe the complex heterogeneity of motion in contracting muscle (Englund et al., 2011). The motion of contracting and relaxing muscle is not simple along any axis, such that the muscle is bending, twisting, and contorting itself far more than we may suppose if we visualize a shortening spring along a single fascicle direction.

During PF, the achilles tendon moves superiorly to cause the rotation of the foot about the ankle. The deep aponeuroses of the triceps surae which join to form the tendon must move in the same direction. In relative terms, the motion of the superficial aponeurosis of the gastrocnemius is much less than the deep aponeuroses at the mid-calf level (Kinugasa et al., 2008; Shin et al., 2009). The tendon and aponeuroses undergo both a displacement and a net elongation (Arampatzis et al., 2005), though some aponeurosis sections experience local contraction (Kinugasa et al., 2008). The connective tissue moves because of muscle fibre contractions in the vicinity, which also changes their pennation angle (Kawakami et al., 1998). During PF with 50% effort, the displacement of muscle and connective tissues in the triceps surae at the mid-calf is approximately 1 cm (Muramatsu et al., 2001; Arampatzis et al., 2005). The displacement is almost exclusively in the inferior-superior direction, with very little motion observed in the anterior-posterior direction, and greater displacement for greater exercise intensity (Finni et al., 2003). Furthermore, PC and ST imaging have shown that muscle changes in fascicle length and pennation angle are not consistent along the muscle longitudinally (Kinugasa et al., 2008). The dynamics of fascicle length changes also vary based on the type of contraction (passive, active concentric, active eccentric) (Sinha et al., 2012).

It has also been shown using PC imaging that the cross sectional area (CSA) of muscle fibres changes asymmetrically during eccentric contractions of the gastrocnemius (Kinugasa et al., 2012). As the contraction progresses, the pennation angle of the muscle changes. The CSA also changes to compensate for the changing muscle length in order to maintain constant muscle volume. To add further complexity, these CSA changes are affected by other local muscles pressing on GM.

A final MRI technique that has been applied to skeletal muscle, after being developed to image myocardium, is displacement encoding with stimulated echoes (DENSE) (Zhong et al., 2008). This technique encodes displacement values into phase measures in a similar manner to phase contrast imaging. The study found highly non-uniform strains in biceps muscle under tension.

1.4 Triceps surae muscle comparisons

The muscles of the triceps surae are known to have different characteristics. Perhaps the most familiar difference is fibre type: SM is considered to be a *slow* twitch muscle (69% type I fibres), and GM is considered to be *mixed* (51% type I fibres) (Gregory et al., 2001). However, the same study argues that enzyme activity is a more important marker of muscle function than fibre type. With SM and LGM showing similar enzymatic markers of fatigue resistance, the argument can be made that both muscles are adapted to chronic loading in humans. Along the same lines, the same authors argue that both GM and SM share the peak forces during maximal PF exercise. The fact remains, however, that type I fibres favour aerobic energy supply, which imposes less energy demand and is less prone to fatigue than fast fibres, and that LGM contains about seven times as many type IIx fibres as SM.

A previous study in a small number of subjects had revealed similar differences between SM and GM in terms of relative content of slow twitch vs fast twitch fibres, with SM at 64% compared to 50% in LGM by area (Andersen and Kroese, 1978). The study included only four subjects, and there was large variance in the values (SE 6%), but in all subjects the percentage of slow twitch fibres in SM was at least 10% higher than LGM. The study also examined capillary density, with GM being 27% higher than SM in transverse cross sections. However, the larger fibre diameters reported in SM meant that it had 45% more capillaries per fibre than GM. Differences in capillary network organization were also revealed, with capillaries in SM being more tortuous and frequently branching.

Another study showed a differing fibre type distribution, though following the same trend, reporting 73% type I fibres by area in SM, compared to 59% in LGM (Vandenborne et al., 1995). The study emphasized that the metabolic differences in human muscles between fibre types are much less pronounced than those reported in animal studies.

Other differences in vessel anatomy between the soleus and gastrocnemius include venous sinuses, which are more numerous and more important in the soleus than the gastrocnemius (Meissner, 2005). Significant differences in vascular anatomy also occur between individuals, with that review placing the proportion who have the classic anatomy at about 1 in 6. As an example, the author stated that 25% of people have a duplicated saphenous vein in their calf, and that the presence or absence of venous valves is variable among individuals. Valves and sinuses are vital to operate the calf muscle pump, which is important for venous return of blood, at least while standing and during upright exercise. It has also been stated that the venous structure of GM and SM are very different: veins in GM run in a well ordered fashion along the muscle fibres, while SM veins are more mesh-like and disordered (Hara, 2008). This may lead to stagnation of venous blood flow in SM, especially with increased muscle tone.

Given the impact of BV and oxygenation on the BOLD signal, the differences between muscles are important. Three factors in SM compared to GM have been described above: increased capillarity associated with type I fibres, increased number of venous sinuses, and a more disordered venous network. Together, these factors strongly imply that the BOLD signal from the two muscles could look quite different in recovery after exercise.

1.5 Changes during exercise

This section details the physiological changes that occur in muscle during dynamic exercise. The measures discussed emphasize those that may affect the muscle BOLD signal, and are not an exhaustive list of parameters that vary during exercise and recovery. Blood flow measures discussed below are acquired from either Doppler ultrasound or thermodilution techniques. Oxygen content in arterial and venous blood are measured by direct sample analysis. Plantar flexion exercise challenges were sometimes found in the literature, but much more often the exercise challenges were cycling or knee extension exercise (single or double leg). The findings of this section are summarized in Table 1.1 on page 22, where the interested reader may find the most relevant parameter changes for the purposes of the later research chapters.

Temperature

One of the most obvious changes that occurs in exercising muscle is an increase in temperature. In one study, muscle temperature increased by 6 °C during submaximal exercise (Saltin et al., 1968). This measurement occurred at a superficial site that started at a temperature several degrees cooler than the core. The intramuscular temperature increased rapidly at first, but took 10–20 min to stabilize, and was concurrent with a more moderate increase in core temperature and decrease in local skin temperature. Another study showed that femoral venous blood temperature during maximal cycling exercise matched the core temperature, rising 2–3 °C in subjects who were already warmed up (González-Alonso and Calbet, 2003). In a third study with 15 min of submaximal exercise, temperature increases of 2–3 °C were reported (Kenny et al., 2003). After exercise, muscle temperature cooled rapidly at first (~ 0.75 °C in 10 min) but remained elevated even after 60 min. An interesting feature of the data was that a gradient of 1 °C existed from deep to superficial muscle before exercise, but the gradient disappeared during exercise and was still far reduced 60 min hence.

The MRI signal is known to be sensitive to temperature in many different ways, including changes in T_2 (Rieke and Butts Pauly, 2008). A study of ex-vivo rabbit muscle samples recorded changes in T_2-weighted signal of approximately −1.7 %/°C in the relevant temperature range (Fig. 1.2) (Graham et al., 1998). This is similar to the change in signal intensity recorded in a lower temperature range from ex-vivo heart tissue (Kaye et al., 2010). In that case the slope was approximately −1.8 %/°C, however it was measured using a very short T_E sequence with mixed T_2^* and T_1 weighting in the range 0–20 °C. These results for the signal-temperature relationship may be specific to the particular image contrasts used in the two studies. If generally applicable, they imply that the temperature drop reported above, 0.75 °C in 10 min, would lead to an MRI signal increase of about 1% during exercise recovery.

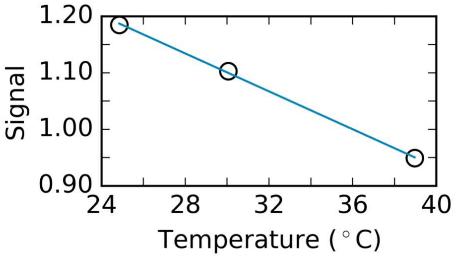

Figure 1.2: Signal change with temperature. The T_2-weighted signal intensity, normalized to the value at 36 °C, is shown with linear fit. The slope of the fit indicated a signal decrease of 1.7% for every 1 °C rise in temperature. Data from Graham et al. (1998), acquired from their plot by manual selection using *xyscan* (`rhig.physics.yale.edu/~ullrich/software/xyscan`).

Blood flow

At the onset of dynamic exercise, heart rate increases rapidly to deliver resources to working muscle. This was shown during a hard dynamic exercise task, when heart rate rapidly increased in the first minute to 80% of the maximal value, with pulmonary oxygen uptake increasing by approximately 500% compared to a rested, warmed-up state (González-Alonso and Calbet, 2003). Cardiac output may have limited the trained subjects' exercise capacity. In sub-maximal exercise with a consistent work rate, heart rate remains stable. This was shown in a mild dynamic task lasting 6 min, when heart rate stabilized within 15 sec at a value 30% above rest (MacDonald et al., 1998). Cardiac muscle perfusion is increased in dynamic exercise tasks, but at high work loads, skeletal muscle perfusion accounts for the vast majority of cardiac output (Laughlin et al., 2010).

Blood flowing from the heart to muscles passes through arteries that branch several times into smaller arterioles, running both across and along muscle fibres. Some arterioles are paired with venules, though a venule does not typically drain its paired arteriole (Segal, 2005). The group of capillaries fed by a terminal arteriole is termed a miscrovascular unit (MVU), representing about 0.1 mm^3 of muscle tissue. MVUs represent the smallest functional unit for the expression of blood flow control (Korthuis, 2011). Capillaries are only about 4 μm in diameter, though this increases at branch points and venule junctions (Korthuis, 2011). This necessitates that red blood cellss (RBCs), which are about 25% larger, deform into cigar-like shapes to pass through (Snyder and Sheafor, 1999). Transit times of red blood cells through capillaries are correlated with body mass across species, and can be expected to be approximately 0.7 s in a 70 Kg human (Kayar et al., 1994). The modern view of capillaries is of extensively branching structures, with massive heterogeneity in flow rates among individual vessels, though none are normally occluded, even at rest. The hematocrit, RBC flux, and RBC velocity all vary widely among capillaries, with some capillaries carrying only plasma (Poole et al., 2013).

At rest, only 5–10 mL of blood per minute is distributed to 100 g of muscle (Laughlin et al., 2010; Korthuis, 2011). Muscle perfusion is highly variable, not only during exercise but also in anticipation of it. When exercise trained rats were placed on a stationary treadmill, muscle perfusion increased by as much as double the untrained rest value (Delp, 1998). Upon initiation of exercise, glycolysis begins within seconds, thus greatly increasing the demand for oxygen (Greenhaff, 2003). Changes in muscle perfusion occur due to the interplay between centrally controlled vasoconstriction (vasomotor tone), locally stimulated vasodilation, and the mechanical effects of muscle contraction (muscle pump) (Segal, 2005; Laughlin et al., 2010).

Vascular dilation due to exercise happens first and to the greatest extent in the arterioles feeding the contracting muscle (Laughlin and Roseguini, 2008). The vasomotion of smaller arterioles is terminated so that the flow rates of red blood cells through individual capillaries are determined by the physical characteristics of the flow path in the MVU, rather than by any active mechanism (Segal, 2005). Nevertheless, large heterogeneity in RBC flow among capillaries remains. Larger arterioles dilate to increase flow to muscle regions (Murrant and Sarelius, 2000). Upon initiation of contractions, RBC velocities and flux are increased within capillaries. Hematocrit also increases, with RBCs packing more tightly together within the vessels (Kindig et al., 2002). Hematocrit in capillaries is still reduced compared to systemic circulation, necessitating that RBCs travel much faster than plasma in those vessels (Poole et al., 2013).

Exercising muscle experiences perfusion increases of 10 to 20 times the resting value (Korthuis, 2011). By comparison, the increase in blood volume with exercise is modest. It occurs as a result of increased flow and hematocrit rather than activation of new capillaries (Poole et al., 2013). Within muscle, perfusion increases more near oxidative fibres than fast-twitch glycolitic ones (Laughlin and Armstrong, 1984). This can be attributed to the greater density and increased number of interconnections in oxidative muscle capillaries (Korthuis, 2011).

During dynamic exercise, both blood flow to working muscle and muscle $\dot{V}O_2$ increase linearly with power output. $\dot{V}O_2$ refers to the rate of oxygen consumption, measured in l/min. This has been shown with knee extension exercise (Andersen and Saltin, 1985). The reported perfusion changes represented increases of 1000–2000% at maximal exercise compared to rest. It is also noteworthy that flow increases were accomplished by vasodilation at lower work rates and increased arterial pressure at higher work rates, with the transition occurring at about 60% of $\dot{V}O_2$-max.

Even higher increases in muscle perfusion of 3000% have been reported in near-maximal human knee extension exercise in *trained* subjects, with blood flow increasing from rest levels in about 10–30 s (Saltin et al., 1998). Blood flow and oxygen uptake were also shown to be stable with dynamic exercise of up to one hour duration at constant workload. The paper aggregated data from several studies to show linear increase in blood flow and perfusion with power output.

In mild knee extension exercise, mean blood velocity was observed to stabilize at 500% above the resting value in 1 min (MacDonald et al., 1998). The same study showed that changes in arterial diameter and pressure as well as blood velocity depended on body position (supine or upright), while leg blood flow did not. It also reinforced the concept that blood flow and oxygenation change in lock step with one another.

In a maximal cycling experiment that examined whole-leg blood flow, increases of 1000% were observed within 1 min (González-Alonso and Calbet, 2003). Blood flow continued to increase slightly, peaking at 3 min and falling slightly with fatigue. Vascular conductance (VC) in exercising muscle rapidly increased by about 950% at the onset of maximal exercise and remained constant throughout.

Following exhaustive cycling exercise, mean arterial pressure, heart rate, and leg $\dot{V}O_2$ stabilized to values slightly above resting within a few minutes (Rådegran and Saltin, 1999). On the other hand, VC and femoral artery blood flow decreased more slowly after exercise, and remained elevated with a strong decreasing trend after 10 min of recovery. VC in this study showed different values than the study of González-Alonso and Calbet (2003), but still showed approximately 1000% change with exercise. VC showed a 20% increase in the first minute after cessation of exhaustive exercise, even as arterial pressure dropped rapidly, which would tend to maintain blood flow to the muscle.

Blood flow has also been shown to increase proportionately to exercise intensity measured as a percentage of maximum voluntary contraction (MVC). This was observed in sub-maximal dynamic knee extension exercise with blood flow measured in the femoral artery by Doppler ultrasound (Walløe and Wesche, 1988). Following such exercise, blood flow started at a value equal to the maximal flow during exercise and decreased rapidly; it returned to baseline after approximately 1 min in mild exercise, but remained elevated 2 min after intense exercise. A study of forearm blood flow also observed no delay between the end of exercise

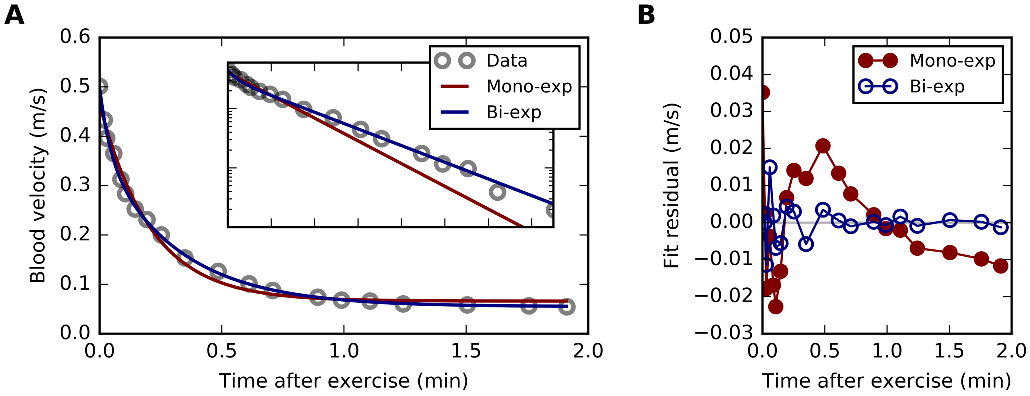

Figure 1.3: Post-exercise blood flow. Femoral artery blood flow data was obtained from the post-exercise portion of the plot in Figure 5 of Walløe and Wesche (1988). **(A)** Mono-exponential and bi-exponential curve fits to the data are shown. The inset shows the same data on a logarithmic y-axis, with the resting blood flow assigned a value of 0. Visually, the bi-exponential curve provides a better fit to the data. **(B)** Residuals from the model fits. The residuals from the bi-exponential fit are smaller, and do not show the structure of the mono-exponential residuals. The BIC was also dramatically lower for the bi-exponential fit (−139, versus −105 for mono-exponential).

and rapid decrease of blood flow, with a steady-state reached after approximately 2 min (Shoemaker et al., 1997). Another study observed that blood flow to the calf dropped immediately after the end of two minutes of dynamic PF exercise, though a slight undulation was observed after the initial rapid drop in half the subjects (Van Leeuwen et al., 1992). The rapid blood flow decreases observed in these studies were suggestive of an exponential trend.

A small study was undertaken to determine whether the rapid blood flow decrease observed after exercise was actually exponential. Data was extracted from the post-exercise portion of the plot in Figure 5 of Walløe and Wesche (1988), by manual selection of points from the curve using *xyscan* (`rhig.physics.yale.edu/~ullrich/software/xyscan`). Figure 1.3 shows the data and fits of mono- and bi-exponential curves. The time constant of the mono-exponential fit was 14 s. The time-constants of the bi-exponential decays were 2.5 s and 19 s, with the longer component being about three times greater in magnitude. The bi-exponential model provided a much better fit, as seen in the plot, and removed the undesirable structure that was present in the residuals of the mono-exponential fit. The Bayesian information criterion (BIC) also provided a rationale for choosing the more complex bi-exponential model. The BIC values were -105 and -139 for mono- and bi-exponential models, respectively. Lower values of BIC are preferred (Spiess and Neumeyer, 2010).

The observed bi-exponential decrease in muscle perfusion following exercise is relatively tranquil and well-ordered compared to perfusion during exercise. While a muscle is contracting, pressure in intramuscular veins and draining veins is much higher than at rest or during relaxation (Laughlin, 1987). Muscle perfusion is significantly if not completely impeded during contractions (Van Leeuwen et al., 1992). Venous blood is expelled toward the heart, in an action known as the *muscle pump* effect. As the muscle tension eases, a hyperemic state is induced, so that intramuscular blood flow is highly variable with the rhythm of contractions.

Blood oxygen saturation

The Andersen and Saltin (1985) knee extension study showed that arterial oxygen saturation (S_{aO_2}) remained very high at around 98%, while venous oxygen saturation (S_{vO_2}) decreased from about 70% at rest to below 30% during near-maximal efforts. Systemic hemoglobin concentration ([Hb]) remained stable during exercise. Mean arterial blood pressure was stable initially, but rose by 30% at higher work rates. In the González-Alonso and Calbet (2003) study, [Hb] rose about 5% during the first 3 min of exercise to exhaustion. During exercise, S_{aO_2} fell about 3%, so that overall oxygen content of arterial blood remained stable. S_{vO_2}, meanwhile, fell rapidly from 61% at rest to 20% after 30 sec and below 15% thereafter.

Following sub-maximal dynamic exercise in trained subjects, phosphocreatine (PCr) recovery within the muscle was shown to take several minutes, and was somewhat limited by local oxygen availability (Haseler et al., 1999). S_{vO_2} values after exercise were found to recover to values above rest within 10 min, even after prolonged (3 h) cycling exercise (Ahlborg and Felig, 1982). Following intense knee extension exercise of 3 min duration, S_{vO_2} recovered to values above rest after approximately 1 min (Bangsbo et al., 1990). S_{vO_2} remained elevated for about 10 min, then fell back to resting values at about 30 min post-exercise.

After a moderate cycling exercise challenge, S_{mO_2} as measured by NIRS took less than one minute to peak above steady state levels in untrained subjects, and appeared to occur more quickly than return of pulmonary $\dot{V}O_2$ to baseline levels

(Belardinelli et al., 1997). In the same study, a delay was observed between the end of exercise and the start of recovery of both S_{mO_2} and central $\dot{V}O_2$. The delay was often several seconds, ranging up to 30 sec. Muscle BV and oxygenation changes were observed to be tightly coupled after exercise, with non-significant differences in timing.

In a separate study of exercise to failure, muscle NIRS data showed a similar delay in temporal changes (10–20 sec on average in normal subjects) in S_{mO_2} and BV during recovery after exercise (Matsui et al., 1995). BV stabilized near baseline levels in about 2 minutes, but values of O_2Hb/O_2Mb stabilized above resting levels while HHb/HMb stabilized below resting levels, causing an increase in blood oxygen saturation to persist after that period.

In a NIRS study with dynamic PF exercise at 50% MVC, BV and oxygenation displayed a similar temporal pattern: after exercise, HHb decayed back to resting levels in 1-3 min, while O_2Hb increased and remained elevated at the end of measurements (3 min) (Torricelli et al., 2004). A flat delay in the temporal signal was also observed in this data (HHb, O_2Hb, ΔS_{mO_2}, ΔtHb) for up to 1 min before the signal started to change at some measurement sites. The delay was most reliably observed in relative total hemoglobin (ΔtHb) values. Absolute values of total hemoglobin (tHb) were elevated during exercise by 5%, and remained elevated compared to rest values after 3 min of recovery. Absolute S_{mO_2} values were decreased during exercise by 8%, but increased above resting levels and remained elevated after 3 min recovery by 3%. Similar trends were reported in NIRS data for 1 min following maximal isometric contractions, with the relative muscle oxygen saturation (ΔS_{mO_2}) values recovering above rest in about 45 sec, though only relative values were available in that study (Ferrari et al., 2011).

The NIRS signal is hard to interpret physiologically. Absolute quantitative values are not typically available, since the light path length is not usually known (McCully and Hamaoka, 2000). The source of the signal is further uncertain as it is a weighted average of the blood signals from the veins and capillaries. If the relative BV changes among these two pools, the NIRS signal changes as well. The thickness of subcutaneous fat adds further uncertainty to signal changes (Miura et al., 2001). The oxygenation of myoglobin contributes to the signal as well, by approximately 20% (Torricelli et al., 2004). As a result of these confounds, the NIRS signal sometimes shows divergent characteristics compared to S_{vO_2} during exercise (MacDonald et al., 1999).

Myoglobin

Myoglobin (Mb) is a protein found in the muscle fibre cytoplasm that reversibly binds oxygen. It contains only one iron atom per molecule, unlike the four per molecule of hemoglobin (Hb). Like Hb, Mb is known to be paramagnetic in the deoxygenated state (HMb), but not as oxy-myoglobin (O_2Mb) (Taylor, 1939). Its role is to store oxygen for later use when the muscle is working, and to facilitate the diffusion of oxygen from capillaries into the cell (Ordway and Garry, 2004). This function results from the fact that Mb binds oxygen much more readily than Hb, meaning that very low PO_2 values are required to saturate Mb compared to Hb. For example, 50% saturation of Mb occurs at approximately 4 Torr (500 Pa), while 50% Hb saturation occurs at 25 Torr (3300 Pa). Myoglobin desaturation can be readily measured using in vivo magnetic resonance spectroscopy (MRS) during ischemia and exercise. In one exercise study, myoglobin saturation has been shown to remain at about 50%, regardless of exercise intensity (Richardson et al., 1995). A later study refuted this, showing a linear relationship between power and HMb that *culminated* in 50% myoglobin saturation at peak power output (Molé et al., 1999).

Myoglobin concentration ([Mb]) has been measured as 4.7 g/kg wet mass of muscle (range 3–5 mg/g), measured by biopsy from the quadriceps muscle (Möller and Sylven, 1981). In resting gastrocnemius muscle in a supine position, [Hb] was measured as 140 µM using NIRS (Torricelli et al., 2004). Using a molecular weight of 65 000 g/mol for Hb and muscle density of 1.1 g/cm^3, this leads to [Hb] of 8 g/kg muscle. Similarly, BV in resting supine human thigh muscle has been measured at 3.3 ml/0.1 kg muscle using positron emission tomography (PET) imaging (Raitakari et al., 1995). Taking a value of 145 g/l Hb in blood as typical (Otto et al., 2013), this leads to a [Hb] value of 4.8 g/kg muscle. The difference in values may be due to the difference in muscles examined, or the superficial nature of the NIRS measurement.

It is established that Mb occurs in comparable concentrations to Hb at rest, desaturates with intense exercise, and that HMb is paramagnetic. Given these properties, Mb may be expected to significantly contribute to the muscle BOLD signal. However, an ischemia study showed that Mb desaturation played little if any role in T_2^*-weighted muscle signal change, though that study used $T_E = 15$ ms (Lebon et al., 1998a).

Posture

Postural changes are known to cause large changes in leg BV. This occurs because of the increased blood pressure in the legs compared to the heart while standing, and the compliance of the vasculature, especially the veins. BV, as measured by NIRS in the calf, increased by 25 μM in 10 min of head-up tilt compared to supine posture (Truijen et al., 2012). Posture must also be considered when discussing leg BV following exercise. In cycling exercise with an upright posture, BV in the leg was reduced by 20–30% depending on work rate, having been redistributed to the thorax (Flamm et al., 1990). The study used radionuclide techniques, and also revealed that the source of increased blood [Hb] during intense exercise was primarily the spleen; the organ had highly reduced BV during maximal cycling, and BV recovered by about 50% at 10 min post-exercise.

Exercise BV, as measured by NIRS, was also shown to decrease during upright PF (Miura et al., 2001). The decrease is thought to be due to the action of the muscle pump, and BV increased above the resting value in recovery. A more nuanced effect has been presented in upright cycling as well, with a NIRS-measured BV decrease during no-load warm-up due to ejection of HHb, followed by a BV increase compared to rest in high-load exercise (Matsui et al., 1995). In contrast to the upright results, supine PF brought about a NIRS-measured BV increase in the legs during exercise (Torricelli et al., 2004) and BV remained elevated in recovery. The maximal BV changes in that study, +15–20 μM compared to rest, were slightly lower than the changes from head-up tilt reported earlier. This likely explains a large proportion of the differing trends due to upright or supine posture.

Other Effects

Some effects of exercise do not dissipate quickly. Following muscle damaging exercise, such as intense eccentric exercise, markers of oxidative stress and muscle damage (such as plasma presence of creatine kinase) are elevated for several days, while force production is reduced (Nikolaidis et al., 2008; Edwards et al., 1977). In long term training studies, muscle blood flow capacity as measured by the hyperemic response is increased, especially as a result of endurance training. Muscle oxidative capacity is also increased, as measured by cytochrome c concentration (Laughlin and Roseguini, 2008). This capacity is associated with region specific angiogenesis of capillaries. Broadly speaking, muscle oxidative capacity is highly correlated with peak blood flow values, reinforcing the nature of the coupling of these two factors (Laughlin and Armstrong, 1984).

Muscle water content (intra and extra-cellular) can vary by as much as 25% during exercise (Sjogaard et al., 1985). The same study showed that concentrations of K+ and lactate, which increase in plasma during exercise, return to baseline levels in about 30 min after maximal dynamic exercise.

Measure	Rest → Ex. Values	Rel. change	Delay	SS Time
Muscle perfusion, f_m (L/kg/min)	0.13 → 2.4	+2000 %	0	1–3 min
Vascular conductance, C_v (mL/min/mmHg)	2 → 19	+950 %	~60 s	> 10 min
Arterial S_{aO_2} (%)	98 → 98 ± 2	0 %	–	–
Venous S_{vO_2} (%)	61 → 13	-80 %	0	1 min
Myoglobin S_{O_2} (%)	100 → 50	-50 %	?	?
[Hb] (g/dL)	14.2 → 15.0	+5 %	?	?
Temperature (°C)	35.5 → 37.5	+6 %	0	> 60 min
NIRS BV (μM)	139 → 145	+5 %	30–60 s	1–3 min
NIRS S_{mO_2} (%)	72 → 66	-8 %	0–60 s	1–3 min

Table 1.1: Physiological changes during exercise and recovery. Values indicated are expected change during intense, near-maximal dynamic exercise of 2.5 min duration in untrained subjects. Delay indicates whether a flat period of little or no change has been observed following exercise for that parameter. Recovery time indicates an approximate duration for the parameter to reach a steady state value, even if that value is different from rest. Fields marked with ? indicate that no literature source for the post-exercise timing was found. For further explanation see the preceding section.

1.6 Multivariate analysis and its application to fMRI data

The typical approach to analysis of fMRI data in the brain consists of creating a mathematical model for the expected BOLD response based on the intervention used during the experiment and a hemodynamic response function (HRF). This is described as a *mass univariate* approach, since the time series of each voxel is modelled separately from its neighbours. In the simplest kinds of these experiments, an active phase is repeatedly compared to control (inactive) conditions. More complicated functional studies use event-related designs in which numerous elements are compared against a resultant BOLD signal. These are often modelled using a general linear model (GLM) multiple regression approach (i.e. one dependent variable, the BOLD signal, and multiple independent variables). These models assume a particular form of model which may or may not be precisely known. In cases where the model is not known, or is overly complex with little physiological understanding, other data-driven *multivariate* approaches may be more useful.

PCA, SVD, and FA

Early approaches to multivariate analysis of fMRI data were dominated by principal component analysis (PCA). PCA is probably the oldest and most often used multivariate analysis technique (Abdi and Williams, 2010), dating to Hotelling (1933). This approach expresses the data from all voxels using new variables (components) derived most frequently from individual time series. The primary component has greater mean squared correlation with the data set than any other possible component. Further components are chosen in turn to have the next greatest mean squared correlation with the data, from the family of components that are mutually uncorrelated with the earlier ones. Typically fewer components are retained to describe the variance of the data than the number of original variables, and in this way PCA may be regarded as a *data compression* or *dimension reduction* technique; this may lead to interpretation of the components for clustering or outlier detection, for example (Jolliffe, 2002).

To put this in more concrete terms, we may express the BOLD signal time course of a single voxel as the vector $\boldsymbol{x}_1$, and the time courses of the other $p - 1$

voxels in a data set as $\boldsymbol{x_2} \dots \boldsymbol{x_p}$. If n time points were collected, the data may be organized as a matrix, $\boldsymbol{X}$, with n rows and p columns. The covariance of the first two vectors is

$$\mathrm{cov}(\boldsymbol{x}_1, \boldsymbol{x}_2) = \frac{1}{n-1} \sum_{i=1}^{n} (\boldsymbol{x_1} - \overline{\boldsymbol{x_1}})(\boldsymbol{x_2} - \overline{\boldsymbol{x_2}}) \tag{1.5}$$

Then the variance-covariance matrix, C, may be defined as a square symmetric $p \times p$ matrix in which the elements $C_{ij} = C_{ji} = \mathrm{cov}(\boldsymbol{x}_i, \mathrm{x}_j)$, and the diagonal elements C_{ii} are the variances of the respective vectors. The column-centred variables may be labelled $\boldsymbol{z}_i = \boldsymbol{x_i} - \overline{\boldsymbol{x_i}}$, and organized into a matrix $\boldsymbol{Z}$ with the same dimensions as $\boldsymbol{X}$. Then C may be computed as $1/(n-1)\boldsymbol{Z}^T\boldsymbol{Z}$. This matrix is sometimes defined without reference to $1/(n-1)$ for convenience, since the eigenvectors are unchanged. Correlation may in turn be defined as covariance normalized by the standard deviations, $\rho = \mathrm{cov}(\boldsymbol{x}_1, \boldsymbol{x}_2)/(\sigma_{x_1}\sigma_{x_2})$.

The covariance matrix has important properties for the purposes of multivariate analysis, chiefly that its eigenvalues are always real and nonnegative, and its eigenvectors are real and mutually orthogonal (Abdi and Williams, 2010). Therefore, the eigenvectors can be chosen to be orthonormal (orthogonal unit vectors). Note that the concept of orthogonality, a geometrical concept, has been extended to this discussion of high dimensional data through the use of the inner product. Due to the favourable properties of the covariance matrix, it can be decomposed as follows:

$$C = \boldsymbol{V}D\boldsymbol{V}^T \tag{1.6}$$

where D is a diagonal matrix of eigenvalues ordered by decreasing magnitude, and each column of $\boldsymbol{V}$ is an orthonormal eigenvector (Fig. 1.4). The eigenvectors are called *principal directions* or *coefficients*. The projection of the centred data onto them, $\boldsymbol{ZV}$, are called the *principal components* or *principal component scores*. The term *loadings* may be defined in various ways depending on the author, but a useful definition to relate the components and the data involves scaling the eigenvectors by the square root of the eigenvalues, as in $\boldsymbol{V}D^{1/2}$.

The correlation matrix may also be used for PCA. In general, using the correlation matrix tends to treat all variables on equal footing, while PCA of the covariance matrix lends more weight to larger variables with greater variance. Note that the reliance of PCA on the covariance matrix means that only *column centred* data is considered. In other words, the orthogonality of raw variables is not of interest,

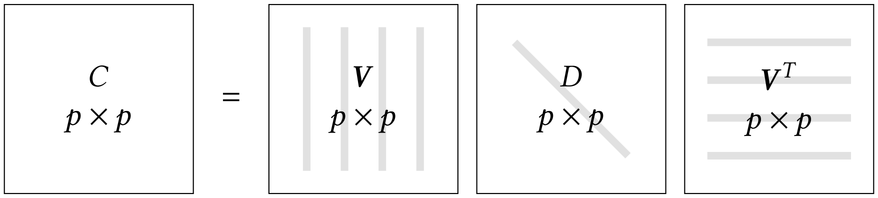

Figure 1.4: PCA of multivariate data. PCA of the covariance matrix C is illustrated. C is $p \times p$ since it is computed from the column-centred data matrix $\boldsymbol{Z}$, which has p variables.

but only the uncorrelated nature (Rodgers et al., 1984). The PCA equivalent on non-centred data has been investigated for certain applications, especially where the geometric origin is of interest in the components (Jolliffe, 2002). In fMRI, the value of zero signal is typically not of interest, but only the fluctuation of the signal about its mean.

Singular value decomposition (SVD) is a closely related technique that operates directly on the data matrix. This is computationally beneficial, since calculating C may be very time-consuming. SVD is often expressed as:

$$\boldsymbol{X} = \boldsymbol{U}\Sigma\boldsymbol{V}^T \tag{1.7}$$

Here, the diagonal elements of Σ are the square roots of the diagonals from D above, and the $\boldsymbol{V}$ matrices are identical. The columns of $\boldsymbol{U}$ are orthogonal along with $\boldsymbol{V}$. $\boldsymbol{X}$ may be used directly in SVD, or the centred version $\boldsymbol{Z}$ may be substituted. From an imaging perspective, the columns of V represent spatial modes that may be called eigenimages, while the columns of U represent temporal modes (Friston and Büchel, 2007). The principal components in this scheme can also be expressed by the relation $\boldsymbol{U}\Sigma$. The diagonal matrix of singular values, Σ, is conventionally organized in decreasing order. Thus a lower dimensional approximation of $\boldsymbol{X}$ amounts to simply reducing the number of columns of $\boldsymbol{U}$ to q, and reducing the size of Σ and $\boldsymbol{V}$ appropriately. This is illustrated in Figure 1.5.

Choosing q, the number of components to keep during dimensional reduction with PCA or SVD, is an open research question (Abdi and Williams, 2010). Classically, one common scheme is the scree plot. In this method, the eigenvalues are plotted on a linear scale, and a transition point in the slope is identified. The location of the transition is somewhat subjective. Another common scheme is to keep

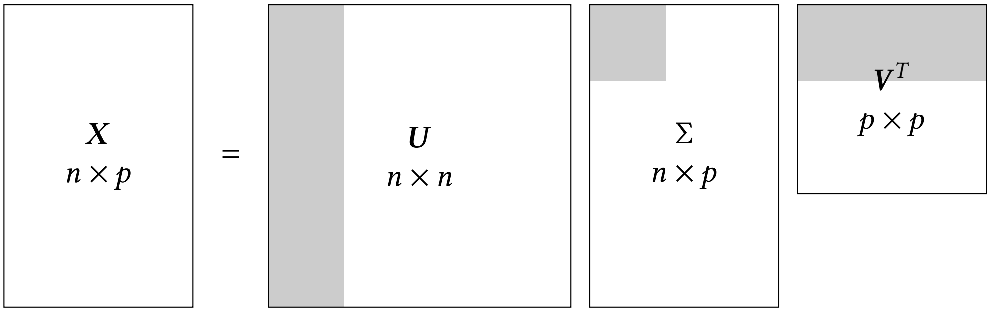

Figure 1.5: SVD of multivariate data. The SVD of the data matrix X is illustrated, where X is composed of p variables organized in columns (e.g. each column could be a voxel time series from an imaging experiment). The shading indicates data that would be used to approximate X with the q largest singular values ($q < p$).

values larger than the average eigenvalue. The method used in later research chapters attempts to penalize the addition of new components that don't offer useful information, and is described in more detail below.

Another related technique is factor analysis (FA), which is commonly expressed as a model:

$$Z^T = \Lambda F + \varepsilon \tag{1.8}$$

FA uses language similar to PCA, with Λ being a matrix of scalar factor loadings, F being the common factors, and ε being the specific factors (i.e. error terms or residuals). In this notation, variables are expressed as rows within the matrices (Fig. 1.6).

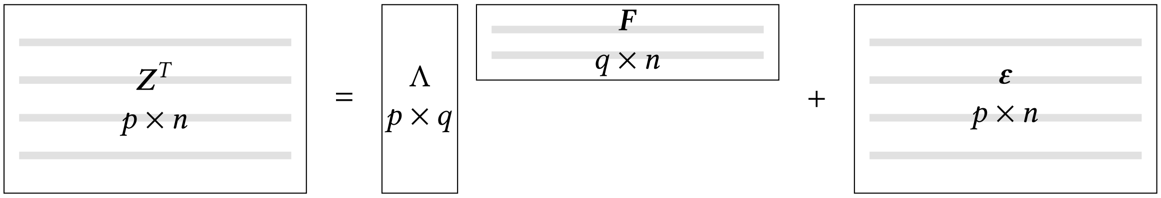

Figure 1.6: FA of multivariate data. The FA model is illustrated. The centred data matrix, Z, is composed of p variables, and q factors are being estimated. The common practice of organizing the variables as rows in FA has been followed.

FA and PCA both attempt to represent aspects of the covariance (or correlation) matrix. FA differs from PCA in that there is no explicit solution to the problem, and the model must be satisfied by an iterative scheme using constraints on the factors and loadings (Jolliffe, 2002). FA always attempts to represent X with fewer factors than its full dimensionality, and it is necessary to recompute the FA model solution with different numbers of factors, unlike using PCA for reduction. Another difference is that a unique, nearly independent variable $\boldsymbol{x_i}$ leads to a unique component in PCA, but would not affect the factors in FA at all; only the error term associated with $\boldsymbol{x_i}$ would be affected. In this way, FA is said to be concerned about the off-diagonal elements of the covariance matrix, while PCA is concerned with the diagonals.

Although FA often requires orthogonal factors, so that SVD may be used to initialize a solution, further constraints are placed on the FA model that require additional processing steps. Arbitrary requirements may be placed on the factors and loadings, depending on the analysis requirements. Two common constraint choices are referred to as *varimax* and *promax* (Martinez and Martinez, 2005). In *varimax*, the factors are rotated while maintaining orthogonality in an attempt to maximize and minimize the loadings on each factor, thus aiding interpretation. In *promax*, the orthogonality requirement is relaxed, allowing correlation between factors.

Whitening is a related technique that is commonly employed to preprocess data before multivariate analysis. The whitening transform produces uncorrelated variables with unit variances. That is, the covariance matrix of the variables is made to be the diagonal identity matrix. Though whitening can be accomplished with infinitely many transforms (Hyvärinen et al., 2001), a commonly used whitening transform can be expressed in terms of PCA variables:

$$T = D^{-1/2}\boldsymbol{V}^T \tag{1.9}$$

Thus, once the PCA model for $\boldsymbol{X}$ is estimated, whitening only requires applying the transform to produced whitened mixtures: $\tilde{\boldsymbol{X}} = T\boldsymbol{X}$.

Plotting of multivariate data may be accomplished in a number of ways. For time series data, the simplest method may be to plot each variable against time, allowing signals to overlay one another. For many variables, it may be beneficial to represent the time series as an image (e.g. Friston and Büchel, 2007). Alternatively, when the data set is made up of p variables, the data may be plotted with each observation being a point in p-dimensional space (e.g. Jutten and Herault, 1991). This may be referred to as the joint mixture. Visualizing the fMRI time series data from two voxels may be useful; then each time point measurement is plotted with respect to two axes. The information on the order of the acquired data in time is lost. Similarly, a q-dimensional subspace ($q < p$) may be defined by PCA, and new data points plotted against the principal components as axes.

BSS and ICA

A common rationale for performing multivariate analysis is blind source separation (BSS). The goal of BSS is to extract features, or components, from the data that describe the underlying generative processes. Independent component analysis (ICA) has been identified as an effective technique for extracting meaningful underlying signals from mixtures (Jutten and Herault, 1991). In PCA, the primary components contain a large proportion of the energy of the signal mixture, but the components themselves remain mixtures. ICA is better able to isolate the sources into separate components and fulfill the goals of BSS. In brain fMRI studies, these components may represent groups of neurons that work in concert during a mental task, and therefore share a common temporal signal.

Much like FA, ICA is defined using a generative model. The simplest expression of the ICA model is usually written as $\boldsymbol{X} = A\boldsymbol{S}$. Here, the rows of $\boldsymbol{S}$ represent estimated components that are statistically independent, and A is referred to as the mixing matrix. Both A and $\boldsymbol{S}$ are unknown, hence the variances of $\boldsymbol{S}$ cannot be determined. The elements of $\boldsymbol{S}$ are usually assigned unit variance to account for this, and are ambiguous in sign. Another way to express the ICA model is through the unmixing matrix, W, which is the inverse of A. Then $\boldsymbol{S} = W\boldsymbol{X}$. Then the goal of BSS is revealed to be the estimation of $\boldsymbol{S}$ such that it represents a good approximation of the real sources.

The FA and ICA models are similar, since both treat multivariate data as a linear mixture of underlying factors. A key difference is that FA assumes the components (factors) are uncorrelated and Gaussian, while ICA requires that the sources are not Gaussian. This is an important distinction for real data sets, which often do not follow a normal distribution (Hyvärinen et al., 2001). In fact, the guiding principle of ICA is that the sources are non-Gaussian; it relies on the central limit theorem to postulate that the mixture of signals will be more Gaussian than the sources themselves. Therefore, making the estimated sources as far from Gaussian as possible should correspond to unmixing them. Another key difference between this ICA model and that of FA is the lack of a noise term; it is assumed that the product $\boldsymbol{AS}$ completely characterizes the input data.

Data is always centred before estimating the ICA model (Hyvärinen and Oja, 2000). This generates $\boldsymbol{Z}$, as in the earlier notations. Algorithms estimating the ICA model also typically employ whitening, to generate $\tilde{\boldsymbol{Z}}$. This reduces the degrees of freedom of the mixing matrix (now called $\tilde{A}$), thus decreasing computation time. The new model is $\tilde{\boldsymbol{Z}} = \tilde{A}\boldsymbol{S}$, with the estimated sources unchanged. Dimensionality reduction with PCA is also often performed at the time of whitening (Beckmann and Smith, 2004). The later research in this thesis uses FSL's *Melodic* software to perform ICA (`fsl.fmrib.ox.ac.uk/fsl/fslwiki/MELODIC`). *Melodic*'s probabilistic independent component analysis (PICA) model includes an additive Gaussian noise term, $\boldsymbol{\eta}$:

$$\boldsymbol{Z} = A\boldsymbol{S} + \boldsymbol{\eta} \tag{1.10}$$

$\boldsymbol{\eta}$ is assumed to be isotropic, and the mixing matrix, A, is rectangular (Beckmann and Smith, 2004). The data is preprocessed to have zero mean and unit variance to account for the isotropic noise assumption. The theoretical framework backing PICA includes the argument that the subspace of the correctly chosen q eigenvectors of $\boldsymbol{Z}$ corresponds to the subspace of the mixing matrix A. Thus dimension reduction using PCA or SVD is an ideal preprocessing step for ICA. *Melodic* estimates the mixing matrix, A in the reduced q-dimensional data space (A is $n \times q$, while S is $q \times q$ at this stage). Then the sources are generated with full spatial fidelity by projecting the unmixing matrix ($W = (A^T A)^{-1} A^T$) onto the data: $S = WZ$ (Fig. 1.7).

The orientation of the data and $\boldsymbol{S}$ matrices in Figure 1.7 imply a spatial independent component analysis (SICA) scheme. This means that the rows of $\boldsymbol{S}$ represent spatial maps, and this is the quantity over which independence is sought, rather than time courses. The PICA algorithm employs an iterative scheme, maximizing the non-Gaussianity of the sources in $\boldsymbol{S}$, while enforcing that the rows are orthogonal and of unit length (Beckmann and Smith, 2004). Z-score maps may then be generated from the ICA sources by dividing by the standard deviation of $\boldsymbol{\eta}$. These maps are then characterized as random values with histograms following a combined Gaussian and Gamma distribution. The Gaussian represents background noise, while activation reveals itself through deviations from the distribution. The

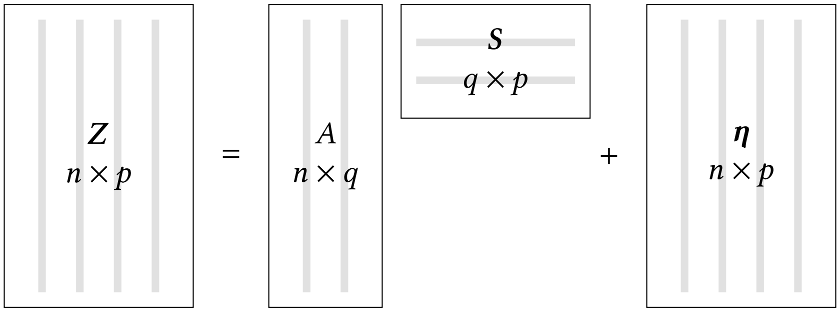

Figure 1.7: ICA of multivariate data. The ICA model is illustrated. This includes an isotropic Gaussian noise term, $\boldsymbol{\eta}$, as implemented in *Melodic*. Within the program, the original p-dimensional data matrix, $\boldsymbol{X}$, is centred and standardized to produce $\boldsymbol{Z}$. Further, PPCA is applied to $\boldsymbol{Z}$ to whiten the data and reduce it to q-dimensions. The mixing matrix, A, is calculated in the q-dimensional space, and contains time courses in its columns. Then A used to produce the $\boldsymbol{S}$ with full spatial resolution. Note that the rows of $\boldsymbol{S}$ contain spatial maps, and these are the quantities over which independence is sought. It is assumed that there are fewer sources than temporal observations ($q < n$).

deviant tails are modelled by Gamma functions, and the resultant maps are thresholded based on the penalization of false positives and false negatives.

There are several ways of measuring the Gaussianity of a signal, with kurtosis being a straightforward choice (Hyvärinen and Oja, 2000). *Melodic*, like the *FastICA* package that underlies it, uses entropy (actually negentropy) by default to measure Gaussianity. This works because Gaussian variables are known to have maximal entropy. In general, the rectangular mixing matrix in the ICA model allows a kind of dimension reduction at the ICA component definition stage, as well as in preprocessing. This is implemented in the *Conn* toolbox (`conn-toolbox.org`). In the *Melodic* implementation, however, dimension reduction is done using PCA preprocessing only.

For selection of the optimal q-dimensional subspace of the data, the PICA method leverages probabilistic principal component analysis (PPCA) (Tipping and Bishop, 1999). PPCA begins with a factor analysis model, deriving a probability distribution, $p(t|x)$, associated with the observed variables, t, and the latent variables, x. It then specifies a Gaussian prior for $p(x)$ and derives a marginal distribution for $p(t)$. By defining the log-likelihood of $p(t)$, the optimal reconstruction can be defined. Once the eigenvectors are defined by PPCA, ICA is used to define the optimal components within this subspace.

The explicit emphasis on non-Gaussianity is not the only strategy for performing ICA. Before *FastICA*, an earlier algorithm called *InfoMax* was described, which emphasizes minimization of mutual information between signals by maximizing entropy (Bell and Sejnowski, 1995). More recently, some authors argue that independence is not the optimal metric for finding components in fMRI data at all, and rather sparsity should be used instead (Daubechies et al., 2009).

Besides *Melodic* and *Conn*, the Matlab *GIFT* toolbox is also commonly used to apply ICA to fMRI data (`mialab.mrn.org/software/gift`). It provides a suite of tools for fMRI analysis using ICA and is in constant development. Currently, *GIFT* offers a choice of 16 ICA algorithms, many of which are extensions of established methods such as *InfoMax* and *FastICA*.

It can be shown that when $\boldsymbol{X}$ is temporally filtered in a way that can be expressed as a component-wise transformation matrix, the ICA model holds for the filtered data, with the mixing matrix unchanged (the estimated sources will be equivalently filtered, component wise, but not mixed). Thus ICA could be used to estimate A on filtered data (such as low-pass, high-pass, or band-pass filtered data), then W could be applied to unfiltered data to generate the components (Hyvärinen et al., 2001).

Multivariate analysis simulation example

To illustrate the difference between PCA and ICA decomposition of multivariate signals, a small example may be useful. A very effective example for binary data signals was given in Jutten and Herault (1991), but does not directly relate to functional imaging. Therefore, three time series signals were chosen to simulate muscle fMRI data in a primitive way: the data includes a fast component, similar to pulsatility in blood flow; a broad, low-frequency component; and a faster decay, similar to physiological signals observed in the data as shown in Chapter 4. Figure 1.8 shows the three source signals generated, and their arbitrary mixture into three simulated measurements. The mixing matrix, O, was:

$$O = \begin{bmatrix} 1.0 & 0.45 & 0.6 \\ -1.0 & 0.15 & 0.3 \\ 0.5 & 0.30 & -0.1 \end{bmatrix}$$

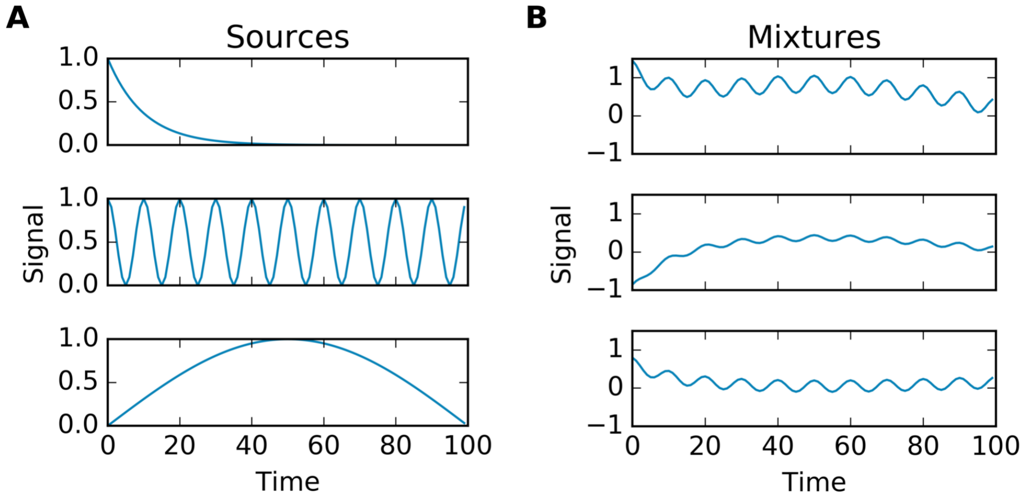

Figure 1.8: Simulated sources and mixtures. (A) Three source signals generated from and exponential decay, a fast sinusoid, and a low frequency sinusoid, respectively. **(B)** Three mixtures generated from the sources using an arbitrary mixing matrix, O.

If $\boldsymbol{X}$ and $\boldsymbol{S}$ are defined with vectors as rows, the relationship is expressed as $\boldsymbol{X} = O\boldsymbol{S}$. Alternatively, if they are column vectors, the relationship is $\boldsymbol{X} = \boldsymbol{S}O^T$. The X data set was plotted as shown in Figure 1.9. This plot illustrates the way the data may be geometrically represented. Each variable, being a simulated time series measurement, is plotted. In fMRI terms, this would be the time series of a spatial voxel. Note that the temporal information is discarded, and the observations become a cloud of data points rather than a temporal sequence.

The mixture was then represented using PCA and ICA (by running `princomp` and `fastica` in Matlab, respectively). An FA representation was not possible, since it requires more degrees of freedom. The three eigenvectors returned from PCA are shown in Figure 1.9, and can be interpreted in terms of the variance of the data set. The three directions associated with the ICA analysis are also shown, but are more difficult to interpret. It then becomes clear that in this geometrical interpretation, the use of methods such as PCA, FA, and ICA to search for components is synonymous with the search for the optimal trio of vectors.

Figure 1.10 shows the components generated from the two methods, and Figure 1.11 shows the mixing matrices. Note that the second ICA component has opposite sign from the original source. This kind of reversal is expected: since

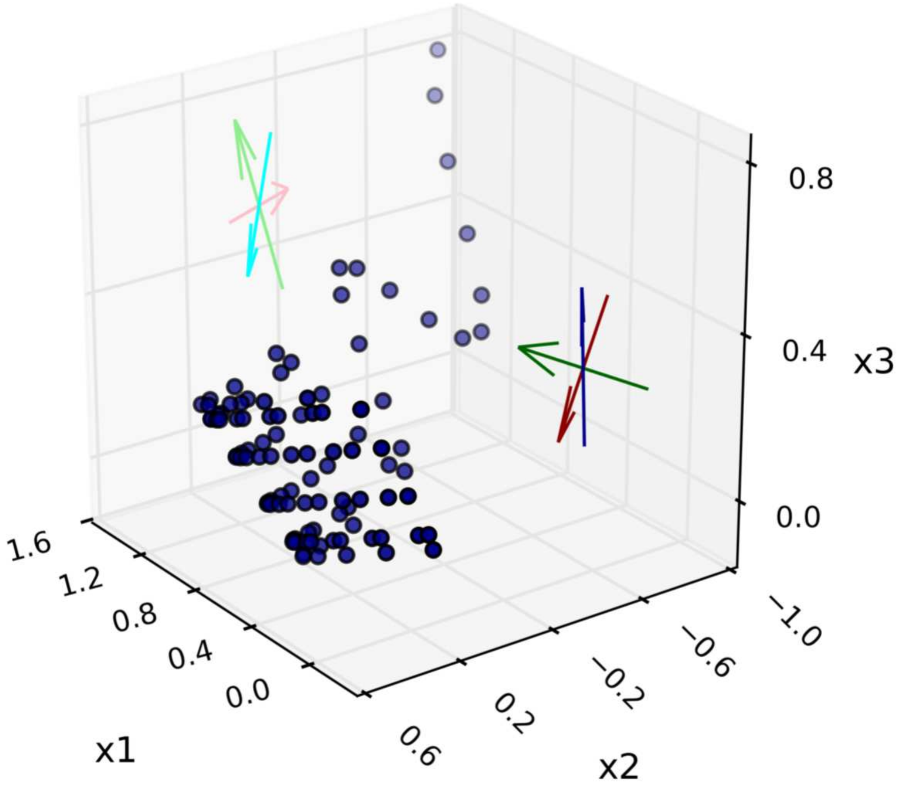

Figure 1.9: Joint mixture from simulation. The simulated mixture matrix, X, plotted with each of the three variables (time series signals) representing a dimension of space. The three principal axes of the PCA model are shown (eigenvectors from columns of $\boldsymbol{V}$), ordered as red, green, blue. The three analogous ICA directions are also shown (columns of $\boldsymbol{W}^T$), ordered as pink, light-green, cyan.

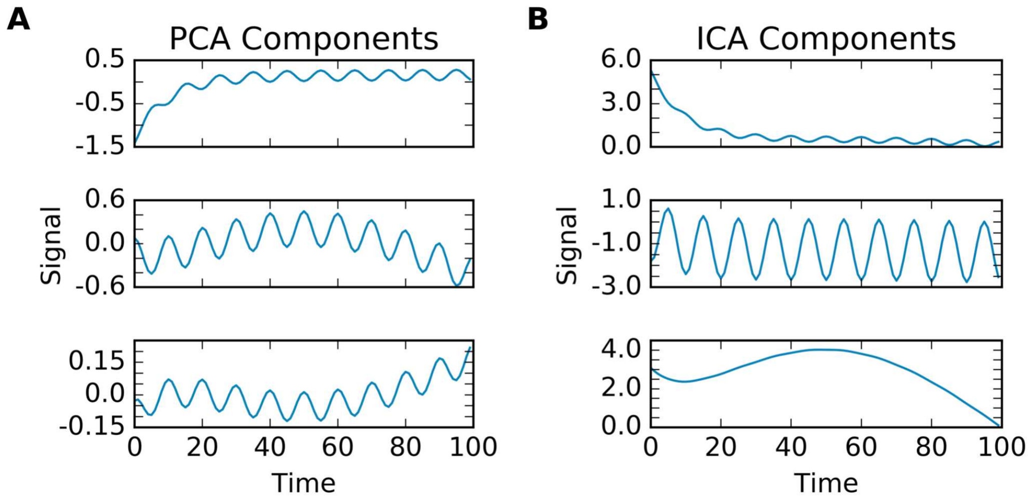

Figure 1.10: **Components from simulation**. **(A)** PCA components. **(B)** ICA components. The PCA components remain mixtures of the sources, since the goal of PCA is simply to represent variance. The ICA components are much more similar to the original sources, illustrating that ICA performs source separation. The ICA result does not perfectly match the original signals, likely because the original signals were not truly independent (or even uncorrelated).

both the sources and the coefficients are unknown in the ICA model, the sources can be determined only up to a scaling factor. In both the components and the mixtures, it can be seen that ICA produces a representation of the original sources with much higher fidelity than PCA. This is not an illustration of the blanket superiority of ICA in general, but does illustrate its better suitability for blind source separation. Applications involving dimension reduction are still better suited to PCA.

Application to muscle BOLD data

Our prior work examined optimal acquisition parameters for skeletal muscle BOLD MRI in the lower leg, in particular comparing spiral and Cartesian acquisition schemes (Davis, 2009). We have also examined the effect of motion without exercise on muscle BOLD data using a conventional block design paradigm (Davis et al., 2009; Davis, 2009). The study showed that conventional motion correction was not adequate to eliminate the effects of motion on the GRE EPI signal during the exercise simulation. This implies that data acquired during exercise can not

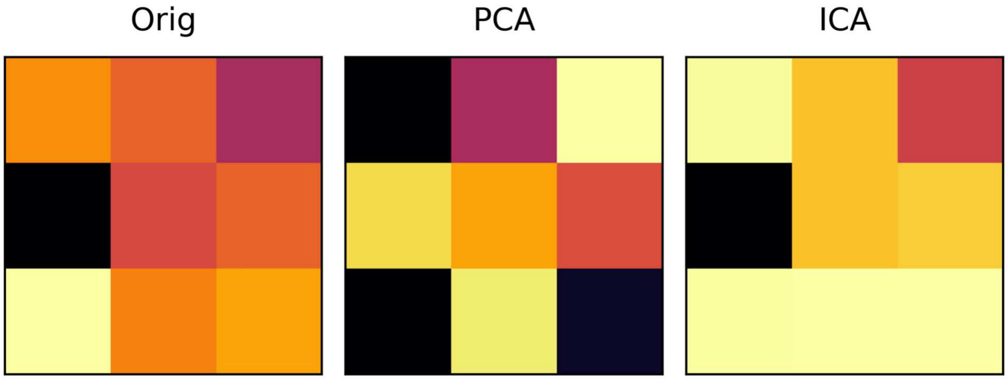

Figure 1.11: **Mixing matrices from simulation**. It can be seen that the ICA mixing matrix, A, is not a perfect copy of the original, O. It is closer than the PCA eigenvectors, though, which bear no resemblance to O. Note that in this figure, the centre column of A had its sign reversed, since the second component can be seen to have opposing sign to the original signal in Fig. 1.10. Colour bars have been intentionally omitted since the scaling of ICA coefficients is arbitrary.

simply be compared to the signal at rest. In a separate abstract, we looked at the power spectral density of muscle BOLD data, showing that certain regions had large contributions of cardiac frequencies (Davis and Noseworthy, 2011). This led to the notion that ROIs in skeletal muscle must be chosen very carefully, in particular avoiding arterioles, if the goal is to obtain signals reflecting only muscle tissue and capillaries.

This earlier experience led us to an experimental design that would acquire Cartesian GRE EPI data and study only the portion following exercise. The one repetition maximum (1RM) test was chosen as a basis for standardizing the exercise based on its simplicity and widespread use. An exercise protocol of 50% of 1RM @ 0.5 Hz for 2.5 minutes was selected based on the practicality of the ergometer in use, and based on initial testing of what subjects could tolerate in repeated scans. The other consideration was that this amount of exercise would stimulate several minutes of unsettled blood volume and oxygenation, providing ample signal for analysis before those parameters returned to baseline levels. Based on this data, we have described a curve fitting scheme to the post-exercise signal from the soleus and gastrocnemius muscle (Davis and Noseworthy, 2013a). We have also described a scheme that attempts to fit a model to the post-exercise BOLD signal

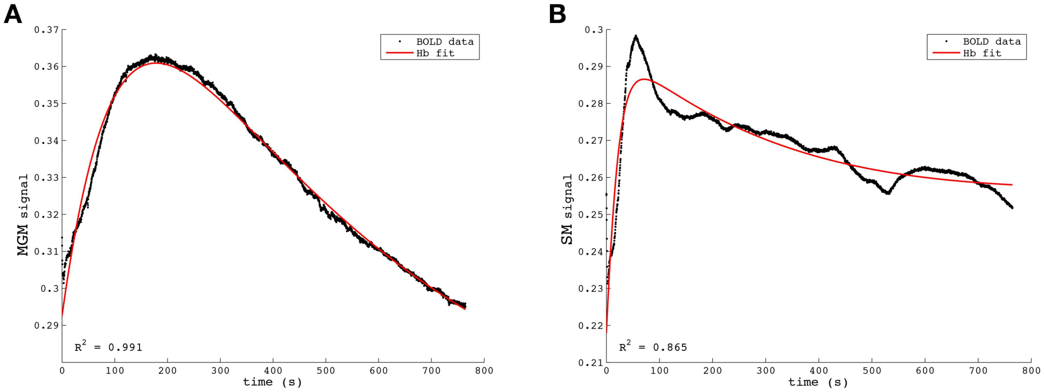

Figure 1.12: Muscle ROI signals. (A) Signal and curve fit from total MGM ROI; **(B)** signal and curve fit from total SM ROI. The mean GRE EPI post-exercise signal is shown along with a curve fit from a model based on prior NIRS studies and the T_2^* of blood, with details given in Davis and Noseworthy (2013b). Care was taken to avoid identifiable vessels when delineating both ROIs. The GM signal could be interpreted as a single response curve, but the SM curve appears to have at least two components, so the model did not provide a good fit.

based on expected blood volume and oxygenation curves. The model was based on previously published NIRS data from other groups, and the expected BOLD signal values in blood (Davis and Noseworthy, 2013b).

Figure 1.12 presents plots from that previous abstract showing the BOLD response and model fits from two muscles. The model did not provide a good fit to SM data, as there appeared to be more than one curve underlying the shape. This indicated that a simple ROI average was not an appropriate strategy, and multivariate processing was warranted to better visualize the signal trends influencing the data.

Moving to the multivariate regime, we attempted to apply PCA to muscle GRE EPI data, as early brain fMRI researchers did (Friston et al., 1994). Thus components of interest were extracted as eigenimages. Though the method showed promise, the maps and associated time courses were difficult to interpret. This was likely because the eigenimages were mixtures representing the predominant variance of the post-exercise signal, rather than underlying physiological processes. Also, the problem of model order remained. The early fMRI literature on motion detrending was also mined for methods to help clean the data (Friston et al., 1996).

Our next attempts to analyze the post-exercise GRE EPI data were to attempt BSS using the *InfoMax* and *FastICA* Matlab toolboxes. These did not prove fruitful, and there are two likely reasons for this. First, the ICA models employed did not include an explicit noise term. Thus, small changes in the temporal signals due to noise could lead to the splitting of components across source maps. Second, the problem of model order selection remained. With no guidance on how to choose q, too many components were extracted, leading to source maps that were uninterpretable. This problem is referred to as *overfitting* (Beckmann and Smith, 2004) or *overlearning* (Hyvärinen et al., 2001). With mild overfitting, components of interest are arbitrarily split into separate source maps. When extreme overfitting occurs, components have the temporal appearance of single spikes or bumps, since they depend more on the data points themselves than the underlying processes generating the data points. This is the problem that *Melodic*'s PICA algorithm is meant to solve, and the results of Chapter 4 demonstrate its effectiveness.

1.7 Problem definition and hypothesis

Motion affects GRE EPI data profoundly, and in several different ways. Previous studies have demonstrated that BOLD imaging can be used to monitor physiological changes in muscle, as noted in Section 1.2. But motion corruption of the signal must be addressed in order to maximize the useful information obtained by the technique. This represents a clear gap in the muscle imaging literature to date, especially given the impact of motion on the GRE EPI signal demonstrated in brain studies. The aim of this thesis is to address that gap by developing image preprocessing and analysis methods that control the effects of motion. Some effects of motion may be treated as artifacts and removed using filtering or multivariate analysis techniques. Other effects of motion may be exploited to extract additional information from muscle GRE EPI data.

It is hypothesized that the processing of muscle GRE EPI data can be improved by developing methods that attend to the unique aspects of the signal arising from muscle. First, it will be shown that motion correction of muscle is inherently different than brain, due to the orientation of the leg vasculature. The through-plane motion of inflowing blood confounds the conventional motion correction tools that are typically used in muscle studies. Second, motion of muscle tissue out of and into the imaged volume during contractions causes signal effects not seen in the brain. These are short duration artifacts in the post-exercise GRE EPI data that can be exploited to map the prior motion of the tissue. Finally, even gradual motion of a subject during relaxation after exercise can cause spurious signals that resemble physiological ones. Using various motion regression techniques and ICA, it will be demonstrated that physiological signals of interest can be definitively separated from the noise.

References

Abdi, H. and L. J. Williams. 2010. “Principal component analysis.” *Wiley Interdiscip Rev Comput Stat* 2: 433–459.

Agur, A. M., V. Ng-Thow-Hing, K. A. Ball, E. Fiume, and N. H. McKee. 2003. “Documentation and three-dimensional modelling of human soleus muscle architecture.” *Clin Anat* 16: 285–293.

Ahlborg, G. and P. Felig. 1982. “Lactate and glucose exchange across the forearm, legs, and splanchnic bed during and after prolonged leg exercise.” *J Clin Invest* 69: 45.

Andersen, P. and A. J. Kroese. 1978. “Capillary supply in soleus and gastrocnemius muscles of man.” *Pflugers Arch* 375: 245–249.

Andersen, P. and B. Saltin. 1985. “Maximal perfusion of skeletal muscle in man.” *J Physiol* 366: 233.

Arampatzis, A., S. Stafilidis, G. DeMonte, K. Karamanidis, G. Morey-Klapsing, and G. P. Brüggemann. 2005. “Strain and elongation of the human gastrocnemius tendon and aponeurosis during maximal plantarflexion effort.” *J Biomech* 38: 833–841.

Bangsbo, J., P. Gollnick, T. Graham, C. Juel, B. Kiens, M. Mizuno, and B. Saltin. 1990. “Anaerobic energy production and o2 deficit-debt relationship during exhaustive exercise in humans.” *J Physiol* 422: 539.

Beckmann, C. F. and S. M. Smith. 2004. “Probabilistic independent component analysis for functional magnetic resonance imaging.” *IEEE Trans Med Imaging* 23: 137–152.

Belardinelli, R., T. J. Barstow, P. Nguyen, and K. Wasserman. 1997. “Skeletal muscle oxygenation and oxygen uptake kinetics following constant work rate exercise in chronic congestive heart failure.” *Am J Cardiol* 80: 1319–1324.

Bell, A. J. and T. J. Sejnowski. 1995. “An information-maximization approach to blind separation and blind deconvolution.” *Neural Comput* 7: 1129–1159.

Bernstein, M. A., K. F. King, and X. J. Zhou. 2004. *Handbook of MRI Pulse Sequences.* Burlington, MA: Elsevier Academic Press.

Blemker, S. S., P. M. Pinsky, and S. L. Delp. 2005. "A 3D model of muscle reveals the causes of nonuniform strains in the biceps brachii." *J Biomech* 38: 657–665.

Blitz, N. M. and D. J. Eliot. 2007. "Anatomical aspects of the gastrocnemius aponeurosis and its insertion: A cadaveric study." *J Foot Ankle Surg* 46: 101–108.

Blitz, N. M. and D. J. Eliot. 2008. "Anatomical aspects of the gastrocnemius aponeurosis and its muscular bound portion: A cadaveric study — part ii." *J Foot Ankle Surg* 47: 533–540.

Bojsen-Møller, J., P. Hansen, P. Aagaard, U. Svantesson, M. Kjaer, and S. P. Magnusson. 2004. "Differential displacement of the human soleus and medial gastrocnemius aponeuroses during isometric plantar flexor contractions in vivo." *J Appl Physiol* 97: 1908–1914.

Broome, D. R. 2008. "Nephrogenic systemic fibrosis associated with gadolinium based contrast agents: a summary of the medical literature reporting." *Eur J Radiol* 66: 230–234.

Brown, R., O. Khegai, and P. Parasoglou. 2016. "Magnetic resonance imaging of phosphocreatine and determination of BOLD kinetics in lower extremity muscles using a dual-frequency coil array." *Sci Rep* 6: 30568.

Bulte, D. P., J. Alfonsi, S. Bells, and M. D. Noseworthy. 2006. "Vasomodulation of skeletal muscle BOLD signal." *J Magn Reson Imaging* 24: 886–90.

Bushberg, J. T., J. A. Seibert, J. Leidholdt, Edwin M., and J. M. Boone. 2012. *The Essential Physics of Medical Imaging.* 3rd edition. Philadelphia, PA, USA: Lippincott Williams & Wilkins.

Buxton, R. B. 2009. *Introduction to Functional Magnetic Resonance Imaging: Principles and Techniques.* 2nd edition. Cambridge, UK: Cambridge University Press.

Caterini, J. E., A. H. Elzibak, E. J. S. Michel, B. W. McCrindle, A. N. Redington, S. Thompson, M. D. Noseworthy, and G. D. Wells. 2015. "Characterizing blood oxygen level-dependent (BOLD) response following in-magnet quadriceps exercise." *MAGMA* 28: 271–278.

Damon, B. M., J. L. Hornberger, M. C. Wadington, D. A. Lansdown, and J. A. Kent-Braun. 2007. "Dual gradient-echo MRI of post-contraction changes in skeletal muscle blood volume and oxygenation." *Magn Reson Med* 57: 670–679.

Daubechies, I., E. Roussos, S. Takerkart, M. Benharrosh, C. Golden, K. D'ardenne, W. Richter, J. Cohen, and J. Haxby. 2009. "Independent component analysis for brain fMRI does not select for independence." *Proc Natl Acad Sci U S A* 106: 10415–10422.

Davis, A. D. 2009. *Optimization of functional magnetic resonance imaging of skeletal muscle.* Master's thesis, McMaster University.

Davis, A. D. and M. D. Noseworthy. 2011. "Fourier analysis of muscle BOLD data after exercise." In "Proc Int Soc Magn Reson Med Sci Meet Exhib," volume 19, p. 7153.

Davis, A. D. and M. D. Noseworthy. 2013a. "Consistency of post-exercise skeletal muscle BOLD response." In "Proc Int Soc Magn Reson Med Sci Meet Exhib," volume 21, p. 1640.

Davis, A. D. and M. D. Noseworthy. 2013b. "Haemoglobin-derived curve fitting to post-exercise muscle BOLD data." In "Proc Int Soc Magn Reson Med Sci Meet Exhib," volume 21, p. 1648.

Davis, A. D., G. D. Wells, B. Falk, and M. D. Noseworthy. 2009. "Twisting motion as a confound to skeletal muscle BOLD." In "Proc Int Soc Magn Reson Med Sci Meet Exhib," volume 17, p. 6351.

Decorte, N., T. Buehler, E. Caldas de Almeida Araujo, A. Vignaud, and P. G. Carlier. 2014. "Noninvasive estimation of oxygen consumption in human calf muscle through combined nmr measurements of asl perfusion and t2 oxymetry." *J Vasc Res* 51: 360–368.

Delp, M. D. 1998. "Differential effects of training on the control of skeletal muscle perfusion." *Med Sci Sports Exerc* 30: 361–374.

Drost, M. R., M. Maenhout, P. J. B. Willems, C. W. J. Oomens, F. P. T. Baaijens, and M. K. C. Hesselink. 2003. "Spatial and temporal heterogeneity of superficial muscle strain during in situ fixed-end contractions." *J Biomech* 36: 1055–1063.

Duteil, S., C. Wary, J. S. Raynaud, V. Lebon, D. Lesage, A. Leroy-Willig, and P. G. Carlier. 2006. "Influence of vascular filling and perfusion on BOLD contrast during reactive hyperemia in human skeletal muscle." *Magn Reson Med* 55: 450–454.

Edwards, R., D. Hill, D. Jones, and P. Merton. 1977. "Fatigue of long duration in human skeletal muscle after exercise." *J Physiol* 272: 769.

Englund, E. K., C. P. Elder, Q. Xu, Z. Ding, and B. M. Damon. 2011. "Combined diffusion and strain tensor MRI reveals a heterogeneous, planar pattern of strain development during isometric muscle contraction." *Am J Physiol Regul Integr Comp Physiol* 300: R1079–R1090.

Englund, E. K., M. C. Langham, C. Li, Z. B. Rodgers, T. F. Floyd, E. R. Mohler, and F. W. Wehrli. 2013. "Combined measurement of perfusion, venous oxygen saturation, and skeletal muscle t 2* during reactive hyperemia in the leg." *J Cardiovasc Magn Reson* 15: 70.

Ferrari, M., M. Muthalib, and V. Quaresima. 2011. "The use of near-infrared spectroscopy in understanding skeletal muscle physiology: recent developments." *Philos Trans A Math Phys Eng Sci* 369: 4577–4590.

Finni, T., J. A. Hodgson, A. M. Lai, V. R. Edgerton, and S. Sinha. 2003. "Nonuniform strain of human soleus aponeurosis-tendon complex during submaximal voluntary contractions in vivo." *J Appl Physiol* 95: 829–837.

Finni, T., J. A. Hodgson, A. M. Lai, V. R. Edgerton, and S. Sinha. 2006. "Muscle synergism during isometric plantarflexion in achilles tendon rupture patients and in normal subjects revealed by velocity-encoded cine phase-contrast MRI." *Clin Biomech* 21: 67–74.

Flamm, S. D., J. Taki, R. Moore, S. F. Lewis, F. Keech, F. Maltais, M. Ahmad, R. Callahan, S. Dragotakes, and N. Alpert. 1990. "Redistribution of regional and organ blood volume and effect on cardiac function in relation to upright exercise intensity in healthy human subjects." *Circulation* 81: 1550–1559.

Friston, K. and C. Büchel. 2007. "Functional connectivity: eigenimages and multivariate analyses." In Friston, K., J. Ashburner, S. Kiebel, T. Nichols, and W. Penny, eds., "Statistical Parametric Mapping," chapter 37, pp. 492 – 507. London: Academic Press.

Friston, K. J., P. Jezzard, and R. Turner. 1994. "Analysis of functional MRI timeseries." *Hum Brain Mapp* 1: 153–171.

Friston, K. J., S. Williams, R. Howard, R. S. Frackowiak, and R. Turner. 1996. "Movement-related effects in fMRI time-series." *Magn Reson Med* 35: 346–355.

Fukunaga, T., Y. Kawakami, S. Kuno, K. Funato, and S. Fukashiro. 1997. "Muscle architecture and function in humans." *J Biomech* 30: 457–463.

Fukunaga, T., R. Roy, F. Shellock, J. Hodgson, and V. Edgerton. 1996. "Specific tension of human plantar flexors and dorsiflexors." *J Appl Physiol* 80: 158–165.

Galbraith, S. M., M. A. Lodge, N. J. Taylor, G. J. Rustin, S. Bentzen, J. J. Stirling, and A. R. Padhani. 2002. "Reproducibility of dynamic contrast-enhanced MRI in human muscle and tumours: comparison of quantitative and semi-quantitative analysis." *NMR Biomed* 15: 132–142.

Gold, G. E., E. Han, J. Stainsby, G. Wright, J. Brittain, and C. Beaulieu. 2004. "Musculoskeletal MRI at 3.0 T: relaxation times and image contrast." *AJR Am J Roentgenol* 183: 343–51.

González-Alonso, J. and J. A. Calbet. 2003. "Reductions in systemic and skeletal muscle blood flow and oxygen delivery limit maximal aerobic capacity in humans." *Circulation* 107: 824–830.

Graham, S. J., M. J. Bronskill, and R. M. Henkelman. 1998. "Time and temperature dependence of mr parameters during thermal coagulation of ex vivo rabbit muscle." *Magn Reson Med* 39: 198–203.

Gray, H. 1918. "Tendons, aponeuroses, and fasciae." In Lewis, W. H., ed., "Anatomy of the Human Body," 20th edition, pp. 376–378. Philadelphia: Lea & Febiger.

Greenhaff, P. L. 2003. "Milestones in human physiology: muscle energy metabolism and blood flow during contraction." *J Physiol* 551: 397–399.

Gregory, C. M., K. Vandenborne, and G. A. Dudley. 2001. "Metabolic enzymes and phenotypic expression among human locomotor muscles." *Muscle Nerve* 24: 387–393.

Haacke, E. M., R. W. Brown, M. R. Thompson, and R. Venkatesan. 1999. *Magnetic Resonance Imaging: Physical Principles and Sequence Design.* New York: John Wiley & Sons.

Hara, Y. 2008. "Deep venous thrombosis in stroke patients during rehabilitation phase." *Keio J Med* 57: 196–204.

Haseler, L. J., M. C. Hogan, and R. S. Richardson. 1999. "Skeletal muscle phosphocreatine recovery in exercise-trained humans is dependent on o2availability." *J Appl Physiol* 86: 2013–2018.

Hodgson, J. A., T. Finni, A. M. Lai, V. R. Edgerton, and S. Sinha. 2006. "Influence of structure on the tissue dynamics of the human soleus muscle observed in MRI studies during isometric contractions." *J Morphol* 267: 584–601.

Hotelling, H. 1933. "Analysis of a complex of statistical variables into principal components." *J Educ Psychol* 24: 417.

Hyvärinen, A., J. Karhunen, and E. Oja. 2001. *Independent Component Analysis.* Toronto: John Wiley & Sons.

Hyvärinen, A. and E. Oja. 2000. "Independent component analysis: algorithms and applications." *Neural Netw* 13: 411–430.

Jacobi, B., G. Bongartz, S. Partovi, A.-C. Schulte, M. Aschwanden, A. B. Lumsden, M. G. Davies, M. Loebe, G. P. Noon, S. Karimi, J. K. Lyo, D. Staub, R. W. Huegli, and D. Bilecen. 2012. "Skeletal muscle BOLD MRI: From underlying physiological concepts to its usefulness in clinical conditions." *J Magn Reson Imaging* 35: 1253–1265.

Jolliffe, I. T. 2002. *Principal Component Analysis.* 2 edition. New York: Springer.

Jutten, C. and J. Herault. 1991. "Blind separation of sources, part i: An adaptive algorithm based on neuromimetic architecture." *Signal Process* 24: 1–10.

Kawakami, Y., Y. Ichinose, and T. Fukunaga. 1998. "Architectural and functional features of human triceps surae muscles during contraction." *J Appl Physiol* 85: 398–404.

Kayar, S., H. Hoppeler, J. H. Jones, K. Longworth, R. Armstrong, M. Laughlin, S. Lindstedt, J. Bicudo, K. Groebe, and C. Taylor. 1994. "Capillary blood transit time in muscles in relation to body size and aerobic capacity." *J Exp Biol* 194: 69–81.

Kaye, E. A., S. Josan, A. Lu, J. Rosenberg, B. L. Daniel, and K. B. Pauly. 2010. "Consistency of signal intensity and t2* in frozen ex vivo heart muscle, kidney, and liver tissue." *J Magn Reson Imaging* 31: 719–724.

Kenny, G. P., F. D. Reardon, W. Zaleski, M. L. Reardon, F. Haman, and M. B. Ducharme. 2003. "Muscle temperature transients before, during, and after exercise measured using an intramuscular multisensor probe." *J Appl Physiol* 94: 2350–2357.

Kindig, C. A., T. E. Richardson, and D. C. Poole. 2002. "Skeletal muscle capillary hemodynamics from rest to contractions: implications for oxygen transfer." *J Appl Physiol* 92: 2513–2520.

Kinugasa, R., J. A. Hodgson, V. R. Edgerton, and S. Sinha. 2012. "Asymmetric deformation of contracting human gastrocnemius muscle." *J Appl Physiol* 112: 463–470.

Kinugasa, R., D. Shin, J. Yamauchi, C. Mishra, J. A. Hodgson, V. R. Edgerton, and S. Sinha. 2008. "Phase-contrast MRI reveals mechanical behavior of superficial and deep aponeuroses in human medial gastrocnemius during isometric contraction." *J Appl Physiol* 105: 1312–1320.

Korthuis, R. J. 2011. "Skeletal muscle circulation." In Granger, D. N. and J. P. Granger, eds., "Colloquium Series on Integrated Systems Physiology: From Molecule to Function to Disease," volume 3, pp. 1–144. Morgan and Claypool Life Sciences.

Kumar, Y., V. Wadhwa, L. Phillips, P. Pezeshk, and A. Chhabra. 2016. "MR imaging of skeletal muscle signal alterations: Systematic approach to evaluation." *Eur J Radiol* 85: 922–935.

Labs, K. H., M. R. Nehler, M. Roessner, K. A. Jaeger, and W. R. Hiatt. 1999. "Reliability of treadmill testing in peripheral arterial disease: a comparison of a constant load with a graded load treadmill protocol." *Vasc Med* 4: 239–46.

Laughlin, M. and B. Roseguini. 2008. "Mechanisms for exercise training-induced increases in skeletal muscle blood flow capacity: differences with interval sprint training versus aerobic endurance training." *J Physiol Pharmacol* 59: 71.

Laughlin, M. H. 1987. "Skeletal muscle blood flow capacity: role of muscle pump in exercise hyperemia." *Am J Physiol Heart Circ Physiol* 253: H993–H1004.

Laughlin, M. H. and R. Armstrong. 1984. "Muscle blood flow during locomotory exercise." *Exerc Sport Sci Rev* 13: 95–136.

Laughlin, M. H., R. J. Korthuis, D. J. Duncker, and R. J. Bache. 2010. "Control of blood flow to cardiac and skeletal muscle during exercise." In "Comprehensive Physiology," John Wiley & Sons.

Lebon, V., C. Brillault-Salvat, G. Bloch, A. Leroy-Willig, and P. G. Carlier. 1998a. "Evidence of muscle BOLD effect revealed by simultaneous interleaved gradient-echo NMRI and myoglobin NMRS during leg ischemia." *Magn Reson Med* 40: 551–558.

Lebon, V., P. G. Carlier, C. Brillault-Salvat, and A. Leroy-Willig. 1998b. "Simultaneous measurement of perfusion and oxygenation changes using a multiple gradient-echo sequence: application to human muscle study." *Magn Reson Imaging* 16: 721–729.

Ledermann, H. P., H.-G. Heidecker, A.-C. Schulte, C. Thalhammer, M. Aschwanden, K. A. Jaeger, K. Scheffler, and D. Bilecen. 2006a. "Calf muscles imaged at BOLD MR: correlation with TcPO2 and flowmetry measurements during ischemia and reactive hyperemia–initial experience." *Radiology* 241: 477–484.

Ledermann, H.-P., A.-C. Schulte, H.-G. Heidecker, M. Aschwanden, K. A. Jäger, K. Scheffler, W. Steinbrich, and D. Bilecen. 2006b. "Blood oxygenation level-dependent magnetic resonance imaging of the skeletal muscle in patients with peripheral arterial occlusive disease." *Circulation* 113: 2929–2935.

Ljunggren, S. 1983. “A simple graphical representation of Fourier-based imaging methods.” *J Magn Reson* 54: 338–343.

Ma, H. T., J. F. Griffith, C. Ye, D. K. Yeung, X. Xing, P.-C. Leung, and J. Yuan. 2014. “BOLD effect on calf muscle groups in elderly females with different bone mineral density.” In “Engineering in Medicine and Biology Society (EMBC), 2014 36th Annual International Conference of the IEEE,” pp. 5607–5610. IEEE.

MacDonald, M. J., J. K. Shoemaker, M. E. Tschakovsky, and R. L. Hughson. 1998. “Alveolar oxygen uptake and femoral artery blood flow dynamics in upright and supine leg exercise in humans.” *J Appl Physiol* 85: 1622–1628.

MacDonald, M. J., M. A. Tarnopolsky, H. J. Green, and R. L. Hughson. 1999. “Comparison of femoral blood gases and muscle near-infrared spectroscopy at exercise onset in humans.” *J Appl Physiol* 86: 687–693.

Mansfield, P. 1977. “Multi-planar image formation using NMR spin echoes.” *J Phys C: Solid State Phys* 10: L55–L58.

Martinez, W. L. and A. R. Martinez. 2005. *Exploratory Data Analysis with MATLAB*. New York: Chapman & Hall/CRC Press.

Matsui, S., N. Tamura, T. Hirakawa, S. Kobayashi, N. Takekoshi, and E. Murakami. 1995. “Assessment of working skeletal muscle oxygenation in patients with chronic heart failure.” *Am Heart J* 129: 690–695.

McCully, K. K. and T. Hamaoka. 2000. “Near-infrared spectroscopy: What can it tell us about oxygen saturation in skeletal muscle?” *Exerc Sport Sci Rev* 28: 123–127.

McRobbie, D. W., E. A. Moore, M. J. Graves, and M. R. Graves. 2006. *MRI; From Picture to Proton.* 2nd edition. New York: Cambridge University Press.

Meissner, M. H. 2005. “Lower extremity venous anatomy.” *Semin Intervent Radiol* 22: 147–156.

Meyer, R., K. K. McCully, R. W. Reid, and B. Prior. 2001. “BOLD MRI and NIRS detection of transient hyperemia after single skeletal muscle contractions.” *Proc Int Soc Magn Reson Med Sci Meet Exhib* 9: 135.

Meyer, R. A., T. F. Towse, R. W. Reid, R. C. Jayaraman, R. W. Wiseman, and K. K. McCully. 2004. “BOLD MRI mapping of transient hyperemia in skeletal muscle after single contractions.” *NMR Biomed* 17: 392–398.

Miura, H., K. McCully, L. Hong, S. Nioka, and B. Chance. 2001. “Regional difference of muscle oxygen saturation and blood volume during exercise determined by near infrared imaging device.” *Jpn J Physiol* 51: 599–606.

Molé, P. A., Y. Chung, T. K. Tran, N. Sailasuta, R. Hurd, and T. Jue. 1999. “Myoglobin desaturation with exercise intensity in human gastrocnemius muscle.” *Am J Physiol Regul Integr Comp Physiol* 277: R173–R180.

Möller, P. and C. Sylven. 1981. “Myoglobin in human skeletal muscle.” *Scand J Clin Lab Invest* 41: 479–482.

Monti, R. J., R. R. Roy, J. A. Hodgson, and V. R. Edgerton. 1999. “Transmission of forces within mammalian skeletal muscles.” *J Biomech* 32: 371–380.

Muller, M. D., Z. Li, C. T. Sica, J. C. Luck, Z. Gao, C. A. Blaha, A. E. Cauffman, A. J. Ross, N. J. Winkler, M. D. Herr et al. 2016. “Muscle oxygenation during dynamic plantar flexion exercise: combining BOLD MRI with traditional physiological measurements.” *Physiol Rep* 4: e13004.

Muramatsu, T., T. Muraoka, D. Takeshita, Y. Kawakami, Y. Hirano, and T. Fukunaga. 2001. “Mechanical properties of tendon and aponeurosis of human gastrocnemius muscle in vivo.” *J Appl Physiol* 90: 1671–1678.

Murrant, C. and I. Sarelius. 2000. “Coupling of muscle metabolism and muscle blood flow in capillary units during contraction.” *Acta Physiol Scand* 168: 531–541.

Murray, M. P., G. N. Guten, J. M. Baldwin, and G. M. Gardner. 1976. “A comparison of plantar flexion torque with and without the triceps surae.” *Acta Orthop Scand* 47: 122–124.

Nikolaidis, M. G., A. Z. Jamurtas, V. Paschalis, I. G. Fatouros, Y. Koutedakis, and D. Kouretas. 2008. “The effect of muscle-damaging exercise on blood and skeletal muscle oxidative stress.” *Sports Med* 38: 579–606.

Nishii, T., A. K. Kono, M. Nishio, K. Kyotani, K. Nishiyama, and K. Sugimura. 2015a. “Dynamic blood oxygen level-dependent MR imaging of muscle: comparison of postocclusive reactive hyperemia in young smokers and nonsmokers.” *Magn Reson Med Sci* 14: 275–283.

Nishii, T., A. K. Kono, M. Nishio, K. Kyotani, K. Nishiyama, and K. Sugimura. 2015b. “Evaluation of blood volume by use of blood oxygen level-dependent magnetic resonance imaging in a cuff-compression model: usefulness of calculated echo time image.” *Jpn J Radiol* 33: 441–447.

Noseworthy, M. D., D. P. Bulte, and J. Alfonsi. 2003. “BOLD magnetic resonance imaging of skeletal muscle.” *Semin Musculoskelet Radiol* 7: 307–15.

Noseworthy, M. D., A. D. Davis, and A. H. Elzibak. 2010. “Advanced MR imaging techniques for skeletal muscle evaluation.” *Semin Musculoskelet Radiol* 14: 257–268.

Ogawa, S., T. M. Lee, A. S. Nayak, and P. Glynn. 1990. "Oxygenation-sensitive contrast in magnetic resonance image of rodent brain at high magnetic fields." *Magn Reson Med* 14: 68–78.

Oomens, C. W. J., M. Brekelmans, and F. P. T. Baaijens. 2009. "The mechanical behaviour of fibres." In "Biomechanics: Concepts and Computation," pp. 50–68. Cambridge, UK: Cambridge University Press.

Ordway, G. A. and D. J. Garry. 2004. "Myoglobin: an essential hemoprotein in striated muscle." *J Exp Biol* 207: 3441–3446.

Otto, J. M., H. E. Montgomery, and T. Richards. 2013. "Haemoglobin concentration and mass as determinants of exercise performance and of surgical outcome." *Extrem Physiol Med* 2: 33.

Pappas, G. P., D. S. Asakawa, S. L. Delp, F. E. Zajac, and J. E. Drace. 2002. "Nonuniform shortening in the biceps brachii during elbow flexion." *J Appl Physiol* 92: 2381–2389.

Partovi, S., A.-C. Schulte, M. Aschwanden, D. Staub, D. Benz, S. Imfeld, B. Jacobi, P. Broz, K. A. Jäger, M. Takes et al. 2012a. "Impaired skeletal muscle microcirculation in systemic sclerosis." *Arthritis Res Ther* 14: R209.

Partovi, S., A.-C. Schulte, B. Jacobi, M. Klarhöfer, A. B. Lumsden, M. Loebe, M. G. Davies, G. P. Noon, C. Karmonik, L. Zipp, G. Bongartz, and D. Bilecen. 2012b. "Blood oxygenation level-dependent (BOLD) MRI of human skeletal muscle at 1.5 and 3 T." *J Magn Reson Imaging* 35: 1227–1232.

Pauling, L. and C. D. Coryell. 1936. "The magnetic properties and structure of hemoglobin, oxyhemoglobin and carbonmonoxyhemoglobin." *Proc Natl Acad Sci U S A* 22: 210–216.

Poole, D. C., S. W. Copp, S. K. Ferguson, and T. I. Musch. 2013. "Skeletal muscle capillary function: contemporary observations and novel hypotheses." *Exp Physiol* 98: 1645–1658.

Price, T. B., G. Kamen, B. M. Damon, C. A. Knight, B. Applegate, J. C. Gore, K. Eward, and J. F. Signorile. 2003. "Comparison of MRI with EMG to study muscle activity associated with dynamic plantar flexion." *Magn Reson Imaging* 21: 853–61.

Rådegran, G. and B. Saltin. 1999. "Nitric oxide in the regulation of vasomotor tone in human skeletal muscle." *Am J Physiol Heart Circ Physiol* 276: H1951–H1960.

Raitakari, M., M. Knuuti, U. Ruotsalainen, H. Laine, P. Makea, M. Teras, H. Sipila, T. Niskanen, O. Raitakari, H. Iida et al. 1995. “Insulin increases blood volume in human skeletal muscle: studies using [15o] co and positron emission tomography.” *Am J Physiol Endocrinol Metab* 269: E1000–E1005.

Richardson, R. S., E. A. Noyszewski, K. F. Kendrick, J. S. Leigh, and P. D. Wagner. 1995. “Myoglobin o2 desaturation during exercise. evidence of limited o2 transport.” *J Clin Invest* 96: 1916.

Rieke, V. and K. Butts Pauly. 2008. “Mr thermometry.” *J Magn Reson Imaging* 27: 376–390.

Robson, M. D. and G. M. Bydder. 2006. “Clinical ultrashort echo time imaging of bone and other connective tissues.” *NMR Biomed* 19: 765–780.

Rodgers, J. L., W. A. Nicewander, and L. Toothaker. 1984. “Linearly independent, orthogonal, and uncorrelated variables.” *Am Stat* 38: 133–134.

Saltin, B., A. t. Gagge, and J. Stolwijk. 1968. “Muscle temperature during submaximal exercise in man.” *J Appl Physiol* 25: 679–688.

Saltin, B., G. Rådegran, M. Koskolou, and R. Roach. 1998. “Skeletal muscle blood flow in humans and its regulation during exercise.” *Acta Physiol* 162: 421–436.

Sanchez, O. A., E. A. Copenhaver, C. P. Elder, and B. M. Damon. 2010. “Absence of a significant extravascular contribution to the skeletal muscle BOLD effect at 3 T.” *Magn Reson Med* 64: 527–535.

Schewzow, K., M. Andreas, E. Moser, M. Wolzt, and A. I. Schmid. 2013. “Automatic model-based analysis of skeletal muscle BOLD-MRI in reactive hyperemia.” *J Magn Reson Imaging* 38: 963–969.

Schulte, A.-C., M. Aschwanden, and D. Bilecen. 2008. “Calf muscles at blood oxygen level-dependent MR imaging: aging effects at postocclusive reactive hyperemia.” *Radiology* 247: 482–489.

Segal, S. S. 2005. “Regulation of blood flow in the microcirculation.” *Microcirculation* 12: 33–45.

Shin, D. D., J. A. Hodgson, V. R. Edgerton, and S. Sinha. 2009. “In vivo intramuscular fascicle-aponeuroses dynamics of the human medial gastrocnemius during plantarflexion and dorsiflexion of the foot.” *J Appl Physiol* 107: 1276–1284.

Shoemaker, J., J. Halliwill, R. Hughson, and M. J. Joyner. 1997. “Contributions of acetylcholine and nitric oxide to forearm blood flow at exercise onset and recovery.” *Am J Physiol Heart Circ Physiol* 273: H2388–H2395.

Sinha, S., J. A. Hodgson, T. Finni, A. M. Lai, J. Grinstead, and V. R. Edgerton. 2004. "Muscle kinematics during isometric contraction: Development of phase contrast and spin tag techniques to study healthy and atrophied muscles." *J Magn Reson Imaging* 20: 1008–1019.

Sinha, S., D. D. Shin, J. A. Hodgson, R. Kinugasa, and V. R. Edgerton. 2012. "Computer-controlled, mr-compatible foot-pedal device to study dynamics of the muscle tendon complex under isometric, concentric, and eccentric contractions." *J Magn Reson Imaging* 36: 498–504.

Sjogaard, G., R. P. Adams, and B. Saltin. 1985. "Water and ion shifts in skeletal muscle of humans with intense dynamic knee extension." *Am J Physiol Regul Integr Comp Physiol* 248: R190–R196.

Slade, J. M., T. F. Towse, V. V. Gossain, and R. A. Meyer. 2011. "Peripheral microvascular response to muscle contraction is unaltered by early diabetes but decreases with age." *J Appl Physiol* 111: 1361–1371.

Snyder, G. K. and B. A. Sheafor. 1999. "Red blood cells: Centerpiece in the evolution of the vertebrate circulatory system." *Am Zool* 39: 189.

Spiess, A.-N. and N. Neumeyer. 2010. "An evaluation of R2 as an inadequate measure for nonlinear models in pharmacological and biochemical research: a Monte Carlo approach." *BMC pharmacology* 10: 1–11.

Stacy, M. R., C. M. Caracciolo, M. Qiu, P. Pal, T. Varga, R. T. Constable, and A. J. Sinusas. 2016. "Comparison of regional skeletal muscle tissue oxygenation in college athletes and sedentary control subjects using quantitative BOLD MR imaging." *Physiol Rep* 4: e12903.

Taylor, D. S. 1939. "The magnetic properties of myoglobin and ferrimyoglobin, and their bearing on the problem of the existence of magnetic interactions in hemoglobin." *J Am Chem Soc* 61: 2150–2154.

Tipping, M. E. and C. M. Bishop. 1999. "Mixtures of probabilistic principal component analyzers." *Neural Comput* 11: 443–482.

Tonon, C., L. L. Gramegna, and R. Lodi. 2012. "Magnetic resonance imaging and spectroscopy in the evaluation of neuromuscular disorders and fatigue." *Neuromuscul Disord* 22: S187–S191.

Torricelli, A., V. Quaresima, A. Pifferi, G. Biscotti, L. Spinelli, P. Taroni, M. Ferrari, and R. Cubeddu. 2004. "Mapping of calf muscle oxygenation and haemoglobin content during dynamic plantar flexion exercise by multi-channel time-resolved near-infrared spectroscopy." *Phys Med Biol* 49: 685.

Towse, T. F., B. T. Childs, S. A. Sabin, E. C. Bush, C. P. Elder, and B. M. Damon. 2016a. "Comparison of muscle BOLD responses to arterial occlusion at 3 and 7 tesla." *Magn Reson Med* 75: 1333–1340.

Towse, T. F., C. P. Elder, E. C. Bush, S. W. Klockenkemper, J. T. Bullock, R. D. Dortch, and B. M. Damon. 2016b. "Post-contractile BOLD contrast in skeletal muscle at 7 T reveals inter-individual heterogeneity in the physiological responses to muscle contraction." *NMR Biomed* 29: 1720–1728.

Towse, T. F., J. M. Slade, J. A. Ambrose, M. C. DeLano, and R. A. Meyer. 2011. "Quantitative analysis of the postcontractile blood-oxygenation-level-dependent (BOLD) effect in skeletal muscle." *J Appl Physiol* 111: 27–39.

Towse, T. F., J. M. Slade, and R. A. Meyer. 2005. "Effect of physical activity on MRI-measured blood oxygen level-dependent transients in skeletal muscle after brief contractions." *J Appl Physiol* 99: 715–722.

Trotter, J. A. 2002. "Structure-function considerations of muscle-tendon junctions." *Comp Biochem Physiol A Mol Integr Physiol* 133: 1127–1133.

Truijen, J., Y. Kim, C. Krediet, W. Stok, R. Kölgen, W. Colier, N. Secher, and J. van Lieshout. 2012. "Orthostatic leg blood volume changes assessed by near-infrared spectroscopy." *Exp Physiol* 97: 353–361.

Van Leeuwen, B., G. Barendsen, J. Lubbers, and L. De Pater. 1992. "Calf blood flow and posture: Doppler ultrasound measurements during and after exercise." *J Appl Physiol* 72: 1675–1680.

Vandenborne, K., G. Walter, L. Ploutz-Snyder, R. Staron, A. Fry, K. De Meirleir, G. Dudley, and J. Leigh. 1995. "Energy-rich phosphates in slow and fast human skeletal muscle." *Am J Physiol Cell Physiol* 268: C869–C876.

Walløe, L. and J. Wesche. 1988. "Time course and magnitude of blood flow changes in the human quadriceps muscles during and following rhythmic exercise." *J Physiol* 405: 257.

Wigmore, D. M., B. M. Damon, D. M. Pober, and J. A. Kent-Braun. 2004. "MRI measures of perfusion-related changes in human skeletal muscle during progressive contractions." *J Appl Physiol* 97: 2385–2394.

Zhong, X., F. H. Epstein, B. S. Spottiswoode, P. A. Helm, and S. S. Blemker. 2008. "Imaging two-dimensional displacements and strains in skeletal muscle during joint motion by cine dense mr." *J Biomech* 41: 532–540.

Chapter 2

Motion and distortion correction of skeletal muscle echo planar images

Preface

The following chapter has been published previously, and is used with permission of the journal. The article can be accessed via its DOI at `http://dx.doi.org/10.1016/j.mri.2016.03.003`, and the full citation is:

> Davis, A. D. and M. D. Noseworthy. 2016. "Motion and distortion correction of skeletal muscle echo planar images." *Magnetic Resonance Imaging* 34: 832–838.

This chapter includes a discussion of preprocessing techniques for skeletal muscle GRE EPI images. In many ways, acquiring and examining such images in skeletal muscle is no different than in the brain, where there exists a robust variety of software packages for preprocessing and analysis. Two areas were identified in which the tools developed for brain were not appropriate for muscle: motion correction and EPI distortion correction. This chapter includes a discussion of the reasons the brain tools fail on muscle data, and a description of the solutions. Links to the software that was developed are included for future use by skeletal muscle MRI researchers.

Abstract

This paper examines two artifacts facing researchers who use gradient echo (GRE) echo planar imaging (EPI) for time series studies of skeletal muscles in limbs. The first is through-plane blood flow during the acquisition, causing a vessel motion artifact that inhibits proper motion correction of the data. The second is distortion of EPI images caused by B_0 field inhomogeneities. Though software tools are available for correcting these artifacts in brain EPI images, the tools do not perform well on muscle images. The severity of the two artifacts was described using image similarity measures, and the data was processed with both a conventional motion correction program and custom written tools. The conventional program did not perform well on the limb images, in fact significantly degrading image quality in some trials. Data is presented which proves that arterial pulsatile signal caused the impairment in motion correction. The new tools were shown to perform much better, achieving substantial motion correction and distortion correction of the muscle EPI images.

2.1 Introduction

gradient echo (GRE) echo planar imaging (EPI) is often employed to examine skeletal muscles in research studies. Authors are commonly interested in the blood oxygenation level dependent (BOLD) effect in health and disease, through exercise and ischemic tests (Carlier et al., 2006; Noseworthy et al., 2010). This paper discusses solutions to two challenges encountered in EPI imaging of muscle that are not encountered when imaging the brain: through-plane arterial blood flow and a lack of software tools for preprocessing muscle images.

Vessel motion artifact

The first problem salient to this paper occurs when the lower leg is imaged axially, with blood flowing through-plane in three arteries entering the imaging plane at a right angle. When an EPI time series of this type is visualized, the arteries appear to vary in brightness and oscillate across the image by several millimetres from one time point to the next. The anterior tibial, posterior tibial, and peroneal arteries have fast flow at some points in the cardiac cycle, causing increased signal intensity due to the inflow or time-of-flight (TOF) effect (McRobbie et al., 2007). This accounts for the varied brightness. The apparent motion is more difficult to explain, but can be understood by referring to a pulse sequence diagram for GRE EPI (Buxton, 2009). Since the flow is through-plane (in the z-direction), only the slice select gradient could cause a phase accumulation in the flowing spins. Flow with constant velocity during such a bipolar gradient pulse causes a phase shift to develop that is proportional to velocity (Haacke et al., 1999). Because of this phase shift in the intra-arterial spins in frames acquired during fast flow, the vessels appear displaced compared to their true location after EPI reconstruction.

The vessel motion artifact is hypothesized to be problematic for image motion correction, since linear registration schemes will tend to align the bright arteries across frames and drag the rest of the image along with the artifactual motion. This may lead to a time series of images with motion introduced by the software intended to perform motion correction, degrading image quality instead of improving it.

To the best of the authors' knowledge, this is the first time the arterial inflow confound to MR motion correction has been described in the literature. This problem is likely to be encountered by researchers in the future as the use of GRE EPI to study muscle continues. The problem of apparent vessel motion due to through-plane flow may be mitigated by applying saturation bands inferior and superior to axially acquired slices, as is commonly done in TOF studies to eliminate venous flow signal. This decreases the signal from inflowing blood to make the artifact less apparent. This strategy is unlikely to completely eliminate the artifact, however, since the saturation of spins adjacent to the imaging slice is imperfect. Spins from this region as well as from the imaging slice itself may still be excited and produce a TOF artifact. If the artifact is still present with spatial saturation bands in place, processing schemes may be employed to de-weight the area of the arteries or hide them from the registration optimizer during motion correction.

EPI distortion

The second problem addressed in this paper is the high sensitivity of GRE EPI imaging to B_0 field variations. The relatively long time (approximately 50 ms) that the radio-frequency (RF) read-out window is open during an EPI scan causes artifacts; these manifest as blurring in spiral images, or spatial shift in the phase encoding direction in the blipped Cartesian EPI images used in this study as well as many others. The distortion (warp) artifact due to B_0 field variations in EPI images is well known and has been described previously (Jezzard and Balaban, 1995), and an algorithm for correction of the images been developed (Cusack et al., 2003). Software tools implementing GRE EPI unwarping exist, but are typically designed for brain images. One such widely used tool is FUGUE from the FSL toolbox (Jenkinson et al., 2012). The brain-centric design is evident given that a three dimensional (3D) volume matching the size of a human head is expected, and slices at the margins may be discarded. It also performs skull stripping and 3D registration which has unpredictable results on small field-of-view limb data, resulting in partially or completely lost slices. Presumably as a result of the lack of available tools, this significant GRE EPI artifact is not usually addressed in muscle imaging studies (Noseworthy et al., 2010); a B_0 field map correction has been applied successfully to forearm DTI, however (Froeling et al., 2012). When EPI images are unwarped, co-registration of functional and anatomical data may be improved, allowing high quality regions of interest (ROIs) drawn on anatomical images to be applied to functional data.

The purpose of this paper is to draw attention to the severity of these two problems facing GRE EPI studies of muscle, and to explain solutions for overcoming them.

2.2 Materials and Methods

Image acquisition

GRE EPI time series data was collected with approval from our local institutional review board using a 3T GE HD Signa MR scanner with a single channel, receive-only, GPFLEX coil (GE Healthcare, Milwaukee, WI). Six male volunteers participated (mean age 31 ± 9 years). Subjects were positioned in a custom-built MR compatible exercise ergometer for the scanning session (Figure 2.1). Following localization, second order shimming, and anatomical imaging, three 10 mm thick, axial

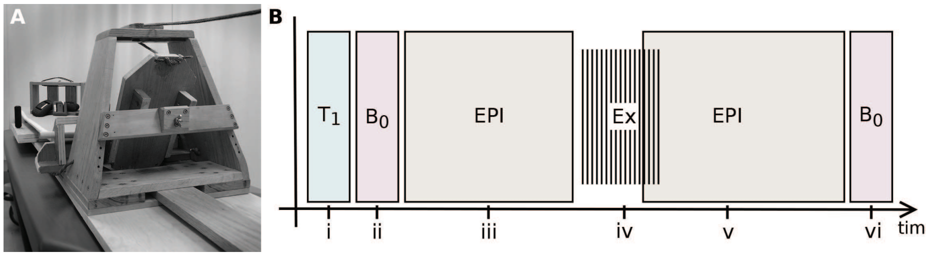

Figure 2.1: Experiment description. **(A)** The photo shows the exercise ergometer used in this study. The apparatus is pictured outside the magnet, with weights for adding resistance visible in the background. **(B)** The diagram shows the events that occurred during an experimental trial (not to scale): **(i)** Subject attached to ergometer in scanner, anatomical images acquired (see section 2.2 for details); **(ii)** Two GRE images acquired for B_0 map creation; **(iii)** Ten min GRE EPI time series images acquired (*rest* condition); **(iv)** Plantar flexion exercise for 2.5 min; **(v)** GRE EPI images acquired. Images acquired during exercise were discarded, leaving 12.5 min time series (*post-ex* condition); **(vi)** Two additional GRE images acquired for B_0 map creation.

slices were acquired with a single-shot gradient echo EPI pulse sequence (Ljunggren, 1983) at the largest cross section of the right leg calf muscles (FOV = 16 cm, matrix size (MS) = 64×64, $T_E = 35$ ms, $T_R = 250$ ms, $\alpha = 33°$, receive bandwidth (rBW) = 500 kHz). The long T_E was used to match typical values of BOLD muscle studies. Spatial saturation bands (40 mm thick) were prescribed continuously above and below the imaged volume to reduce artifacts produced by through-plane flowing blood. For each EPI image series acquired, a pair of fast spoiled gradient echo (FSPGR) images were acquired to generate B_0 field maps from the phase images ($T_E = 4.55/6.82$ ms for $\Delta T_E = 2.27$ ms; MS = 128×128; FOV, T_R, α matched EPI images; rBW = 62.5 kHz). EPI images were acquired before, during, and after exercise. First, 10 min of baseline data was acquired before the start of exercise. Next, isotonic plantar flexion exercise (2.5 min of dynamic (0.5 Hz) plantar flexion at 50% of a subject's previously measured one-repetition maximum) commenced, and image acquisition was started with 30 s of exercise remaining. Data acquisition continued after exercise for 12.5 min. This time series was examined for each subject, and all exercise frames were removed. Thus, two sets of GRE EPI time series data were acquired from each subject: the 10 min pre-exercise data set (denoted *rest*), and the 12.5 min data set immediately following exercise (called *post-ex*). A diagram of the experiment timeline is shown in Figure 2.1.

Image post-processing

Although spatial saturation bands were applied, arterial flow artifacts were still present with enough severity to spoil motion correction (Figure 2.2). Thus, steps were taken to remove the influence of the artery voxels on the registration. A hand drawn binary mask was used which applied a value of zero (i.e. `False`) to the area around three major through-plane arteries in the lower leg and a value of one (i.e. `True`) elsewhere. The masked area was roughly elliptical, with dimensions 20 × 50 mm on each slice, masking approximately 5% of image. The mask was applied to the cost function during registration, which caused the registration algorithm to ignore the areas of the arteries when optimizing the motion correction parameters. Masking the cost function is an improvement over masking the images themselves, as it does not generate artificial edges which may confound the motion correction process. A conservative intensity based mask was also generated to eliminate the image background areas, which contained phase ghosts capable of influencing registration. The motion correction scheme was implemented in a shell script (`mocorib` – **mo**tion **cor**rection with **i**nflowing **b**lood) using FSL's FLIRT tool for registration (Jenkinson and Smith, 2001; Jenkinson et al., 2002), as well as other command line utilities from the FSL and AFNI toolboxes (Jenkinson et al., 2012; Cox, 1996). Given that FLIRT is not optimized for motion correction (especially with respect to computational speed), a custom schedule file was also written for the task in FLIRT's scripting language. Further implementation and download details are available in Supplementary Section 2S.1.

The task of EPI unwarping was accomplished by following the algorithm of Cusack et al. (Cusack et al., 2003). This was implemented and optimized for 2D muscle images by limiting registration to 3 degrees of freedom. The method was otherwise unchanged except for elimination of the skull stripping steps, using a simpler intensity-based masking of the background instead. Briefly, (1) the two phase images were masked and unwrapped; (2) phase images were blurred with a 5 mm Gaussian kernel and images were corrected for overall offsets of 2π introduced during the unwrapping process; (3) a fieldmap was created from the corrected phase images (Haacke et al., 1999); (4) the fieldmap was forward warped to match the EPI images; (5) the EPI images were unwarped using the warped fieldmap; (6) overlay images were generated to check unwarping success. This scheme was implemented using shell scripts written for the task (`fieldmap` and `epiunwarp`). Phase unwrapping was performed by FSL's PRELUDE tool (Smith et al., 2004), and warping was done by FSL's FUGUE tool (Jenkinson et al., 2012).

Comparison matrix

To assess the quality of the `mocorib` tool for performing motion correction despite the inflowing arterial blood, the GRE EPI time series images were also processed with `mcflirt`, a commonly used tool from the FSL package (Oakes et al., 2005; Jenkinson et al., 2002). All processing was done on a single machine (dual-core Intel Core i3 at 1.33 GHz, 4 GB of RAM, running 64-bit Ubuntu Linux 14.04, FSL version 4.1).

Images were processed using two different sets of options for each of `mocorib` and `mcflirt`. The full command line calls are given in Supplementary Section 2S.2. Briefly, `mocorib` was called once with standard options (*mocorib* data set) and once with forced spatial resampling of the images at each registration stage (*mocorib_fs* data set). By default, low resolution (functional) data would only have smoothing applied at each stage. The resampling significantly increased processing time, as shown in Results (Section 2.3). `mcflirt` was called with standard options (*mcflirt* data set), and with sinc interpolation at the final registration optimization stage (*mcflirt_4s* data set). This significantly increases processing time, but may improve accuracy according to the program's documentation (FMRIB Analysis Group, 2015).

Comparison metrics

The first statistical measure used to compare the motion correction tools was root mean squared error (RMSE). RMSE was computed as follows: from the reference image for motion correction, denoted R, and the time series of N GRE EPI images, I, an RMSE image was calculated as the mean of the squared difference at each voxel location, r, using,

$$RMSE(r) = \sqrt{\frac{\sum_{i=1}^{N}(I_i(r) - R(r))^2}{N}} \tag{2.1}$$

RMSE values were reported rather than simple MSE since they were found to give a distribution closer to Gaussian across the image. Global RMSE as a summary statistic was calculated as the mean of the $RMSE(r)$ image for M voxels within an intensity-based mask to remove the background:

$$RMSE_G = \frac{\sum_{r \in mask} RMSE(r)}{M} \tag{2.2}$$

The masking step was found to improve the normality of the distribution of values compared to the full $RMSE(r)$ image including the background.

Definition of H_N

The second statistical measure calculated to assess the effectiveness of the motion correction tools was derived from the motion correction parameters. The statistic, dubbed H_N, is the normalized signal power in the frequency band B, which is centered on a subject's heart rate. H_N was calculated according to the following equation:

$$H_N = \frac{\sum_{i=1}^{3} S_{B,i}}{\sum_{i=1}^{3} S_{N,i}} \tag{2.3}$$

where S_B is the integral of the power spectral density (PSD) in the band B; S_N is the integral of the PSD in an equivalent area adjacent to B; and the subscript $i = 1..3$ indicates that the integrals are calculated for all three motion correction parameters (x- and y-translations and rotation about the z-axis in harmonized units). The calculation was implemented in Python using tools from the NumPy, SciPy, and Matplotlib libraries (Van Der Walt et al., 2011; Hunter, 2007). Further details are provided in Supplementary Section 2S.1. Given the normalization, the expected value of H_N for flat PSDs without a peak in the heart-rate band is 1.0. Figure 2.5 illustrates the technique graphically for a single trial.

Unwarping assessment

To assess the effectiveness of the unwarping, the geometric fidelity of the GRE EPI images to the corresponding T_1-weighted anatomical image for the session was determined. Since the contrast differed between the T_2^* and T_1-weighted images, the correlation ratio (CR) statistic was used instead of RMSE (Roche et al., 1998). For each trial, the *raw* and *unwarped* EPI images were registered to the T_1-weighted image and the correlation ratio was calculated. Two dimensional linear registration was employed for the task.

To examine the source of the EPI distortions, the quality of the shim was also assessed from the B_0 field maps that were generated from the conventional GRE images. The field homogeneity was measured using hand drawn ROIs (circular, 12 mm in diameter) to find the highest and lowest field regions in each slice. The field difference was then calculated, and the mean difference across slices (B_0diff) was calculated for each trial. Finally, a correlation coefficient was calculated from B_0diff and the CR of the *raw* EPI images across trials.

2.3 Results

Vessels, especially arteries, with inflow during the GRE EPI acquisition clearly appear to move during the time series (Figure 2.2). The figure shows the vessel at multiple phases of a cardiac cycle: (i) vessel not apparent; (ii) vessel bright due to inflow; and (iii) vessel shifted due to phase shifts during the slice select gradient. These phases are common throughout the time series, though not apparent in every cardiac cycle since the T_R was not synchronized with the heart rate. The images show that the apparent motion is present even after reducing TOF effects by adding saturation bands above and below the imaged volume.

Table 2.1 reports mean computational time per image frame taken by `mocorib` and `mcflirt` on the standard machine. The *rest* and *post-ex* data sets resulted in almost identical processing rates across conditions for each tool. The fastest processing was achieved in the *mcflirt* data set, which took 4.3 min for the 10 min (2400 frame) *rest* data. The *mocorib* and *mcflirt_4s* data sets both took about 11 min, whereas *mocorib_fs* took 30.4 min for the *rest* data.

Figure 2.3 shows examples of $RMSE(r)$ values from one subject with typical results. For brevity, only the results for the standard options are shown, since the results from the other options are similar. The *raw* data exhibits some increased RMSE values around the edges of the leg due to motion during the time series. The arteries and veins are also highlighted due to flow effects. In the *post-ex* images, several muscles show increased $RMSE(r)$ due to signal variation from physiological effects following exercise. The *mocorib* images have clearly decreased edge effects compared to the *raw* data, indicating successful motion correction. The

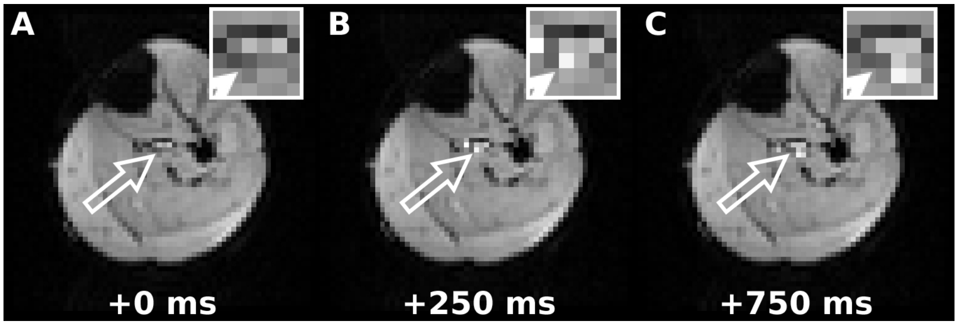

Figure 2.2: Arterial inflow artifact. Three image time frames are shown from the same slice, with the position of the arrow constant in each. Smaller panels are magnifications of the regions near the arrowheads. **(A)** With no inflow, the arteries of the lower leg are not especially apparent. **(B)** In the following image frame (250 ms after *A*), inflowing blood makes the fibular (arrow tip) and posterior tibial (above arrow) arteries appear brighter than surrounding tissue. **(C)** Two frames later (750 ms after *A*), the brightness of the fibular artery appears to have shifted to the lateral posterior (down and right by 3.5 mm in the image). Although this is an image artifact rather than true motion of the vessel (see section 2.1 for explanation), image registration software will treat it as a translation and attempt to remove it with a transformation. The frequency and phase encode directions are left-right and up-down in the image, respectively. On stepping through the time-series, the artifactual motion was observed to be primarily left-right, by as much as two voxels.

mcflirt images, especially the *rest* data, have increased edge effects, indicating that motion has been artificially *introduced* into this time series and data quality has been degraded.

The $RMSE_G$ summary statistic values for each subject are plotted in Figure 2.4. The values for *rest* and *post-ex* have been normalized to the mean value for *raw* data in each case, though the absolute values for the *post-ex* data were greater. For the *rest* condition, both *mocorib* and *mocorib_fs* decreased the $RMSE_G$ value, indicating frame-to-frame motion was reduced. Both *mcflirt* and *mcflirt_4s* increased the $RMSE_G$ value, indicating that data quality was degraded. For the *post-ex* condition, all tools decreased $RMSE_G$, though *mocorib* slightly outperformed *mcflirt*, with most comparisons reaching significance at $p < 0.05$ as indicated in the caption.

Figure 2.5 shows the motion correction parameters and estimated PSDs from *mcflirt* and *mocorib_fs* for one typical *rest* trial. The areas used for calculating H_N are also shown. All parameters in the *mcflirt* PSDs have peaks in the integrated

	mocorib	**mocorib_fs**	**mcflirt**	**mcflirt_4s**
rest	0.284 (0.007)	0.77 (0.05)	0.107 (0.002)	0.28 (0.02)
post-ex	0.268 (0.006)	0.75 (0.04)	0.105 (0.001)	0.27 (0.02)

Table 2.1: Motion Correction Processing Times. Mean (and standard deviation, SD) processing times are expressed in units of seconds per image frame for each software tool. For the 2400 frame *rest* data set, this equated to 11.4 min for `mocorib` and 4.3 min for `mcflirt`.

band which was defined earlier from physiological (heart rate) data. After taking the ratio of the integrated PSDs in the central region to the outer region, this resulted in an H_N value much greater than 1.0 for this trial. The *mocorib_fs* data did not produce a peak in the defined heart rate region, producing an H_N value close to 1.0.

Figure 2.6 shows plotted H_N values for each subject. For both conditions, *mocorib* and *mocorib_fs* produced H_N values that did not significantly differ from 1.0 (one-sample, two-tailed t-test), whereas H_N for *mcflirt* and *mcflirt_4s* significantly differed from 1.0. Both *mcflirt_4s* values and the *rest mcflirt* value were significantly greater than corresponding *mocorib* values (two-tailed, paired t-test, $p < 0.05; p = 0.095$ for *post-ex mcflirt*). This indicated contamination of the motion correction parameters from physiological noise in cases where `mcflirt` was used. It was also notable that H_N values generally increased for *post-ex* data compared to *rest*, as there was greater arterial flow during acquisition of *post-ex* data.

Figure 2.7 shows the results of unwarping the GRE EPI images of a single slice in a typical subject using the `epiunwarp` script, after generating B_0 field maps using the `fieldmap` script. Fidelity of the EPI images to the anatomical images was notably improved in the areas of the lateral gastrocnemius and anterior compartment. When examining the distortion from a difference image of the *raw* and *unwarped* images, the shift was measured to be a maximum of 7.5 mm, representing approximately 3 pixels in-plane. The correlation ratio of the *raw* and *unwarped* images to the anatomical were 0.824 and 0.875 in this trial, respectively.

The group mean correlation ratio values for *rest* and *post-ex* conditions are shown in Table 2.2. The mean CR increased with unwarping in both cases, but was statistically significant only for the *post-ex* data. The B_0diff values were not

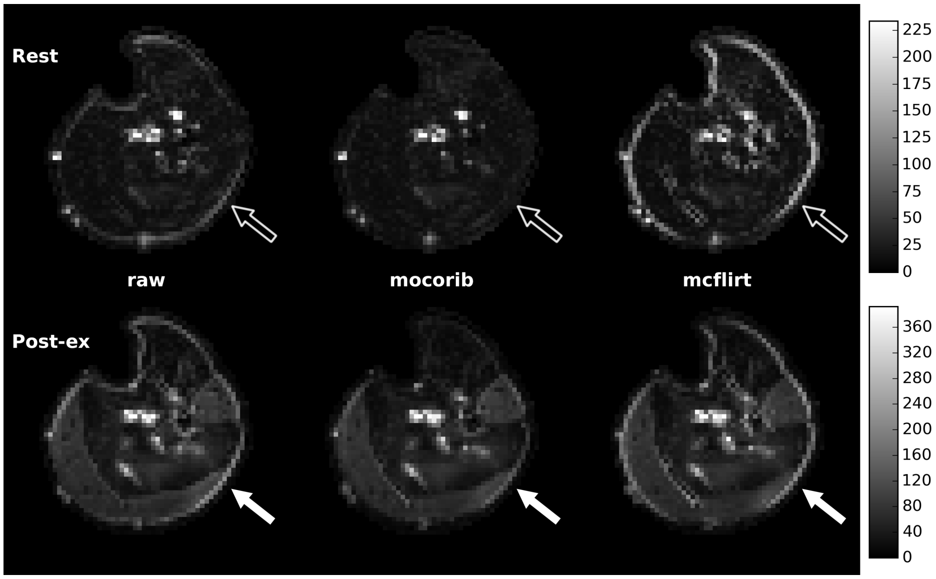

Figure 2.3: ***RMSE*(*r*) images**. Each image represents a single slice of *RMSE*(*r*) values from a typical subject. The **top** row is from *rest* data. Note the decrease in *RMSE*(*r*) around the edges in the *mocorib* data with arteries masked, whereas the edge effects increase in the *mcflirt* data (open arrows). The **bottom** row is from *post-ex* data. The edge effects are greatly reduced in the *mocorib* data compared to *raw*, whereas the *mcflirt* image shows less improvement over *raw* (solid arrows). Note the higher scale in *post-ex RMSE*(*r*) values (380 versus 230 in *rest*) due to higher motion and greater physiological noise in *post-ex* data. Also note the increased intensity in the gastrocnemius and lateral compartment due to post-exercise physiological changes.

significantly different between *rest* and *post-ex* conditions; the range was 0.5 – 3.5 ppm, with mean (and standard deviation, SD) of 2.0 (1.1) ppm across all trials. B_0diff and *raw* CR values were anti-correlated, with $r = -0.76$ in *rest* data, $r = -0.66$ in *post-ex*, and $r = -0.71$ across all trials.

2.4 Discussion

Through-plane arterial blood flow was shown to cause vessel motion artifacts despite the use of spatial saturation bands during image acquisition to attenuate the flow signal. The limited effectiveness of the saturation bands is understandable given the severity of the TOF effect: the TOF saturation threshold was $z/T_R = 4$ cm/s in this study, while peak flow in lower leg arteries is approximately

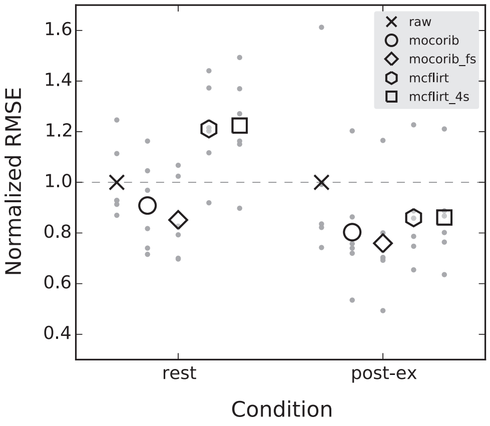

Figure 2.4: *$RMSE_G$* plot. Large symbols indicate group mean $RMSE_G$ values from tested software tools, whereas small symbols are subject data points. Values were normalized by the mean *raw* $RMSE_G$ for each condition to ease comparison. For the *rest* data, mean $RMSE_G$ decreased significantly for *mocorib* data compared to *raw* (paired, two-tailed t-test $p < 0.05$), whereas *mcflirt* data had significantly increased $RMSE_G$ ($p < 0.05$). This indicated that `mcflirt` added motion rather than reducing it. For *post-ex* data, both tools decreased $RMSE_G$ on average, though only the *mocorib* values were statistically significant ($p < 0.05$, $p = 0.07, 0.08$ for *mcflirt* and *mcflirt_4s*, respectively).

20 cm/s (Caputo and Higgins, 1992). The pulsatile nature of the vessel motion artifact was shown, by examining H_N, to influence the motion correction parameters produced by a conventional motion correction program. Further, the $RMSE(r)$ images and global $RMSE_G$ values indicated that the conventional motion correction tool actually degraded the time series image quality in some trials. It should be noted that `mcflirt` was not designed with pulsatile flow in mind; the validation testing by the program's authors was done with simulated data generated using affine transforms, but not including flow effects (Jenkinson et al., 2002). Indeed, it would be difficult to predict that the arteries, which represent a small proportion of the leg cross section, could have such influence over the motion correction parameters. It's likely because the arteries have such high signal compared to the surrounding tissue, generating high contrast, that they have such an effect.

Compared to the conventional tool, the custom written `mocorib` script was shown to give excellent motion correction results, with the difference especially apparent in resting data. Masking the arteries from the motion correction cost function effectively reduced the influence of the pulsatile signal in most subjects.

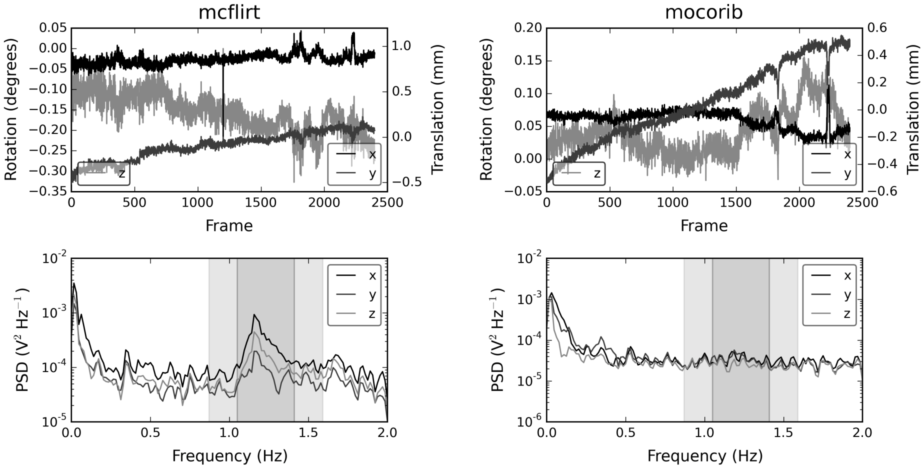

Figure 2.5: Motion correction parameters and PSDs. The motion correction parameters (top) from one *rest* trial of a subject and their associated power spectral densities (bottom) as determined by FSL's `mcflirt` (left) and the custom written `mocorib`, with the `forcescale` option (right). The x and y lines represent translations, and the z lines represent rotations about the z-axis. The dark vertical band in the PSD plots represents the frequency band B integrated to determine S_B in this trial. The adjacent lighter bands represent the area integrated for the normalizing the score to determine H_N (see section 2.2). The H_N values were 2.8 and 1.2 for `mcflirt` and `mocorib` in this trial, respectively.

In some subjects, pulsatile influence in the motion correction parameters was still evident, especially in the *post-ex* data, as shown in Figure 2.6. This was likely due to the fact that only major arteries were masked, not minor vessels, so a relatively small pulsatile effect remained.

The `mocorib` script was found to take significantly longer than `mcflirt` with standard settings. This was likely because of the nature of the file operations of the two tools: `mcflirt` operates mainly in RAM, whereas `mocorib` relies on file system input/output operations at many stages of the procedure to write intermediate results. Attempts to mitigate the computational time discrepancy included writing the intermediate images to a RAM disk and using parallel processing when possible. In the future, re-writing the tool in C or incorporating its functionality into the open source `mcflirt` code would likely decrease processing time.

`Mocorib` and the associated FLIRT script were tested with various options to optimize for motion correction, with the particular goal of parameter *stability* rather than the absolute lowest cost function value. The goal was to correct motion and

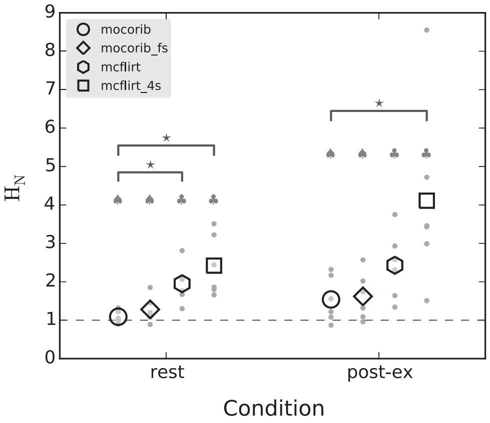

Figure 2.6: H_N values. Mean H_N values are shown for *rest* and *post-ex* conditions as large symbols, with small circles showing individual data points. (♠) No values from *mocorib* were significantly different from 1.0 (paired, two-tailed t-test, $p > 0.05$, $p = 0.24, 0.10, 0.08, 0.06$ left to right in the figure), whereas (♣) all *mcflirt* values significantly differed from 1.0 ($p < 0.05$). (★) Three of the four *mcflirt* values were significantly greater than corresponding *mocorib* values ($p < 0.05$, $p = 0.095$ for *post-ex mcflirt*).

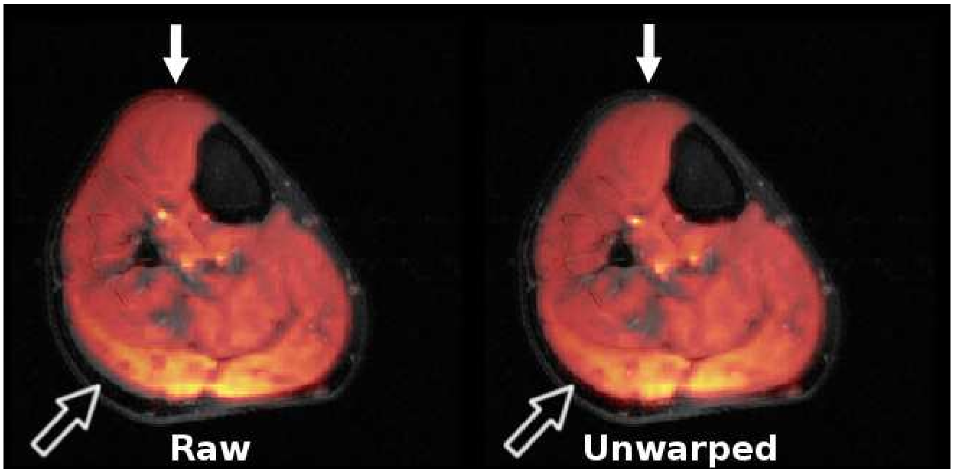

Figure 2.7: EPI unwarping. A single slice of GRE EPI data (red-yellow colormap) overlayed on the subject's anatomical image (grey colormap). The non-rigid distortion of the EPI images in the phase encode direction (vertical in this image) due to B_0 field variations caused poor registration. The effect is apparent near the lateral gastrocnemius (*open arrow*) and the anterior compartment (*solid arrow*).

	raw CR	**unwarped CR**	**B_0diff [ppm]**	**pearson r**
rest	0.86 (0.07)	0.88 (0.07)	1.8 (1.0)	-0.76
post-ex	0.84 (0.06)	0.86 (0.05)	2.2 (1.2)	-0.66

Table 2.2: EPI Distortion Measures. Group mean (and SD) correlation ratio (CR) values for the *rest* and *post-ex* conditions are shown. The statistic was calculated from *raw* and *unwarped* EPI images that were linearly registered to corresponding T_1 anatomical images. The difference between *unwarped* and *raw* images was statistically significant only for *post-ex* data (paired, two-tailed t-test, $p < 0.05$, $p = 0.09$ for *rest* data). Mean (and SD) B_0 field variations (B_0diff) are also shown, in units of ppm. Pearson's r refers to the correlation coefficient calculated from B_0diff and *raw* CR values across trials.

not introduce new motion, which may occur when the optimizer is alternating from frame-to-frame between two nearly identical solutions to the registration problem. A key strategy to accomplish this goal was to initialize each frame's registration with the registration parameters of the previous frame. Mutual information was also found to have more variance in its frame-to-frame motion correction parameters compared to normalized correlation.

Performing EPI distortion correction with the `epiunwarp` script was found to increase fidelity to the anatomical images across trials, as shown by the CR values. The increase in CR varied widely across trials, with some trials having a negligible difference of 0.1% and others having differences up to 8.0%. The amount of EPI distortion was found to be strongly associated with a low quality shim; the correlation coefficient of $r = -0.71$ between the *raw* CR and B_0diff values indicates that EPI fidelity decreases with increasing B_0 field variation. Though the geometric fidelity of trials with low *raw* CR and high B_0diff improved more than trials with high *raw* CR, the CR values typically did not improve to match those of trials with very low B_0diff. This indicates that better quality images are obtained from having a very good shim during acquisition, rather than attempting to improve the results with field maps in post-processing.

This study has identified a motion correction problem not previously described in the literature. The influence of the arterial inflow artifact was reduced by the strategy of masking the cost function in the `mocorib` script. The well known problem of EPI distortion was also mitigated by the `epiunwarp` script. These tools, which are available for download, should prove useful for muscle functional imaging researchers in future studies.

Acknowledgements

Funding for this project was provided by a Natural Sciences and Engineering Research Council (NSERC) Discovery Grant to Dr. M. Noseworthy, titled: Advanced Analysis of Functional Magnetic Resonance Imaging (MRI) Data for Evaluation of Tissue Physiology. The authors also wish to acknowledge the indispensable help of Conrad Rockel during data acquisition.

References

Buxton, R. B. 2009. *Introduction to Functional Magnetic Resonance Imaging: Principles and Techniques.* 2nd edition. Cambridge, UK: Cambridge University Press.

Caputo, G. R. and C. B. Higgins. 1992. “Magnetic resonance angiography and measurement of blood flow in the peripheral vessels.” *Invest Radiol* 27 Suppl 2: S97–102.

Carlier, P. G., D. Bertoldi, C. Baligand, C. Wary, and Y. Fromes. 2006. “Muscle blood flow and oxygenation measured by NMR imaging and spectroscopy.” *NMR Biomed* 19: 954–967.

Cox, R. W. 1996. “AFNI: software for analysis and visualization of functional magnetic resonance neuroimages.” *Comput Biomed Res* 29: 162–173.

Cusack, R., M. Brett, and K. Osswald. 2003. “An Evaluation of the Use of Magnetic Field Maps to Undistort Echo-Planar Images.” *Neuroimage* 18: 127–142.

FMRIB Analysis Group. 2015. “MCFLIRT – FslWiki.” `http://fsl.fmrib.ox.ac.uk/fsl/fslwiki/MCFLIRT`. Accessed: 2017-08-13.

Froeling, M., A. J. Nederveen, D. F. Heijtel, A. Lataster, C. Bos, K. Nicolay, M. Maas, M. R. Drost, and G. J. Strijkers. 2012. “Diffusion-tensor MRI reveals the complex muscle architecture of the human forearm.” *Journal of Magnetic Resonance Imaging* 36: 237–248.

Haacke, E. M., R. W. Brown, M. R. Thompson, and R. Venkatesan. 1999. *Magnetic Resonance Imaging: Physical Principles and Sequence Design.* New York: John Wiley & Sons.

Hunter, J. D. 2007. “Matplotlib: A 2D graphics environment.” *Comput Sci Eng* 9: 90–95.

Jenkinson, M., P. Bannister, M. Brady, and S. Smith. 2002. “Improved optimization for the robust and accurate linear registration and motion correction of brain images.” *NeuroImage* 17: 825–841.

Jenkinson, M., C. F. Beckmann, T. E. J. Behrens, M. W. Woolrich, and S. M. Smith. 2012. “FSL.” *Neuroimage* 62: 782–790.

Jenkinson, M. and S. Smith. 2001. “A global optimisation method for robust affine registration of brain images.” *Med Image Anal* 5: 143–156.

Jezzard, P. and R. S. Balaban. 1995. “Correction for geometric distortion in echo planar images from B0 field variations.” *Magn Reson Med* 34: 65–73.

Ljunggren, S. 1983. “A simple graphical representation of Fourier-based imaging methods.” *J Magn Reson* 54: 338–343.

McRobbie, D. W., E. A. Moore, M. J. Graves, and M. R. Prince. 2007. *MRI from Picture to Proton.* 2 edition. Cambridge University Press.

Noseworthy, M. D., A. D. Davis, and A. H. Elzibak. 2010. “Advanced MR imaging techniques for skeletal muscle evaluation.” *Semin Musculoskelet Radiol* 14: 257–268.

Oakes, T. R., T. Johnstone, K. S. Ores Walsh, L. L. Greischar, A. L. Alexander, A. S. Fox, and R. J. Davidson. 2005. “Comparison of fMRI motion correction software tools.” *NeuroImage* 28: 529–543.

Roche, A., G. Malandain, X. Pennec, and N. Ayache. 1998. “The correlation ratio as a new similarity measure for multimodal image registration.” In “Medical Image Computing and Computer-Assisted Interventation — MICCAI’98,” pp. 1115–1124. Springer.

Smith, S. M., M. Jenkinson, M. W. Woolrich, C. F. Beckmann, T. E. J. Behrens, H. Johansen-Berg, P. R. Bannister, M. De Luca, I. Drobnjak, D. E. Flitney, R. K. Niazy, J. Saunders, J. Vickers, Y. Zhang, N. De Stefano, J. M. Brady, and P. M. Matthews. 2004. “Advances in functional and structural MR image analysis and implementation as FSL.” *NeuroImage* 23 Suppl 1: S208–19.

Van Der Walt, S., S. C. Colbert, and G. Varoquaux. 2011. “The NumPy array: a structure for efficient numerical computation.” *Computing in Science & Engineering* 13: 22–30.

2S Supplementary material

2S.1 Implementation Details

As discussed in section 2.2, the `mocorib` program was written to implement the motion correction scheme. The script operates by splitting an input 4D time series into 3D volumes, estimating motion correction parameters, and applying them to the original images. Other features of the script and the associated FLIRT schedule file include: (1) passing of output registration parameters from one frame to initialize the registration of the next frame, for speed and consistency; (2) choices of degrees of freedom for registration in 2D or 3D; (3) flexible options to tune the registration parameters based on those available in FLIRT; (4) option to write parameters out before full registration of a frame is complete to allow parallel processing and speed the result. Sensible default values for script parameters such as cost function were specified after some initial testing, while still allowing flexibility.

The `mocorib`, `fieldmap`, and `epiunwarp` shell scripts, the FLIRT schedule file, and the documentation are available for download from the following page: `goo.gl/VcDW6S`.

The equation for the statistic H_N was discussed in section 2.2. H_N was calculated as follows: first, the centre frequency and peak width of the subject's heart-rate were manually delineated from the PSD of a physiological signal acquired during the scan. This determined the heart-rate band, B. Next, the rotation and translation values from the motion correction parameters were harmonized by calculating the arc length ($s = r\theta$) of a rotating voxel at a radius of $1/2$ the FOV. PSDs were estimated using Welch's method for the three motion correction parameters (x- and y-translations and the converted rotation about the z-axis). S_B was calculated as the sum of the integrals of the three PSDs in the heart-rate frequency band defined earlier. Finally, H_N was calculated as the ratio of S_B to the sum of the integrals of the PSDs in an equivalent area band adjacent to (i.e. split on either side of) B.

2S.2 Command Line Program Calls

As discussed in section 2.2, the `mocorib` and `mcflirt` programs were each used to perform motion correction on the data in two ways. Assuming an input data set of functional images called `EPI.nii` and an arterial mask image called `mask.nii`, the actual command lines used are listed below. Full details related to the arguments may be found in the documentation for `mocorib`, available from the above download `link`.

mocorib

```
mocorib -refweight=mask.nii -ibw -2D -dof=3 -jobctrl
-interp=sinc -cost=normcorr -tolrot=0.001 -toltrn=0.05
-nopars -outp=EPI-mocorib EPI.nii
```

mocorib_fs

```
mocorib -refweight=mask.nii.gz -ibw -2D -dof=3 -jobctrl
-interp=sinc -cost=normcorr -tolrot=0.001 -toltrn=0.05
-nopars -forcescale -outp=EPI-mocorib_fs EPI.nii
```

mcflirt

```
mcflirt -in EPI.nii -2d -mats -sinc_final -out EPI-mcf
```

mcflirt_4s

```
mcflirt -in EPI.nii -2d -mats -sinc_final -stages 4 -out EPI-mcf_4s
```

Chapter 3

Post-contraction spin saturation effect: model for regression and displacement mapping in gradient echo images of skeletal muscle

Preface

The following chapter has been submitted for publication. The analysis in this chapter builds on the preprocessed data from the previous chapter and examines a small segment of the data immediately following exercise. This data includes an artifact that results from the exercise motion that precedes its acquisition. This portion of the data could simply be excluded, but if a BOLD analysis of the time period is desired, the motion-related artifact must be regressed out. This chapter includes an argument about the origin of the artifact as a T_1 regrowth effect, which leads to a model of the signal effect as a mono-exponential decay. This chapter also shows how the artifact can be exploited to examine the nature of the motion that caused it.

Abstract

Object. The objective of this study was to characterize an artifact common in time series gradient echo (GRE) echo planar imaging (EPI) magnetic resonance imaging (MRI) data. A model for regression of the artifact was described, as well as a method to generate muscle displacement maps using the artifact.

Materials and Methods. Subjects performed isotonic plantar flexion exercise inside a 3 T MRI scanner while a time series of axial GRE EPI images of the lower leg was acquired. An image post-processing scheme was developed to exploit the saturation effect evident in the signal upon muscle return to baseline position after a contraction, when muscle tissue leaves and re-enters the imaged volume. For validation of the motion-mapping technique, an agar phantom was placed in the MRI scanner and displaced a known distance during a GRE EPI scan. B-mode ultrasound imaging was also employed to validate in-vivo results.

Results. Through-plane displacement maps were generated from subject and phantom data. Motion maps from the phantom were in agreement with the true displacement. Over the cross-section of the lower leg, the algorithm indicated 44 ± 12% of voxels had undergone motion. In particular, superior motion was especially prominent near the deep aponeuroses of the triceps surae (DA), with 80% of voxels within 2.5 mm of the DA mapped superiorly. Inferior motion was mapped further from the DA, peaking at a distance of 10 mm in the triceps surae, and in the anterior compartment. Ultrasound imaging confirmed the in-vivo displacement directionality and magnitude.

Conclusion. The new method mapped muscle displacement in a pattern consistent with expectations for plantar flexion. This method provides researchers who already perform functional GRE EPI muscle studies with valuable complementary information, without significant adjustment of scan parameters.

3.1 Introduction

The action of skeletal muscle and tendon complexes to move and stabilize joints is a broad topic; it encompasses physical scales ranging from whole limbs to subcellular proteins, with diverse fields of study. On the scale of bulk muscle function, the foundational biomechanical measure is tissue strain (Monti et al., 1999). This may be ascertained by mapping skeletal muscle motion during voluntary exercise (Oomens et al., 2009). Tissue strain can further the understanding of how forces are transmitted along muscles and tendons considering the varying cross sectional areas of components such as tapering fascicles. Strain measurements can also show how forces in muscles and tendons change with muscle plasticity, such as during hypertrophy and aging (Trotter, 2002).

Previous studies have examined muscle motion with ultrasound (Fukunaga et al., 1997) and specialized magnetic resonance imaging (MRI) sequences such as phase-contrast (Drace and Pelc, 1994). Sinha et al. have published several such MRI studies using cine phase-contrast and spin-tag sequences during plantar flexion (PF) of the lower leg (Sinha et al., 2004; Finni et al., 2003, 2006; Kinugasa et al., 2008). PF exercise is primarily, but not entirely, performed by the triceps surae muscle group (Murray et al., 1976; Finni et al., 2006)), which is composed of the soleus muscle and the medial and lateral heads of the gastrocnemius muscle. The spin-tag images revealed how complex muscle motion is during flexion, especially the shear of muscles across one another in the transverse plane. These studies also showed the spatial heterogeneity of motion along the longitudinal axis within muscles during exercise (Finni et al., 2003, 2006). In addition, the importance of the deep and superficial aponeuroses of the triceps surae to bulk muscle motion during this type of exercise was revealed (Kinugasa et al., 2008).

Other imaging studies of skeletal muscle commonly probe physiological measures such as blood volume and oxygenation using time series gradient echo (GRE) echo planar imaging (EPI). Studies commonly use a long T_E to examine the blood oxygenation level dependent (BOLD) effect, though exceptions exist (e.g. Damon et al., 2007). GRE EPI shows increasing promise in evaluating skeletal muscle under a variety of conditions, especially during exercise (Carlier et al., 2006; Noseworthy et al., 2010). Thus far, such studies have not considered whether time series GRE images may be used to evaluate biomechanics through muscle motion mapping.

The steady state signal magnitude of a spoiled GRE sequence is well known (Bernstein, 2004). The equilibrium condition holds for the perfect case of static tissue undergoing a chain of radio frequency pulses. If the spins undergo bulk motion that causes them to move out of the imaged volume during scanning, as in an exercise protocol, they will undergo partial relaxation with time constant T_1; when they return to and remain in the imaged volume, the signal will asymptotically approach steady state with time constant τ:

$$\tau = -T_R / \ln(\cos\alpha\, e^{-T_R/T_1}) \tag{3.1}$$

A full description of how the signal approaches steady state is provided in Section 3A.1.

The previously discussed spin-tag and phase-contrast methods of examining muscle motion during exercise give reliable and specific quantitative data. However, they require scans during exercise that acquire only motion data, and require specialized hardware to trigger the scanning during contraction while subjects synchronize exercise with an external cue (Sinha et al., 2004). Since subjects must execute dozens of roughly identical contractions in succession, the maximum contraction intensity subjects can tolerate is limited to a fraction of their strength, and requires a suitable rest period before repeating the experiment to acquire functional data, if such data are desired.

In this study we present a novel method for generating maps of muscle motion during exercise directly from time series GRE EPI data. The method exploits a phenomenon of highly elevated signal intensity in time series data immediately after a muscle contraction. GRE EPI data for muscle studies are typically acquired over several minutes, but the signal elevation phenomenon occurs very briefly. The phenomenon is caused by the magnetization relaxation and re-saturation when muscle tissue moves out of and into the imaged volume during contraction cycles. It has been a noted artifact in previous muscle studies (Meyer et al., 2004; Wigmore et al., 2004; Towse et al., 2005). Our method does not require subjects to exercise in synchrony, or with a trigger mechanism. An arbitrary exercise paradigm is also possible, in terms of timing and intensity. This technique allows researchers already performing GRE EPI muscle studies to gain displacement measures from the data as well.

3.2 Materials and Methods

Subjects and exercise

Six healthy male volunteers participated (mean age 31 ± 9), with informed consent and approval from our local institutional review board. PF exercise was performed

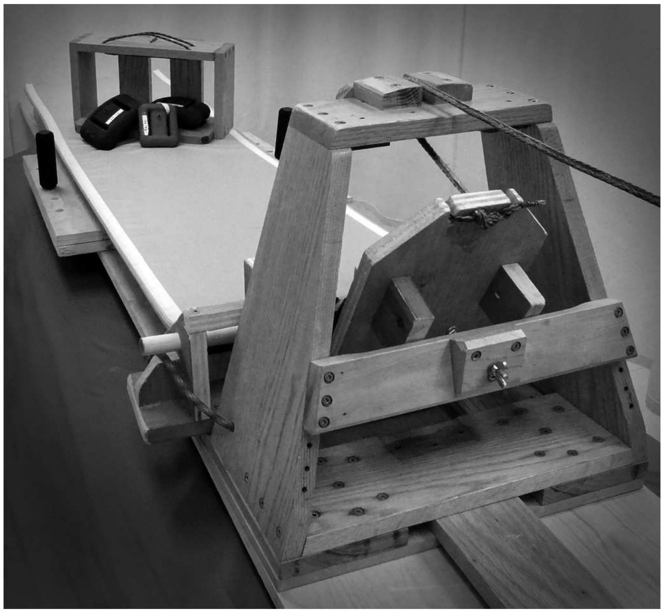

Figure 3.1: **Ergometer**. The main housing of the ergometer (oak wood frame) is shown removed from the magnet. The base of the unit, which attaches to the scanner bed, is visible beyond the housing. Subjects lay on the bed and were strapped into the foot pedal. The cord visible in the foreground is made from low-stretch Kevlar. It ran over plastic pulleys, and was attached to a hanging load of variable mass when installed. An example load using lead diving weights is pictured on the bed in the background.

using a custom built MRI compatible ergometer employing a pulley system with hanging weights for variable resistance (Fig. 3.1). Subjects were positioned feet-first supine with their right foot attached to the ergometer pedal with Velcro straps. The ankle angle began at 99°, with PF taking it to 113°, and the knee was almost completely extended. The bed surface was built up with cushions under the torso and thigh to allow the calf muscle to hang without compression. Restraining straps were tightly fastened around the right thigh just above the knee and on the hips to prevent upper leg movement. The subjects also held handles to keep themselves in place, and a separate system kept the scanner bed from inadvertently moving during exercise.

At least one day before the study a one repetition maximum (1RM) test was performed on each subject with the ergometer in the magnet. Vocal encouragement was given during the test to ensure maximal subject performance. Subsequently the MRI exercise protocol was 2.5 min of dynamic (0.5 Hz) PF at 50% of a subject's

1RM.

Image acquisition

Image data were collected using a 3 T GE HD Signa MR scanner with a single channel, receive-only, GPFLEX coil (General Electric Healthcare, Milwaukee, WI). Scan sessions began with localization, second order shimming, and T_1-weighted structural imaging of three 10 mm thick, axial slices (0 mm gap) with chemical fat saturation (FATSAT) (acquisition matrix size (MS) = 256×256, field of view (FOV) = 16 cm, $T_E = 4.9$ ms, $T_R = 51$ ms, $\alpha = 19°$, receive bandwidth (rBW) = 62.5 kHz). FATSAT was used to aid registration with GRE EPI images and delineate muscle compartments for ease of segmentation. Slices were located at the largest cross section of the calf muscles in the right leg, as determined from the localizer image. Next, a GRE EPI (single-shot, Cartesian) time series was acquired from 3 axial slices with the same FOV, thickness and locations as the T_1-weighted structural scan (MS = 64×64, $T_E = 35$ ms, $T_R = 250$ ms, $\alpha = 33°$, rBW = 500 kHz) (Ljunggren, 1983). The 33° flip angle was used since it represents the Ernst angle for muscle at $T_R = 250$ ms (Ernst and Anderson, 1966). The long T_E was used to match typical BOLD imaging studies. Spatial saturation bands (40 mm thick) were prescribed immediately proximal and distal to the imaged volume to reduce flow-related artifacts. Along with each EPI series, two fast spoiled gradient echo (FSPGR) images were acquired to generate B_0 field maps ($T_E = 4.55/6.82$ ms for $\Delta T_E = 2.27$ ms; MS = 128×128; rBW = 62.5 kHz), with FOV, T_R, and α all exactly matched to the EPI images (Haacke et al., 1999). EPI images were acquired before, during, and after exercise, as follows (see also Fig. 3.2): (1) 10 min of baseline data were acquired before the start of exercise (*rest* data set); (2) exercise was started without the scanner running; (3) data acquisition was started with 30 s remaining in the exercise, and continued after exercise for 12.5 min. This image time series was examined and exercise frames were removed to leave only the data following exercise (*post-ex* data set). Following a 40 min break, during which the subjects were allowed to exit the magnet and relax, the entire protocol was repeated to assess measurement consistency. The long EPI time series data was acquired for a different study of muscle exercise and recovery. However, for this study only a small fraction of the data immediately following exercise was used (115 data points, equivalent to

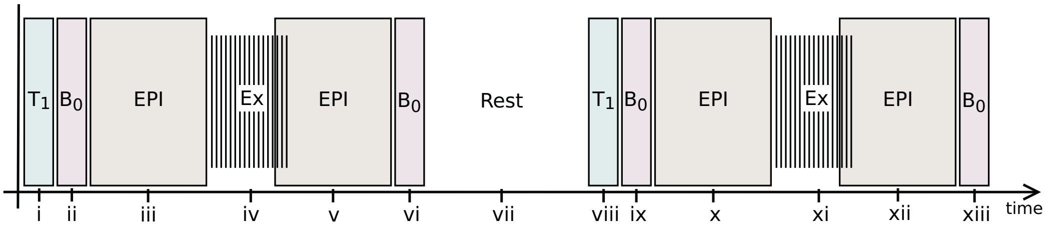

Figure 3.2: Experiment timeline. The diagram shows the order of events during the MRI experiment (not to scale). **(i,viii)** Subject attached to ergometer inside MRI scanner; localizer and T_1-weighted structural images acquired; **(ii,vi,ix,xiii)** two FSPGR images acquired for B_0 field map creation; **(iii,x)** 10 min EPI time series acquired before exercise; **(iv,xi)** plantar flexion exercise performed; **(v,xii)** 13 min EPI time series started with 30 s of exercise remaining; exercise frames were later discarded, leaving 12.5 min image time series; **(vii)** 40 min rest period with subjects outside the scanner.

28.75 s) with the goal of exploring motion and the spin saturation effect.

Phantom Experiment

The phantom consisted of two litres of 5% agar mixture in a plastic container. Axial GRE EPI images were acquired with identical parameters to those in the subjects, except that six 5 mm slices were acquired, which necessitated an increase to $T_R = 350$ ms. The phantom was moved during imaging using a long wooden handle. The motion occurred along the magnet axis (proximal direction for the lower leg of a subject in FFS position), followed by a 20 s pause and a return to the starting position. The duration of the movement out of and into the starting position was approximately 1 s each way, and the distance was 2.0 cm, with an estimated uncertainty of 2 mm.

Ultrasound examination

To validate motion measures from the exercise protocol, ultrasound imaging (B-mode) with video capture was performed on a subject with the ergometer outside the magnet, using an Ultrasonix system and a 12.5 MHz ultrasonic linear array transducer (Sonix USA Analogic Ultrasound, Scottsdale AZ). Images were acquired in a sagittal oblique plane in the medial gastrocnemius and tibialis anterior muscles while the subject performed the exercise routine described above. A flexion event was chosen from the image series for its high quality depiction of striation motion at the crossing of the aponeurosis, and muscle displacement was measured (Fukunaga et al., 1997).

Image preprocessing

GRE EPI image preprocessing was accomplished using custom written Bourne-again shell (BASH) shell scripts making use of FSL and AFNI tools (`fsl.fmrib.ox.ac.uk/fsl/fslwiki`, `afni.nimh.nih.gov/afni`) (Jenkinson et al., 2012; Cox, 1996). Steps included motion correction and geometric distortion correction (unwarping) based on B_0 field maps to allow accurate registration between functional and structural images (Davis and Noseworthy, 2016). Smoothing with a 5 mm full width at half maximum (FWHM) Gaussian kernel was also employed, but applied only in-plane to prevent a reduction in precision of through-plane motion measurements.

Regions of interest (ROIs) that excluded major vessels were manually drawn on the structural images for 7 muscle groups in the lower leg (Fig. 3.3). A 2.5 mm wide line (i.e. the size of one functional image voxel) was also drawn to represent the deep aponeuroses of the triceps surae (DA), along the border of the gastrocnemius and soleus muscles and the central sulcus of the posterior aponeurosis of the soleus (Hodgson et al., 2006). ROIs were transformed into functional image space using linear registration (Jenkinson and Smith, 2001).

Image analysis

Each *post-ex* EPI time series was analyzed and motion maps were generated using a custom written MATLAB program (R2012a, The MathWorks Inc., Natick, MA). The full analysis algorithm is described in Section 3A.2. Briefly, the first 15 post-exercise data points of a voxel's signal were fit with a mono-exponential decay curve (Eq. (3.6) in Section 3A.1) after removing the longer-term linear trend in *post-ex* data. Motion was indicated in a voxel if the fits met certain criteria: (i) the values of the initial signal decay magnitude and time constant, taking into account their standard errors, must be within predefined limits to obtain a curve with the expected shape; (ii) the R^2 statistic for the curve fit to the data must be greater than 0.60 (Boslaugh and Watters, 2008). Voxels meeting the criteria were included in motion maps and overlaid on the subject's structural image. Given

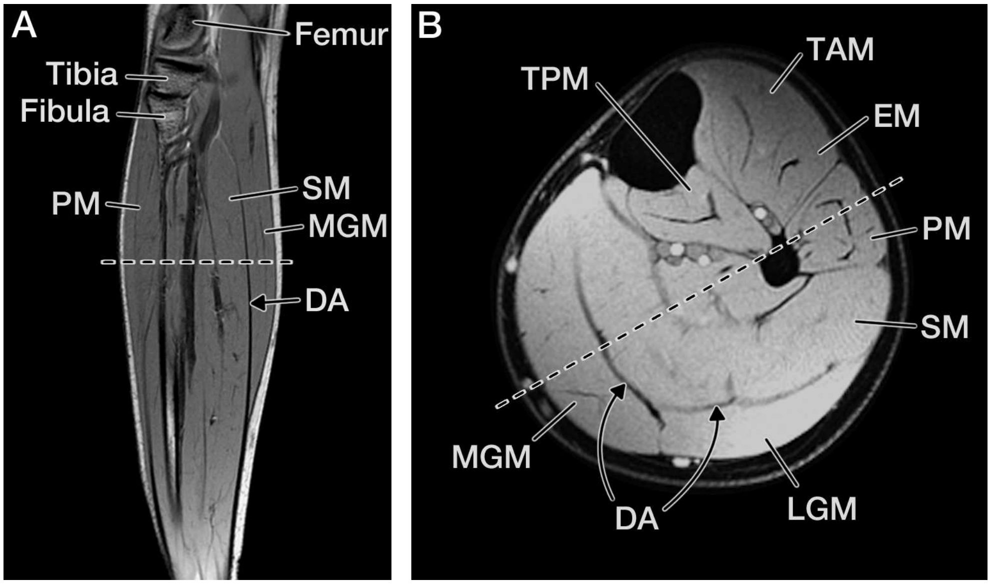

Figure 3.3: Regions of interest. ROIs in the lower leg are shown: *(MGM)* and *(LGM)* medial and lateral head of the gastrocnemius muscle, respectively; *(SM)* posterior soleus muscle; *(PM)* peroneus longus and brevis muscles; *(EM)* extensor digitorum and hallucis longus muscles; *(TAM)* tibialis anterior muscle; *(TPM)* tibialis posterior muscle; *(DA)* deep aponeuroses of the triceps surae. The dashed line in the sagittal oblique view **(A)** indicates the approximate slice location for **(B)**, and the images acquired in this study. The dashed line in the axial view **(B)** indicates the approximate sagittal oblique slice location of **(A)**.

the complexity of the in-vivo muscle motion maps, with potentially overlapping regions, the maps were split into inferior and superior parts for display.

Group results were expressed as the fraction of motion voxels by total ROI voxels for each muscle group. Normality was tested (using MATLAB's Jarque-Bera test, `jbtest`, which combines both 3rd and 4th moments about the mean), and then a paired Student's T-test was used for each muscle group to attempt to distinguish the two runs. Finally, plots were generated using the `Matplotlib` python package (Hunter, 2007).

3.3 Results

Ultrasound images were used to validate muscle motion measures (Fig. 3.4). Near the deep aponeurosis of the gastrocnemius, the medial gastrocnemius muscle

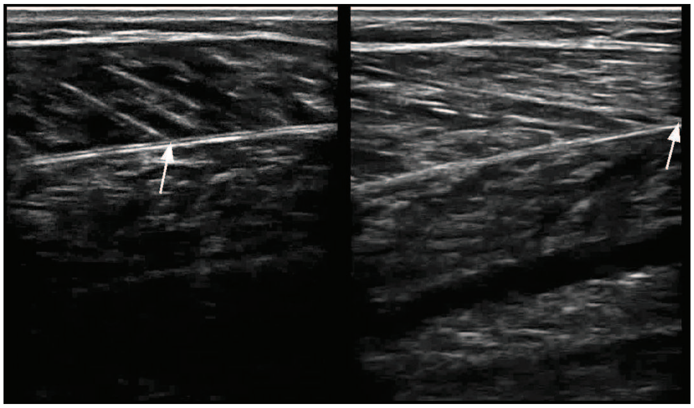

Figure 3.4: Ultrasound validation. The images show a sagittal oblique plane of the lower leg, superior toward the right, with the MGM towards the top of the image and SM visible underneath it. Arrows indicate the location of the same striation at the intersection point with the DA, with the subject in relaxed (**left**) and flexed (**right**) conditions.

(MGM) was found to move 18 ± 1 mm superiorly, while it moved 4 ± 1 mm inferiorly near the superficial aponeurosis. In the tibialis anterior muscle (TAM), displacement measures ranged from 8 ± 1 mm inferiorly near the aponeurosis in the muscle belly to 5 ± 1 mm inferiorly close to the tibia. Motion of the tibia itself appeared low (less than 2 mm on the longitudinal axis), though it was difficult to assess due to low signal beyond the tissue-bone interface.

In order to illustrate the *post-ex* fitting procedure, sample data along with the linear detrending and mono-exponential fits are shown in Figure 3.5. Intermediate results of the fitting method for the phantom data, in the form of slice-by-slice R^2 maps, are presented in Figure 3.6. The most inferior slice is devoid of motion-indicated voxels, which is consistent with the displacement of the phantom being in the superior direction. In the four most superior slices, representing a 20 mm thick slab, the fitting algorithm flagged every ROI voxel as having moved out of the imaged volume (with uniformly high R^2). Some of the ROI voxels in the next slice were also flagged (with mixed R^2).

The six slices of phantom results were combined to form a motion map (Fig. 3.7), using the slice thickness of 5 mm. The map indicated variable motion across the slice of either 20 or 25 mm. This was consistent with the actual motion of the phantom: 20 mm, with a small uncertainty.

Fits of in-vivo *post-ex* data were performed on a mean of 1800 ROI voxels across

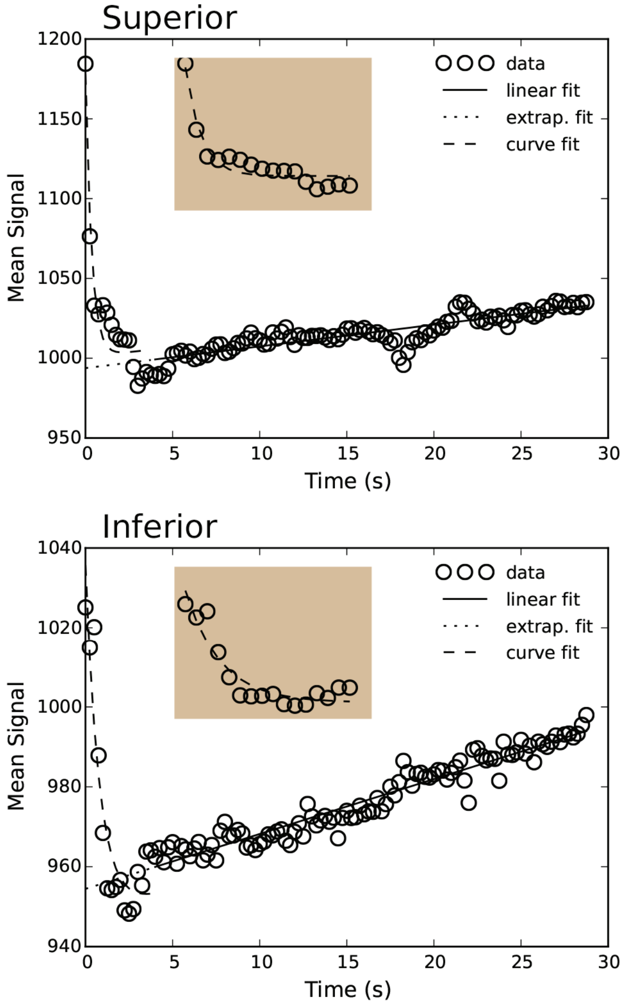

Figure 3.5: Saturation signal fit method. Fits are shown to post-exercise data from the mean of the MGM motion map voxels from one trial in the superior (**upper plot**, 84 voxels averaged) and inferior (**lower plot**, 62 voxels averaged) directions. Shown are the linear fit (solid line), extrapolation to early points (dotted line), and subsequent exponential decay curve fit (dashed line). Insets show fits of early post-exercise data to a mono-exponential curve after removal of the linear trend.

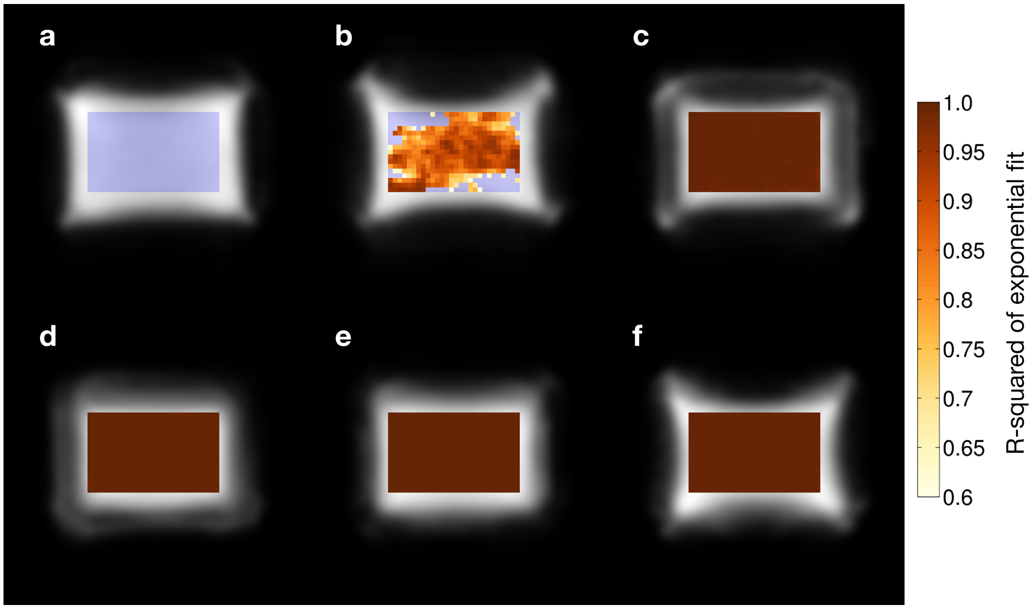

Figure 3.6: Phantom R^2 maps. The six slices from most inferior **(a)** to superior **(f)** are shown. Rectangular ROIs were drawn on each slice, indicating the voxels to be tested with the motion-mapping algorithm. Parametric maps representing R^2 values of the mono-exponential fit to the time series data for each voxel in the ROIs were overlaid on mean functional data. The border of the background image is disorderly due to irregularities in the surface of the phantom. The uniform $R^2 = 1.0$ results across slices **(c)** to **(f)** indicate that this material moved out of the imaged volume when the phantom was displaced. No voxels were flagged in slice **(a)**, since this material remained within the volume. The results were mixed in slice **(b)**, since that slice was on the edge of the field-of-view after displacement.

all trials (SD 200). 44 ± 12% of voxels had superior-inferior motion indicated by the algorithm. Of the voxels that were left out of the maps because no motion was identified, 92 ± 3% were eliminated based on parameter constraints and 8 ± 3% were eliminated based on R^2.

Motion maps for superior and inferior displacement from three representative trials on different subjects are shown in Figure 3.8. The maps indicate superior (proximal) motion especially in the triceps surae near the deep aponeuroses of the triceps surae (DA). Inferior (Distal) motion is apparent in the triceps surae farther from the DA (anterior SM and superficial MGM and LGM), and in the anterior compartment (TAM and EM).

Fitting proceeded successfully across trials with one exception: in one trial, a

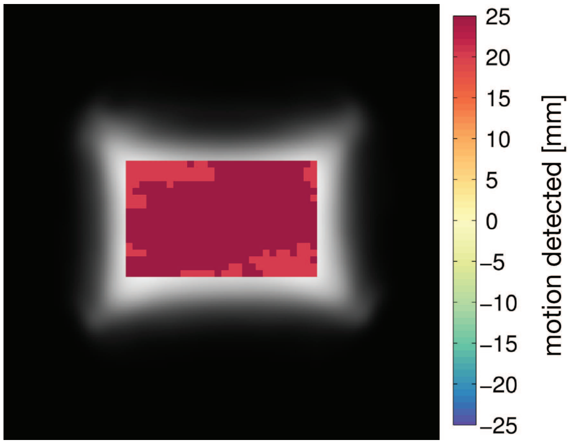

Figure 3.7: Phantom motion map. A map of phantom motion was generated from the six slices of R^2 values. The map was overlaid on the mean functional image.

scanner acquisition error occurred during the exercise phase, leaving 11 trial data sets from the 6 subjects. There was no statistically significant difference between the two runs (i.e. the Student's T-test failed to reject the null hypothesis at $P = 0.05$), so data from both trials of all subjects were combined at the group level, and the quotient of motion voxels to ROI voxels was examined. Most ROIs included regions of both superior and inferior motion, but the anterior compartment (EM and TAM) was the exception: those ROIs had almost uniform inferior motion and very little superior motion across all subjects. A plot of the fractions is shown in Supplementary Section 3S.

Group results were further examined based on the spatial proximity of motion voxels to the DA (Fig. 3.9). The upper plots demonstrate that voxels near the aponeuroses moved superiorly; majorities of voxels within 5 mm of the DA had motion indicated, with the proportions decreasing with greater distance. The lower plots show that both a greater number and a greater fraction of voxels farther from the DA moved inferiorly.

3.4 Discussion

The motion maps produced from this method provide valuable information for examining muscle using the GRE EPI technique. Conveniently, one can likely extract the displacement information without undue alteration of exercise or scanning protocols. The post-processing algorithm discerns areas of muscle motion for

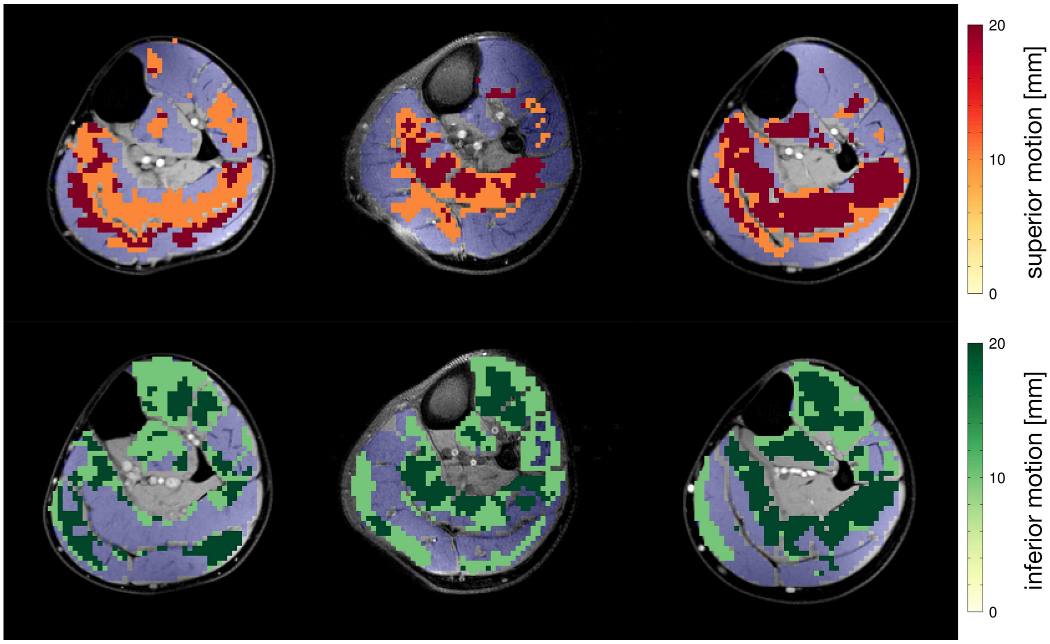

Figure 3.8: **In-vivo motion maps**. Maps from three representative trials are shown. Magnitudes of superior **(top)** and inferior **(bottom)** displacements are indicated by the colour scales, while blue tinted areas indicate voxels where the algorithm did not detect motion. Maps were overlaid on appropriate slices (superior or inferior) from subject structural images.

the exercise undertaken. Thus displacements during a particular exercise can be examined per subject, provided the exercise can be performed in the MRI scanner. The displacement maps may be converted to strain values given the pennation angle of the muscles. However, care must be taken in interpretation of the values as muscle activation, as has been done previously (Finni et al., 2006), since passive motion is evident in the motion maps as well.

Furthermore, the phantom testing provided quantitative validation that the method provides accurate motion maps. The experiment also demonstrated that the measurement uncertainty using this method is equivalent to the full thickness of one slice. This was clear because the motion map had values of 20 and 25 mm, while the true motion was 20 ± 2 mm. Once the displacement of a voxel extended beyond four slices (20 mm), it was labelled as having moved by five slices (25 mm).

The in-vivo motion voxels identified by the algorithm were consistent with PF exercise, as demonstrated by the plots of voxel proximity to the DA. The DA moves superiorly along with the Achilles tendon, and the maps reflect that across subjects:

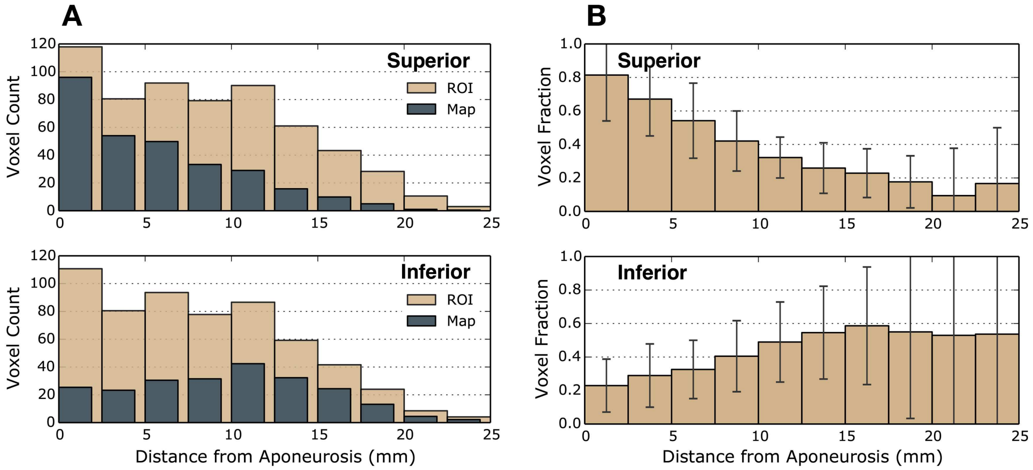

Figure 3.9: Motion proximity to deep aponeurosis. The plots show the proximity of voxels in the triceps surae (MGM, LGM and SM) to the deep aponeuroses (DA, see Fig. 3.3). **(A)** Mean voxel counts from all trials, identified as displaced (darker bars), and total examined (lighter bars). **(B)** Bar heights represent the quotient of the two bars from (A). Error bars represent the standard deviation across trials. The error bars of the distant voxels are particularly large because of the small absolute number of such voxels. The method identified 80% of voxels next to the DA has having been displaced superiorly, with a monotonic decrease with increasing distance from the DA. In the inferior direction, 20% of voxels next to the DA were identified as having moved, with a much greater proportion distant from the DA.

80% of tested voxels that were next to the DA were found to move superiorly, and the fraction decreased steadily as the distance from the DA increased. Furthermore, most voxels that moved inferiorly were farther from the DA. Prior muscle motion studies (eg. Kinugasa et al., 2008; Shin et al., 2009) have reported very little motion at the superficial aponeuroses of the gastrocnemius, though inferior motion was clearly present in that area of the maps produced by the current method. This may be due to the isometric contractions employed previously as opposed to the isotonic exercise performed here. This would be expected to produce different strain distributions (Chi et al., 2010). Some individual variability was notable in the maps. Individual variability of PF activation patterns in muscles outside the triceps surae has been reported previously (Finni et al., 2006). Finally, in extensor digitorum and hallucis longus muscles (EM) and TAM, which are antagonistic to PF, almost every voxel moved inferiorly in most trials. This result was due to the passive pull on these muscles during PF. The directionality of the muscle motion, including the inferior motion of the superficial gastrocnemius, was corroborated in the ultrasound measurements of both areas examined: (1) in the MGM, superior motion occurred near the deep aponeurosis and inferior motion superficially; (2) inferior motion was observed across the entire TAM.

Several methodological considerations are relevant to this new method. First, the constraints on the fit parameters were strong enough to reject data with no motion, as verified by running the algorithm on data without the initial post-exercise points. This yielded an empty motion map as expected. Second, although not actually an outlier by the common definition (Boslaugh and Watters, 2008), the motion map from one trial looked qualitatively different from the rest due to the large proportion of voxels in the inferior motion map. The superior map showed a similar pattern to other trials, with clustering near the DA. The inferior map had voxels in the motion map broadly covering the tibialis posterior muscle (TPM), peroneus longus and brevis muscles (PM), and anterior soleus muscle (SM) areas, to a greater extent than other trials. This may indicate a bulk displacement of the lower leg in the inferior direction occurred, which would confound this method.

In this study, the choice of three 10 mm thick slices were the minimum required to provide unambiguous motion maps for the exercise protocol, with muscle motion expected to extend across 1-2 slices. This choice was supported by previous reports stating that deep in the triceps surae, the inferior-superior displacement of muscle and connective tissues during PF is approximately 1 cm at the mid-calf level with 50% effort (Muramatsu et al., 2001; Arampatzis et al., 2005). The connective tissue motion is caused by a corresponding displacement of the muscle fibres in the vicinity, with attendant change in their pennation angle (Kawakami et al., 1998). The ultrasound examination results also indicated muscle displacement in the superior-inferior direction ranging from 5–18 mm. Increasing the number of GRE EPI slices across the same 30 mm through-plane FOV, as in the phantom protocol, would have provided displacement maps with higher precision.

Exercise protocols examining different muscles or using isometric contractions may need to *tune* the slice and total slab thicknesses based on expected muscle motion. If the prescribed image slab was too thin, muscle motion extending across the whole volume would produce maps of ambiguous direction and magnitude. The only motion information produced in that case would be the minimum displacement magnitude. Conversely, if image slices were prescribed too thick compared to the motion, the small desaturation of the tissue spins may not exceed the thresholds of the fit algorithm, and the motion would go undetected.

When discussing spoiled GRE sequences, Bernstein (2004) noted that the approach to steady state can deviate from the ideal case significantly, with specific reference to the study of Epstein et al. (1996) which used short T_R (10 ms) sequences. Resting EPI data in the present study were found to be an excellent fit (median R^2 of 0.997) to a mono-exponential curve, as expressed in Eq. (3.4). Comparing the amplitude of exponential fits to initial *rest* data ($S_0 = 800 \pm 200$) with the plots of curve fitting to *post-ex* data, one can see that the *post-ex* exponential decays had lower amplitudes closer to $S_0 = 150 \pm 50$. This was expected since the contraction frequency was 0.5 Hz, so the muscle tissue spins could not have spent enough time out of the imaged volume for the magnetization to completely relax. It may also be indicative of the fact that, in most cases, less than the full 10 mm thickness of the muscle slice was outside the imaged volume during contraction, resulting in partial relaxation of a voxel's magnetization. Future GRE EPI muscle studies may also wish use the fitting method described here only to remove the contaminating exponential trend from the signal of interest, rather than to quantify motion.

One of the main advantages of our method of motion mapping compared to others is the ability to use almost any exercise protocol. Although the method clearly works for the dynamic exercise performed in this study, as do the phase-contrast and spin-tag methods (Sinha et al., 2004), a static flexion or single contraction exercise protocol would likely work even better. A static flex would keep displaced tissue outside the imaging volume for longer periods and allow the signal to relax back closer to initial levels, causing the saturation exponential fits to have greater amplitudes. A greater contraction force (e.g. 100% 1RM) is also possible with this motion mapping method. This is because subjects need only perform the contraction once, rather than the dozens of synchronized repetitions necessary to get good phase-contrast images.

The main limitation of the method implemented in this study is that it provides only crude displacement data. Thinner slices would be needed to get more subtle strain values. Although 10 mm slices have often been used in muscle GRE EPI studies (Meyer et al., 2004; Wigmore et al., 2004; Towse et al., 2005, 2011), 5 mm slices also provide adequate signal to noise, even at 1.5 T (Ledermann et al., 2006; Schulte et al., 2008; Partovi et al., 2012). Thus, a study employing thinner slices is feasible, and would provide greater precision. Of course, a trade-off would have to be made between the temporal and spatial resolutions of the scan, keeping in mind that the time constant of the effect seen in this study was $\tau = 0.63 \pm 0.06$ s. An advantage of the phase-contrast method is that it can be prescribed on a sagittal oblique plane to get displacement information along the length of the aponeurosis. The present method relies on through-plane tissue displacement, so it must be prescribed perpendicular to the expected motion (axially in this study). Of course, the axial slice also provides information on the deep plantar flexors and antagonist muscles, which are not simultaneously visualized on a sagittal oblique plane.

3.5 Conclusion

This study demonstrated the extraction of muscle displacement information from GRE EPI time series MR images following exercise. The novel post-processing scheme developed here provided through-plane motion maps in agreement with ultrasound measures. Although the technique provides rough measures of displacement compared to the established methods, it nevertheless adds this valuable and completely complementary information to functional data sets without the need for a separate scan or extraordinary adjustments to scan or exercise parameters.

3A Appendix

3A.1 GRE signal approach to steady state

When a GRE sequence is started, the signal takes time to come into dynamic equilibrium (i.e. steady state). The steady state signal, S_{ss}, depends on the type of GRE sequence. For a spoiled GRE sequence, such as the one used in this study, the steady state signal magnitude is given by (Bernstein, 2004):

$$S_{ss} = M_0 \sin\alpha \, f_{z,ss} e^{-T_E/T_2^*}, \tag{3.2}$$

where M_0 is the initial longitudinal magnetization, α the excitation flip angle, T_E the echo time, and T_2^* the effective transverse relaxation time. The dimensionless quantity $f_{z,ss}$ is the ratio of the steady state to the initial longitudinal magnetization, M_{ss}/M_0, and depends on the pulse repetition time, T_R, as follows:

$$f_{z,ss} \equiv \frac{1 - e^{-T_R/T_1}}{1 - \cos\alpha\, e^{-T_R/T_1}}. \tag{3.3}$$

When the pulse sequence is first started, the spins are in a non-equilibrium condition. Under this condition, the signal obtained from pulse n of a spoiled gradient echo pulse sequence depends on the initial z-magnetization as follows (after Bernstein, 2004):

$$S(n) = M_0 \sin\alpha\, e^{-T_E/T_2^*} \left[f_{z,ss} + (\cos\alpha\, e^{-T_R/T_1})^n (1 - f_{z,ss})\right] \qquad (n = 0, 1, 2, \ldots). \tag{3.4}$$

Making the substitutions $A = M_0 \sin\alpha\, e^{-T_E/T_2^*}$, $B = \cos\alpha\, e^{-T_R/T_1}$, and using $B^n = e^{n \ln B}$, this can be written as:

$$S(n) = A f_{z,ss} + A(1 - f_{z,ss}) e^{n \ln B} \qquad (n = 0, 1, 2, \ldots). \tag{3.5}$$

By converting the acquisition number to time using $t = nT_R$, this can be expressed as a decaying exponential in time as:

$$S(t) = S_0 e^{-t/\tau} + C, \tag{3.6}$$

which yields the following parameter definitions:

$$\begin{aligned} S_0 &= A(1 - f_{z,ss}) &&= M_0 \sin\alpha\, e^{-T_E/T_2^*}(1 - f_{z,ss}), \\ \tau &= -T_R/\ln B &&= -T_R/\ln(\cos\alpha\, e^{-T_R/T_1}), \\ C &= A f_{z,ss} &&= M_0 \sin\alpha\, e^{-T_E/T_2^*} f_{z,ss}. \end{aligned}$$

In the limit $t \to +\infty$, we have $S = C$; in other words, Eq. (3.6) reduces to the equilibrium condition of Eq. (3.2).

3A.2 Image analysis algorithm details

First, each *post-ex* EPI time series was viewed to determine the image index representing the end of exercise (denoted i_0 here). The motion correction parameters were also consulted for confirmation. The time series of voxels in images subsequent to i_0 were analyzed and motion maps were generated using a custom written MATLAB program. It operated as follows:

(i) First 15 post-exercise data points ($i_0 \rightarrow i_{14}$, approximately 5 time constants) extracted for exponential fitting.

(ii) Linear detrending: next 100 points ($i_{15} \rightarrow i_{114}$) extracted to establish the underlying linear trend of the *post-ex* data. A linear least-squares fit was performed. The linear trend originates from changes in blood oxygenation and volume during the post-exercise period (Towse et al., 2011).

(iii) Linear curve was extrapolated back and subtracted from $i_0 \rightarrow i_{14}$.

(iv) Exponential fit to Eq. (3.6) performed on detrended $i_0 \rightarrow i_{14}$ in the non-linear least-squares sense.

(v) Voxels with successful fits were included in the results map overlays if they met the parameter estimate constraints, discussed below.

The fitting procedure was repeated while varying the value of i_0 four times (relative values of -1, +1, +2, +3) to produce the best possible fit for a voxel, selected as the highest R^2. This was necessary to ensure that each voxel had the motion of the final contraction removed, while allowing for the fact that different muscles relaxed with different timing.

The voxel slice location established motion direction, so that voxels identified in the motion map on the superior side of the slice stack had presumably moved superiorly, and inferior motion voxels having moved inferiorly. To establish the total displacement of a voxel, fit maps from adjacent slices deeper in the stack were examined to determine how far motion had extended outside the imaged volume. The displacements of motion map voxels were presented as statistical map overlays on the structural images.

3A.3 Parameter estimate constraints

Constraints on the parameter estimates from the fitting of Eq. (3.6) to the *post-ex* signal were necessary. Longitudinal magnetization recovers while muscle tissue is outside the imaged volume during a contraction, then quickly returns to dynamic equilibrium upon the tissue's return to rest position. Therefore, a mono-exponential decrease was expected from the signal curve fits, establishing a fit constraint of $S_0 + \mathrm{SE}(S_0) > 0$, where SE indicates standard error of the parameter from the fit. To establish a constraint on the time-constant of decay, the 40 initial time points (i.e. 0–10 s) of the resting GRE EPI scans were fit with mono-exponential decay curves (Eq. (3.6)), while the signal approached steady state. The median R^2 value across all voxel time series fits was 0.997, indicating very high fidelity fitting of this region of the data. The median and median absolute deviation values across trials were $S_0 = 800 \pm 200$, $\tau = 0.63 \pm 0.06$ s, and $C = 900 \pm 100$. This established a conservative (factor of 3) cut-off for the time constant in the fit-map algorithm at $\tau + \mathrm{SE}(\tau) < 2.0$ s. Voxel time-series fits not meeting these constraints on S_0 and τ were deemed unphysical and thus eliminated from motion maps.

The final constraint on the fitting algorithm was based on the R^2 value of the fit to the time series data of a particular voxel. Given that the R^2 statistic indicates the amount of variance accounted for by the fit-curve (Boslaugh and Watters, 2008), a constraint was established on curve fits as $R^2 > 0.60$, and voxels not meeting this criterion were eliminated from the fit map. This constraint required that a mono-exponential decrease was actually present in the data, given that a 60% majority of the signal variation was accounted for by the fitted curve.

When considering the proportion of voxels eliminated from motion maps based on constraint considerations, it is worth noting the order of the algorithm. The algorithm eliminated voxels based on parameter estimate constraints first, then by R^2 threshold. This means that some of the voxels eliminated for generating unphysical parameter estimates may also have had low R^2 values.

The slice profile of an imaging experiment may influence this method as well. The two dimensional (2D) slice profiles in real world MRI scanners are known to deviate in shape from the ideal of perfect rectangles. The true slice thickness may vary by 0.5 mm on 5 mm slices (Chen et al., 2004), and 15% of the radio-frequency (RF) energy intended for a slice may fall outside of it (Bourel et al., 1999). The stray RF reduces the precision of the method, since excitation energy applied to spins that have moved just outside the image volume would prevent their full relaxation. This places a lower bound on the possible precision of this method. With no prescribed slice gap, imperfect slice profiles would not be expected to influence this method for tissue moving across the imaged volume. This would have led to spurious motion identified in the phantom, which did not occur.

References

Arampatzis, A., S. Stafilidis, G. DeMonte, K. Karamanidis, G. Morey-Klapsing, and G. P. Brüggemann. 2005. "Strain and elongation of the human gastrocnemius tendon and aponeurosis during maximal plantarflexion effort." *J Biomech* 38: 833–841.

Bernstein, M. A. 2004. "Gradient echo." In "Handbook of MRI Pulse Sequences," pp. 579–606. Burlington, MA: Elsevier Academic Press.

Boslaugh, S. and P. A. Watters. 2008. *Statistics in a Nutshell.* Sebastopol, CA: O'Reilly Media.

Bourel, P., D. Gibon, E. Coste, V. Daanen, and J. Rousseau. 1999. "Automatic quality assessment protocol for MRI equipment." *Med Phys* 26: 2693–2700.

Carlier, P. G., D. Bertoldi, C. Baligand, C. Wary, and Y. Fromes. 2006. "Muscle blood flow and oxygenation measured by NMR imaging and spectroscopy." *NMR Biomed* 19: 954–967.

Chen, C.-C., Y.-L. Wan, Y.-Y. Wai, and H.-L. Liu. 2004. "Quality assurance of clinical MRI scanners using ACR MRI phantom: preliminary results." *J Digit Imaging* 17: 279–284.

Chi, S.-W., J. Hodgson, J.-S. Chen, V. R. Edgerton, D. D. Shin, R. A. Roiz, and S. Sinha. 2010. "Finite element modeling reveals complex strain mechanics in the aponeuroses of contracting skeletal muscle." *J Biomech* 43: 1243–1250.

Cox, R. W. 1996. "AFNI: software for analysis and visualization of functional magnetic resonance neuroimages." *Comput Biomed Res* 29: 162–173.

Damon, B. M., J. L. Hornberger, M. C. Wadington, D. A. Lansdown, and J. A. Kent-Braun. 2007. "Dual gradient-echo MRI of post-contraction changes in skeletal muscle blood volume and oxygenation." *Magn Reson Med* 57: 670–679.

Davis, A. D. and M. D. Noseworthy. 2016. "Motion and distortion correction of skeletal muscle echo planar images." *Magn Reson Imaging* 34: 832–838.

Drace, J. E. and N. J. Pelc. 1994. "Measurement of skeletal muscle motion in vivo with phase-contrast MR imaging." *J Magn Reson Imaging* 4: 157–163.

Epstein, F. H., J. P. Mugler, and J. R. Brookeman. 1996. "Spoiling of transverse magnetization in gradient-echo (GRE) imaging during the approach to steady state." *Magn Reson Med* 35: 237–245.

Ernst, R. R. and W. A. Anderson. 1966. "Application of Fourier transform spectroscopy to magnetic resonance." *Rev Sci Instrum* 37: 93.

Finni, T., J. A. Hodgson, A. M. Lai, V. R. Edgerton, and S. Sinha. 2003. "Nonuniform strain of human soleus aponeurosis-tendon complex during submaximal voluntary contractions in vivo." *J Appl Physiol* 95: 829–837.

Finni, T., J. A. Hodgson, A. M. Lai, V. R. Edgerton, and S. Sinha. 2006. "Muscle synergism during isometric plantarflexion in achilles tendon rupture patients and in normal subjects revealed by velocity-encoded cine phase-contrast MRI." *Clin Biomech* 21: 67–74.

Fukunaga, T., Y. Kawakami, S. Kuno, K. Funato, and S. Fukashiro. 1997. "Muscle architecture and function in humans." *J Biomech* 30: 457–463.

Haacke, E. M., R. W. Brown, M. R. Thompson, and R. Venkatesan. 1999. "Magnetic properties of tissues: Theory and measurement." In "Magnetic Resonance Imaging: Physical Principles and Sequence Design," pp. 741–779. New York: John Wiley & Sons.

Hodgson, J. A., T. Finni, A. M. Lai, V. R. Edgerton, and S. Sinha. 2006. "Influence of structure on the tissue dynamics of the human soleus muscle observed in MRI studies during isometric contractions." *J Morphol* 267: 584–601.

Hunter, J. D. 2007. "Matplotlib: A 2D graphics environment." *Comput Sci Eng* 9: 90–95.

Jenkinson, M., C. F. Beckmann, T. E. J. Behrens, M. W. Woolrich, and S. M. Smith. 2012. "FSL." *Neuroimage* 62: 782–790.

Jenkinson, M. and S. Smith. 2001. "A global optimisation method for robust affine registration of brain images." *Med Image Anal* 5: 143–156.

Kawakami, Y., Y. Ichinose, and T. Fukunaga. 1998. "Architectural and functional features of human triceps surae muscles during contraction." *J Appl Physiol* 85: 398–404.

Kinugasa, R., D. Shin, J. Yamauchi, C. Mishra, J. A. Hodgson, V. R. Edgerton, and S. Sinha. 2008. "Phase-contrast MRI reveals mechanical behavior of superficial and deep aponeuroses in human medial gastrocnemius during isometric contraction." *J Appl Physiol* 105: 1312–1320.

Ledermann, H. P., H.-G. Heidecker, A.-C. Schulte, C. Thalhammer, M. Aschwanden, K. A. Jaeger, K. Scheffler, and D. Bilecen. 2006. "Calf muscles imaged at BOLD MR: correlation with TcPO2 and flowmetry measurements during ischemia and reactive hyperemia–initial experience." *Radiology* 241: 477–484.

Ljunggren, S. 1983. "A simple graphical representation of Fourier-based imaging methods." *J Magn Reson* 54: 338–343.

Meyer, R. A., T. F. Towse, R. W. Reid, R. C. Jayaraman, R. W. Wiseman, and K. K. McCully. 2004. "BOLD MRI mapping of transient hyperemia in skeletal muscle after single contractions." *NMR Biomed* 17: 392–398.

Monti, R. J., R. R. Roy, J. A. Hodgson, and V. R. Edgerton. 1999. "Transmission of forces within mammalian skeletal muscles." *J Biomech* 32: 371–380.

Muramatsu, T., T. Muraoka, D. Takeshita, Y. Kawakami, Y. Hirano, and T. Fukunaga. 2001. "Mechanical properties of tendon and aponeurosis of human gastrocnemius muscle in vivo." *J Appl Physiol* 90: 1671–1678.

Murray, M. P., G. N. Guten, J. M. Baldwin, and G. M. Gardner. 1976. "A comparison of plantar flexion torque with and without the triceps surae." *Acta Orthop Scand* 47: 122–124.

Noseworthy, M. D., A. D. Davis, and A. H. Elzibak. 2010. "Advanced MR imaging techniques for skeletal muscle evaluation." *Semin Musculoskelet Radiol* 14: 257–268.

Oomens, C. W. J., M. Brekelmans, and F. P. T. Baaijens. 2009. "The mechanical behaviour of fibres." In "Biomechanics: Concepts and Computation," pp. 50–68. Cambridge, UK: Cambridge University Press.

Partovi, S., A.-C. Schulte, B. Jacobi, M. Klarhöfer, A. B. Lumsden, M. Loebe, M. G. Davies, G. P. Noon, C. Karmonik, L. Zipp, G. Bongartz, and D. Bilecen. 2012. "Blood oxygenation level-dependent (BOLD) MRI of human skeletal muscle at 1.5 and 3 T." *J Magn Reson Imaging* 35: 1227–1232.

Schulte, A.-C., M. Aschwanden, and D. Bilecen. 2008. "Calf muscles at blood oxygen level-dependent MR imaging: aging effects at postocclusive reactive hyperemia." *Radiology* 247: 482–489.

Shin, D. D., J. A. Hodgson, V. R. Edgerton, and S. Sinha. 2009. "In vivo intramuscular fascicle-aponeuroses dynamics of the human medial gastrocnemius during plantarflexion and dorsiflexion of the foot." *J Appl Physiol* 107: 1276–1284.

Sinha, S., J. A. Hodgson, T. Finni, A. M. Lai, J. Grinstead, and V. R. Edgerton. 2004. "Muscle kinematics during isometric contraction: Development of phase contrast and spin tag techniques to study healthy and atrophied muscles." *J Magn Reson Imaging* 20: 1008–1019.

Towse, T. F., J. M. Slade, J. A. Ambrose, M. C. DeLano, and R. A. Meyer. 2011. "Quantitative analysis of the postcontractile blood-oxygenation-level-dependent (BOLD) effect in skeletal muscle." *J Appl Physiol* 111: 27–39.

Towse, T. F., J. M. Slade, and R. A. Meyer. 2005. "Effect of physical activity on MRI-measured blood oxygen level-dependent transients in skeletal muscle after brief contractions." *J Appl Physiol* 99: 715–722.

Trotter, J. A. 2002. "Structure-function considerations of muscle-tendon junctions." *Comp Biochem Physiol A Mol Integr Physiol* 133: 1127–1133.

Wigmore, D. M., B. M. Damon, D. M. Pober, and J. A. Kent-Braun. 2004. "MRI measures of perfusion-related changes in human skeletal muscle during progressive contractions." *J Appl Physiol* 97: 2385–2394.

3S Supplementary material

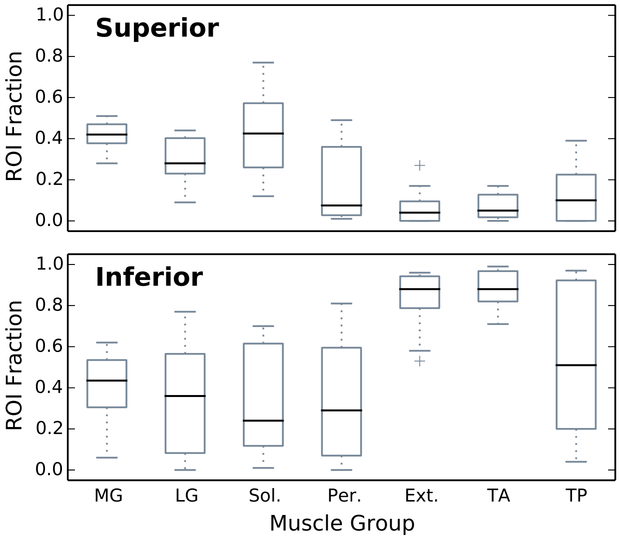

Figure 3.10: Fit voxels by muscle group. The plots show the fraction of motion voxels appearing in the superior and inferior muscle maps for each muscle group ROI. The horizontal lines and boxes represent median and inter-quartile ranges, respectively. The whiskers and fliers represent the data range and statistical outliers, respectively. The muscle ROIs are labelled in Figure 3.3.

Chapter 4

Signal uniformity and test-retest reliability in BOLD imaging of post-exercise skeletal muscle

Preface

The following chapter has not yet been submitted for publication. In some ways, the previous two chapters were preparatory for the analysis executed in this one. They represent preprocessing techniques for skeletal muscle GRE EPI data and an examination of an artifact in the signal immediately following exercise. The material in this chapter represents an analysis of the full post-exercise data set with an interest in its BOLD characteristics. The goal is to extract the most interesting features from the data in a reliable way. The consistency of the results among individuals and upon repeated scanning is examined. The technique developed here represents a multivariate approach to skeletal muscle BOLD that is lacking in the literature, and should certainly prove useful for future studies.

Abstract

Purpose. Gradient echo (GRE) echo planar imaging (EPI) is increasingly applied to skeletal muscle to acquire a time series of images for examination of physiological parameters. An examination of signal uniformity within muscle regions has been lacking in the literature. It is unknown how consistent or different the functional response of each muscle is during exercise, and how consistent the response is across trials and subjects.

Materials and Methods. Dynamic plantar flexion exercise, which primarily works the triceps surae muscles of the lower leg, was performed inside a 3 T MRI scanner. A time series of GRE EPI images was acquired before and immediately following the exercise. A probabilistic independent component analysis (PICA) framework was used to generate spatial parameter maps and temporal components. Correlations of spatial components to structural regions were examined, along with the signal uniformity within muscles. Intra- and intersubject test-retest reliability of components was examined.

Results. The probabilistic estimate for the optimal number of components returned very consistent intrasubject results, and 15 was selected as the best number of components for all exercise trials. The PICA method was shown to generate consistent components within and across subjects: all trials produced a component that was highly spatially correlated with the gastrocnemius within the first two, when the components were ordered by uniquely explained variance. Most trials also produced a soleus component that had very different temporal dynamics than the gastrocnemius. Vascular components with temporal dynamics previously unreported in the literature were also generated in every trial. Motion correction parameters were found to be highly correlated with post-exercise signal changes, but were not likely the cause of those changes based on an examination of the timing and the spatial extents of components.

Conclusion. This technique allows the reliable extraction of muscle tissue signals separated from the vessel they contain. The muscle and vessel signals have very different temporal characteristics, and the spatial extent of the vessel signal is difficult to predict without multivariate analysis.

4.1 Introduction

The magnetic resonance imaging (MRI) blood oxygenation level dependent (BOLD) effect is sensitive to the ratio of oxy to deoxy-hemoglobin. The ratio is determined by blood volume, flow and tissue metabolism, and is routinely applied for functional magnetic resonance imaging (fMRI) in the brain (Buxton, 2009). The BOLD technique is increasingly being used to examine physiological variations in skeletal muscle as well (Carlier et al., 2006; Noseworthy et al., 2010; Towse et al., 2011). Furthermore, BOLD imaging shows promise for evaluating disease states that affect skeletal muscle (Jacobi et al., 2012).

Whether changes to the BOLD signal are provoked by exercise or experimental ischemia, studies routinely gather time series data chronicling the effects using gradient echo (GRE) echo planar imaging (EPI). Further analysis is usually done on regions of interest (ROIs) to increase the signal-to-noise ratio (SNR) of the time series signals. Although an entire muscle's cross section is sometimes included in the ROI (e.g. Damon et al., 2007), many studies involve rectangular ROI selection from within a muscle (e.g. Ledermann et al., 2006; Schulte et al., 2008; Potthast et al., 2009; Partovi et al., 2012; Caterini et al., 2015). The resulting signal is taken as representative of the entire muscle. As far as we know, no functional studies have been performed to justify choosing a small ROI to represent the entire muscle, implying a homogeneous response throughout. A DTI study found that a sample of several ROIs in the lower leg had less intramuscular variance than inter-muscular variance in basic parameters such as fractional anisotropy, mean diffusivity, and λ_1 (Rockel and Noseworthy, 2016). In fact, evidence has been presented that suggests varying physiological response in triceps surae (TS) muscles following single short plantar flexion (PF) contractions; this has been shown in T_1-weighted GRE EPI images giving signal related to perfusion (Wigmore et al., 2004), and in spin echo EPI images measuring T_2, where less than half of muscle voxels were determined to be activated (Kinugasa et al., 2005). However in post-exercise data in the anterior compartment, cluster analysis of T_2-weighted images yielded single clusters in most subjects, suggesting homogeneous activation (Damon et al., 2003). This study sought to examine the homogeneity of the signal response in T_2^*-weighted GRE EPI images acquired following an intense exercise protocol.

Some studies that have examined post-contraction GRE EPI signals have attempted to directly interpret them physiologically (Damon et al., 2007; Towse et al., 2011; Davis and Noseworthy, 2013). However, the post-exercise skeletal muscle BOLD signal varies widely among subjects, even after carefully controlling relevant study parameters. One study showed that post-contraction hyperemia curves varied by approximately 20% following brief contractions (Wigmore et al., 2004). Another showed that the peak signal response varied by a factor of more than 3 according to subject athletic participation (Towse et al., 2005). It is clearly understood that this data is highly motion sensitive due to the dependence of the signal on the local field and the spin history; motion induced signals remain even after registration-based motion correction. Brain researchers have identified that frame-to-frame displacements as small as 0.2 mm can generate spurious signals that profoundly contaminate results in model-free fMRI analysis (Power et al., 2013, 2012; Van Dijk et al., 2012). Appropriate motion correction must be performed (Davis and Noseworthy, 2016), but the signal effects of motion should also be considered to ensure the source of signal variability is predominantly physiological. Thus, this study revolves around examining a common technique for dealing with motion in which motion correction parameters are regressed from the data, yielding a motion-free residual. Furthermore, the use of independent component analysis (ICA) as a blind source separation (BSS) technique is investigated as a means to separate signals from noise in a data-driven fashion to examine intrasubject test-retest reliability in post-exercise BOLD signals and pursue repeatable signals across subjects (Jutten and Herault, 1991; Hyvärinen and Oja, 2000).

4.2 Methods

Data was acquired from six healthy male volunteers (age 31 ± 9, BMI 22 ± 1) in a study approved by the local research ethics board. Plantar flexion exercise was performed using a custom built ergometer as described previously (Section 3.2). A one repetition maximum (1RM) test was performed at least one day prior to scanning in order to measure subjects' force generation capacity. Exercise performed during the scans consisted of 2.5 min of dynamic (0.5 Hz) PF exercise at 50% of a subject's 1RM.

Images were acquired using a 3 Tesla GE HD Signa MR scanner with a flexible single channel, receive-only coil (General Electric Healthcare, Milwaukee, WI). Each imaging session was comprised of two trials, with each trial having data acquisition before (*rest*, 10 min of data) and after (*post-ex*, 13 min of data) exercise. There was a 40 min rest between trials. The *post-ex* data acquisition was actually begun 30 s before the end of exercise, and exercise images were removed, as described below. Imaging parameters and timing have been described previously (Section 3.2). Briefly: following localizer and structural scans, three 10 mm slices (0 mm gap) of GRE EPI data with $T_E = 35$ ms and $T_R = 250$ ms were acquired at the largest cross-section of the calf (field of view (FOV) = 160 mm, matrix = 64×64, $\alpha = 33°$). Two gradient echo images were also acquired at the same locations as the functional data to generate B_0-field maps for EPI distortion correction ($T_E = 4.55/6.82$ ms for $\Delta T_E = 2.27$ ms; matrix size (MS) = 128×128; FOV, T_R, α matched EPI images; receive bandwidth (rBW) = 62.5 kHz).

Functional images were preprocessed using Bourne-again shell (BASH) shell scripts that relied on FSL and AFNI tools (Smith et al., 2004; Cox, 1996). Motion correction and unwarping of the EPI distortion was performed with programs developed specifically for muscle images as previously described (Davis and Noseworthy, 2016). Images were also masked to remove the background, slice timing corrected, and smoothed with a 5 mm full width at half maximum (FWHM) Gaussian filter. Smoothing was only applied in-plane as the images were already 10 mm thick. Data acquired during exercise and the 15 time points immediately following were removed to limit motion corruption of the data, and time series were truncated to a common number of frames (2880 = 12 min for *post-ex*, 2385 = 9.9 min for *rest*).

Seven muscle ROIs (Table 4.1) were manually drawn on subject structural images and transformed into the subject's functional space using linear registration. Two additional ROIs were created by combining the two regions of the gastrocnemius muscle (GM), and then further adding the soleus muscle (SM) to form the TS.

Probabilistic Independent Component Analysis

The post-exercise GRE EPI data was analyzed using probabilistic independent component analysis (PICA), as implemented by FSL's *Melodic* program (Beckmann and Smith, 2004). The tool estimated the optimal number of components to reveal the unique sources underlying the data, and performed data reduction using principal component analysis. Next, whitening with principal component analysis (PCA) was performed, during which the time series means were removed and they were variance normalized. This was followed by spatial ICA. A mask was applied during ICA processing to include only tissue voxels, and was dilated by 2 voxels to include those on the margins. After an initial PICA run to estimate the optimal

ROI	Descripton
1	Medial gastrocnemius muscle (MGM)
2	Lateral gastrocnemius muscle (LGM)
3	Soleus muscle (posterior region) (SM)
4	Peroneus longus and brevis muscles (PM)
5	Extensor digitorum and hallucis longus muscles (EM)
6	Tibialis anterior muscle (TAM)
7	Tibialis posterior muscle (TPM)
8	Gastrocnemius muscle (GM = MGM + LGM)
9	Triceps surae (TS = MGM + LGM + SM)

Table 4.1: ROI Descriptions. Anatomical description of the seven regions of interest (ROIs) drawn on subject structural images, as well as the two compound regions.

number of components across trials, a standardized value of 15 ICA components were extracted from each trial (see Figure 4.1). Spatial maps of component weights were output with the associated time series in normalized units. Components that were deemed to be noise contributors from gross motion were identified and regressed using a multivariate strategy to remove only the unique variance of the component. Next, a second ICA run was performed on the residual data with identical settings. Component weight maps from the second run were examined for high spatial correlation with manually drawn muscle ROIs. For display of the component weight maps, a Bayesian mixture model was performed with threshold set at 0.5 (representing an equal probability of false negatives and false positives). A more detailed discussion of PICA preprocessing considerations is provided in Appendix 4A.1.

Motion parameter examination

Based on the in-plane motion correction that was performed, three motion parameters were generated (left-right and anterior-posterior translation, in-plane rotation). The motion parameters were examined for correlations between subjects in both *rest* and *post-ex* data.

The association between the *post-ex* motion parameters and GRE EPI signals was also evaluated. First, twelve regressors were generated from the three parameters using the expansion method originally described by Friston et al. (1996), and

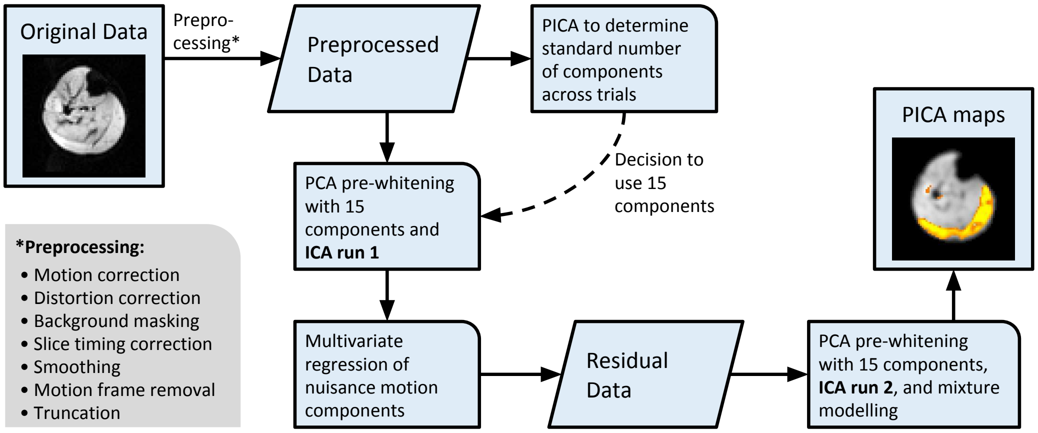

Figure 4.1: Data analysis method. Flow chart illustrating the PICA analysis method. Figures of later results come from ICA run 2.

often used for brain (e.g. Satterthwaite et al., 2013; Griffanti et al., 2014). The expansion includes the square of each component, and takes account of spin-history effects using the differential of the components and their squares. The parameters were regressed from the time series signals and the remaining variance was determined from the residual signals. This was reported as SS_{rel}, the relative sum-of-squares of the signal after regression compared to before.

To determine whether motion played a role in generating the post-exercise signal of interest, peak times in the motion parameter and gastrocnemius ROI signals were compared. The correlation of signal fluctuation in the gastrocnemius to motion parameters was also examined based on the following parameters at rest and post-exercise:

(i) *NTRg*, a measure of temporal fluctuation magnitude:

$$NTRg = \frac{1}{n}\sum_{i=1}^{n}\frac{S_{i,max} - S_{i,min}}{\overline{S_i}} \tag{4.1}$$

where n is the number of voxels in the gastrocnemius, and S_i is the signal in a voxel within that ROI.

(ii) *MCD*, the displacement range after the total motion correction parameters are converted to a single displacement value (in mm).

To determine whether signal and contrast changes in the time series of GRE

EPI images caused the motion parameter changes, the images were modified using custom written python programs in the following ways:

- Histogram modifications using a quarter-root transform to suppress contrast.
- Histogram matching to reduce contrast changes in the time-series.
- Images were cluster thresholded using Otsu's method (Otsu, 1979), and all voxels with signal above the threshold were assigned the threshold value.
- Masking was applied to the background to ensure ghosting was not affecting the motion correction.
- High-pass image filtering (Scharr differentiation) was applied to get an edge image of the leg-air interface, including masking of the interior and background areas.
- The cost function was changed to use mutual information, which is known to be less sensitive to differences in contrast.

The cluster thresholding and high-pass filtering steps used the *scikit-image* Python package (Van der Walt et al., 2014). Each modified data set was run through the motion correction program to determine whether the parameters had changed appreciably.

4.3 Results and Discussion

Data from subjects' 1RM tests and triceps surae muscle ROI volumes are shown in Table 4.2. The load values are specific to the ergometer used in this study with its particular force multiplying characteristics. There was wide variation in the composition of the TS, as shown by the relative volume occupied by GM. The total volume of the TS was the single measure found to have highest correlation (0.95) with subjects' 1RM values, giving R-squared $R^2 = 0.909$ (adjusted R-squared $R^2_{adj} = 0.886$) in a linear regression model. The addition of the relative volume of the TS occupied by GM was found to slightly improve the model, giving $R^2 = 0.934$ ($R^2_{adj} = 0.889$). Subject weight, height, and BMI were correlated with 1RM, while

Subject	1RM load (Kg)	BMI (Kg/m^2)	GM Vol. (cm^3)	SM Vol. (cm^3)	TS Vol. (cm^3)
1	12.2	21.7	45.7	35.2	80.8
2	20.6	24.5	54.7	62.1	116.8
3	11.2	21.5	41.3	47.1	88.4
4	19.7	23.7	65.4	52.6	118.0
5	18.8	21.9	51.7	67.9	119.5
6	15.5	21.4	47.1	50.0	97.1
1RM PCC		0.78	0.83	0.79	0.95

Table 4.2: Subject 1RM and Muscle Volumes. Measures of maximal pressed load and ROI volumes of various muscles of the lower leg for each subject. PCC: pearson correlation coefficient; 1RM: result of single repetition maximum test; BMI: body-mass index; ROI labels as in Table 4.1.

age was not ($R^2 = 0.000$); none of these measures increased R^2_{adj}. This indicates that subject performance in this exercise was mostly determined by the muscle volume of the TS, while the relative sizes of GM and SM also played role.

PICA Results

PICA was employed to avoid the problem of *overfitting* the data, in which so many components are extracted that interpretation is difficult due to splitting and a high number of noise components (Beckmann and Smith, 2004). The optimal numbers of components for ICA decomposition of the *post-ex* and *rest* data are shown in Table 4.3. The values were estimated using the Laplace approximation technique (*Melodic*'s default) for each trial. In *post-ex* data, high variance was observed between subjects, but the values for the two trials of a subject were more consistent; the correlation ratio was 0.978 (ICC 0.956), indicating very high inter-subject variance compared to intrasubject variance for the number of components. In *rest* data, the optimal numbers of components were an order of magnitude higher than the *post-ex* data. This indicates a lack of coherent signals accounting for a high proportion of the variance in the *rest* data.

On examination of the components, it was evident that too many *post-ex* components (45) were estimated for Subject 3. Many components seemed spurious, and others were highly temporally correlated; fewer estimated components would

Subject	PE1	PE2	R1	R2
1	20	7	218	253
2	16	13	309	161
3	45	45	226	218
4	3	3	404	473
5	9	13	360	419
6	12	13	337	407

Table 4.3: Estimated optimal number of components for ICA decomposition. Results under the PE1/2 headers refer to the two *post-ex* data collections for each subject, while R1/2 refer to the two data collections at rest, before exercise. Note the consistency of the number of *post-ex* components in Subjects 3 and 4, despite how different they are from others. The number of *rest* components are uniformly an order of magnitude greater than *post-ex*. This is likely due to the nature of the probabilistic determination: with no components individually accounting for large variance in the *rest* data, many more components are required to account for the total variance in the data set.

aid later inference and decrease computation time. Conversely, too few components (3) were estimated for Subject 4. Though the extracted components appeared salient, additional components were desirable to allow noise regression and reveal more subtle signals in the data. For further analysis, a standardized value of 15 components were extracted for each trial.

Based on visual inspection of the component spatial maps and time courses from the 15-component ICA run, a total of 24 components were identified for regression from the data (average 2.0 per trial, range $1-5$). Figure 4.2 shows two typical examples of regressed components.

It was also observed that a large number of components had spatial maps matching the vasculature, especially the arteries (Fig. 4.3). As it was not known whether these components contained useful information, they were not regressed, and therefore remained in the next ICA pass. The pulsatile aspects of these components could be effectively removed using low-pass filtering.

All further results are reported from the second ICA run on residual data, after regression of nuisance components. The list of components regressed and the full set of components returned before and after regression for every trial are shown in Appendix 4A.4. The components with highest spatial correlation to muscle ROIs are shown in Table 4.4; results shown are thresholded at $PCC > 0.4$ ($z-\text{score} >$

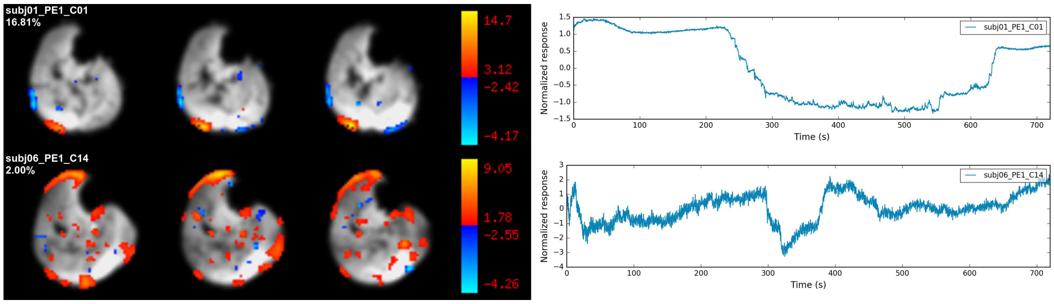

Figure 4.2: Regressed components. The figure shows two example components regressed from the data after the first ICA pass. The components are both good candidates for regression because: (1) the thresholded spatial maps (left) show strong edge effects, while (2) the time courses (right) defy physiological interpretation. The components in this and subsequent figures are identified by the subject number (*subj01–6*), the trial within an imaging session (*PE1* or *PE2*), and the component number (*C01–15*). The presence of *f* after the trial would indicate that this is the second ICA run, after the nuisance regressors have been filtered (e.g. *PE1f*).

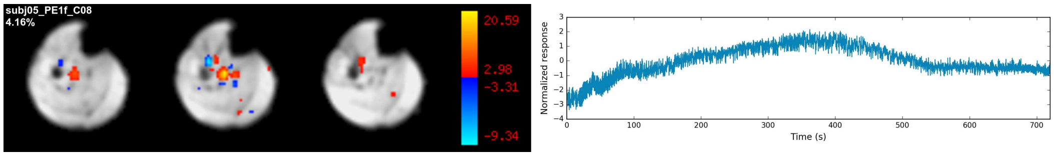

Figure 4.3: Arterial component. Typical component identified as having an arterial origin. The spatial weights (left) identify a vascular origin to the signal, especially the popliteal artery. The time course (right) represents a strong pulsatile signal, along with a low frequency trend. Labels as in Fig. 4.2.

2.5 including all trial data).

Gastrocnemius components

Every trial resulted in a component with high spatial correlation to the gastrocnemius (ROI 8 in Table 4.4). The thresholded component maps, shown in Figure 4.4, have similar spatial extent to the gastrocnemius, while sometimes including the lateral compartment as well (e.g. *subj02_PE1*). A second gastrocnemius correlated component from *subj06_PE1* was excluded from the figure, since it had a different time course shape from the rest (shown in Appendix 4A.4). The *subj04_PE2* trial had no gastrocnemius ROI represented in the table, but the component with highest correlation was included in the figure. In that trial, a splitting effect occurred across two components (numbers 1 and 2) that were correlated with the gastrocnemius (Pearson correlation coefficient (PCC) of 0.24 and 0.33 respectively), and matched the temporal shape of the other gastrocnemius independent components (ICs) (both shown in Appendix 4A.4).

These gastrocnemius correlated signal intensity changes were often evident by viewing the time-series of GRE EPI images, and accounted for a large amount of variance; the component was usually the primary one for a trial (10 trials), but was sometimes the second (2 trials). From the plots of the time courses in the figure, it can be seen that the components are also highly temporally correlated, with a median temporal correlation of 0.96, even with the plot of *subj02_PE2* included (purple line in the plot).

Soleus components

Another trend evident in Table 4.4 is the high prevalence of components correlated to the soleus (ROI 3). Upon inspection of the time courses, it was observed that most components could be visually categorized as either *decay* type (Fig. 4.5) or *wave* type (Fig. 4.6). All subjects were represented in the *decay* type figure except Subject 5, who contributed all four *wave* type components. Two soleus components that did not appear as the others are shown in Figure 4.7.

The *decay* type components had fair temporal correlation (median $PCC = 0.60$). They varied in initial normalized magnitude, but were consistent in qualitative shape. The shape consisted of an initial decay lasting approximately 10 s, followed

Trial	ROI 1 (MGM)	ROI 2 (LGM)	ROI 3 (SM)	ROI 4 (PM)	ROI 5 (EM)	ROI 6 (TAM)	ROI 7 (TPM)	ROI 8 (MGM+LGM)	ROI 9 (TS)
subj01_PE1	C02 (0.66)		C06 (0.46)					C02 (0.57)	
subj01_PE2	C01 (0.52)		C06 (0.46)∗					C01 (0.60)	
subj02_PE1			C06 (0.72)∗				C10 (0.58)	C01 (0.53)	
subj02_PE2							C03 (−0.50)	C01 (0.45)	
subj03_PE1	C01 (0.53)		C11 (0.43)∗	C12 (0.56)				C01 (0.64)	C12 (−0.40)
subj03_PE2	C02 (0.44)	C01 (0.61)		C10 (0.41)		C12 (0.42)	C11 (0.54)	C01 (0.58)	
subj04_PE1		C01 (0.42)	C02 (0.43)					C01 (0.42)	
subj04_PE2			C08 (0.44)∗						
subj05_PE1	C01 (0.61) C06 (0.57) C12 (−0.46)		C03 (0.60)† C13 (0.46)†	C02 (0.48)				C01 (0.76)	
subj05_PE2		C01 (0.59)	C03 (0.48)† C08 (0.52)†					C01 (0.40)	
subj06_PE1	C01 (0.42) C04 (0.52)		C05 (0.53)∗					C01 (0.44) C04 (0.55)	
subj06_PE2	C01 (0.46)	C01 (0.46)	C10 (0.59)∗				C09 (0.52)	C01 (0.66)	C01 (0.51)

Table 4.4: Spatial ICA component correlations with ROIs. Results thresholded to $|PCC| > 0.40$. Scattered correlations exist for most ROIs, but consistent results are found for ROI 8 (MGM+LGM) and ROI 3 (SM). SM component time courses were identified as *decay* type (∗) or *wave* type (†), as indicated. ROI abbreviations as in Table 4.1.

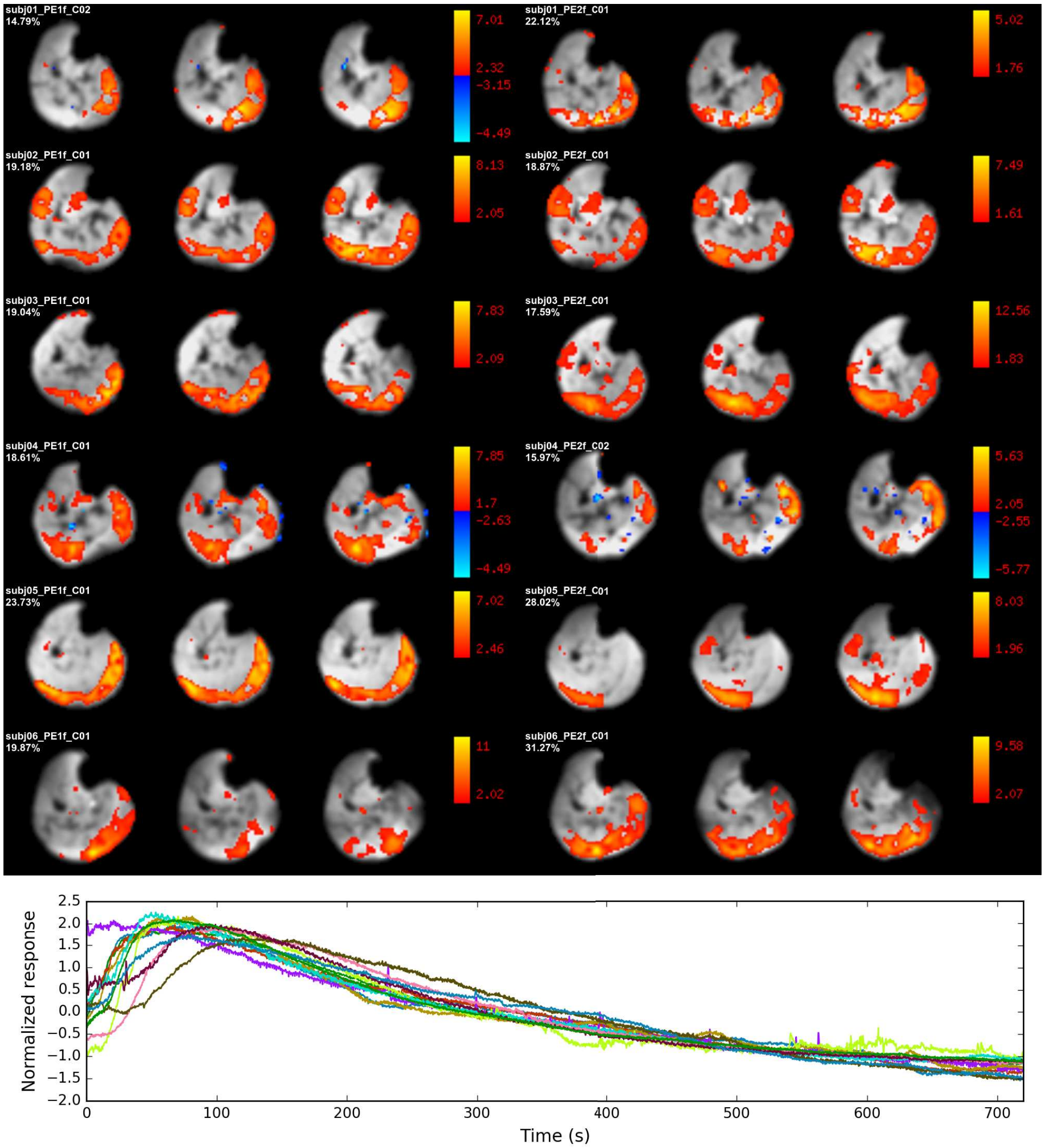

Figure 4.4: Gastrocnemius components. The components most correlated with the gastrocnemius from each trial are shown (ROI 8 in Table 4.4). The spatial extent of each component is shown, while the time courses are plotted together. The purple line in the plot represents *subj02_PE2*, for which a data acquisition problem early in the scan changed truncated the initial data. Labels as in Fig. 4.2.

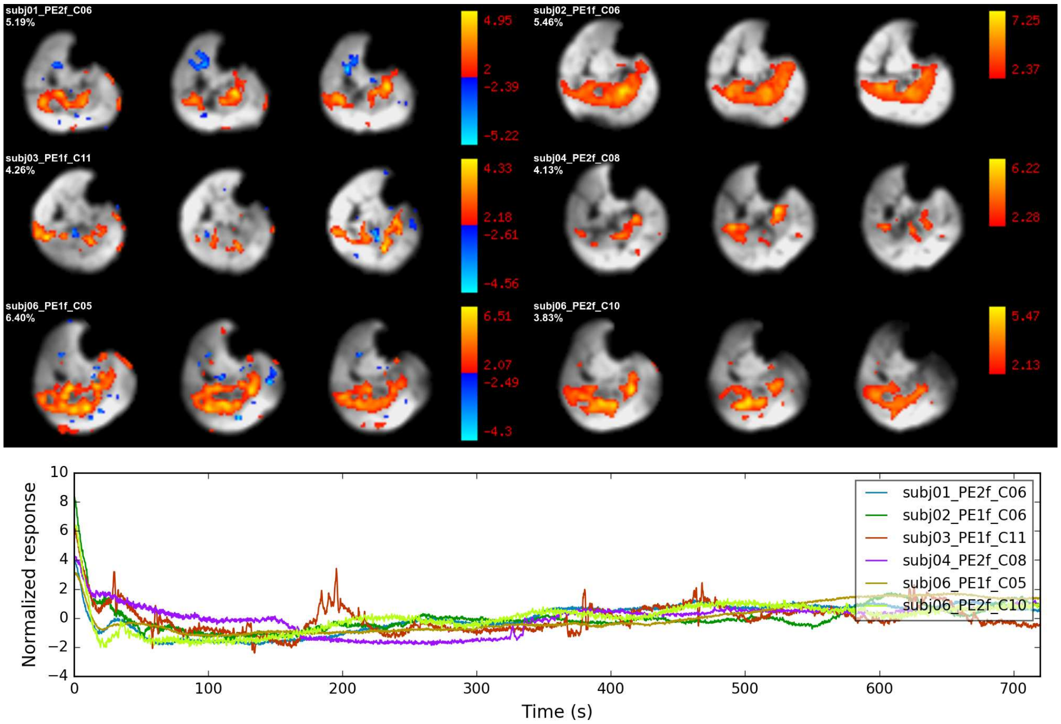

Figure 4.5: Soleus components (decay type). These components were spatially correlated with soleus muscle and identified as *decay* type. Labels as in Fig. 4.2. The quick peaks of *subj03_PE1f_C11* are likely residual motion signal that was not regressed.

by a bump or flat portion of about 20 s, then a long tail with a very gradual rise lasting for minutes until the finish of the scan. The small undulation occurring after most of the signal decrease occurred in most trials. This appears similar to the undulation in blood flow in the calf after exercise that was observed in an earlier plantar flexion study by Van Leeuwen et al. (1992).

The *wave* type soleus components from Subject 5 were very different from the other subjects, but were remarkably consistent between the *PE1* and *PE2* trials in some respects. Both trials produced a soleus component in their third ranked position with a simple temporal shape, and a component accounting for less variance that peaked sooner and was followed by an undershoot.

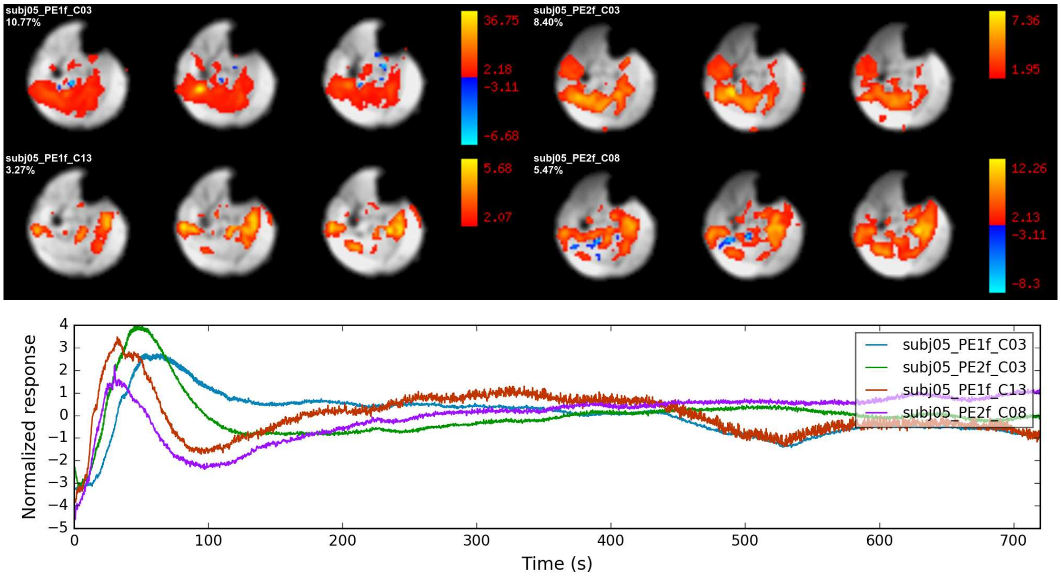

Figure 4.6: Soleus components (wave type). These components were spatially correlated with soleus muscle and identified as *wave* type. Labels as in Fig. 4.2. Note that these components came exclusively from Subject 5.

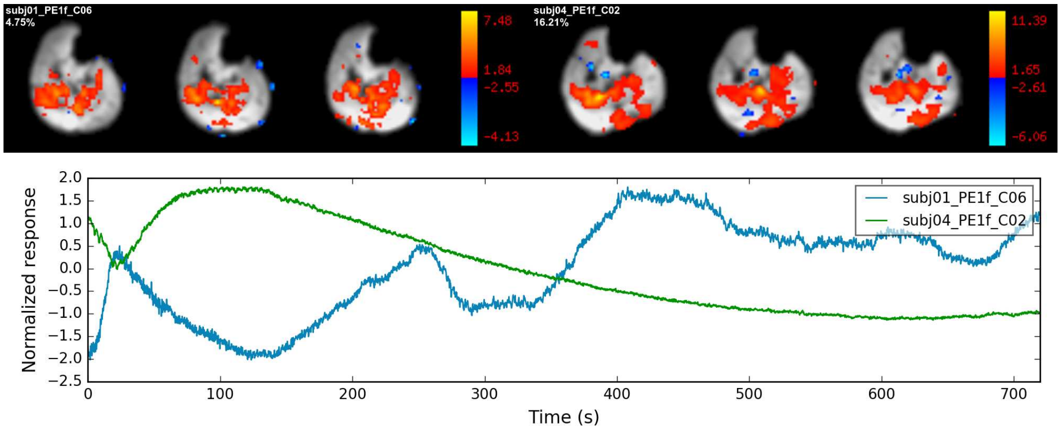

Figure 4.7: Soleus components (other type). These components were spatially correlated with soleus muscle and not identified in the other categories. Labels as in Fig. 4.2.

Other muscles

The peroneus longus and brevis muscles (PM) in the lateral compartment are known to be involved in PF along with the TS. Though only a few components in the data were shown to be correlated exclusively with the PM, several trials produced components correlated to regions in the TS and the PM. As shown in Appendix 4A.4, these included trials from Subjects 2, 3, 4, and 5.

The posterior tibialis muscle was also represented several times in Table 4.4. This muscle is known to aid in PF as well. Along with the isolated examples, it sometimes appeared in a component with the lateral compartment, as in *subj04_PE2f_C10*, and in a component with the gastrocnemius, as in *subj06_PE1f_C04*.

The tibialis anterior and extensor digitorum muscles, which oppose PF contractions, were not heavily represented in the spatial component maps or Table 4.4. The one example in the table, *subj03_PE2f_C12*, represents a component with a large noise contribution.

Two-crest components

Visual inspection of the components revealed another striking and unexpected feature. Almost all trials produced at least one component with a temporal shape resembling a wave with two crests, the first being lower and shorter than the second (Figure 4.8). The only exception was *subj02_PE2*, for which the crucial initial data was lost. In total 21 such components were identified in the data by visual inspection. Though the qualitative shapes were consistent, the timing differed, resulting in moderate temporal correlation across the ICs (median $PCC = 0.59$). The typical timing of the second crest was later than the gastrocnemius component. Examining the spatial weights of the ICs, small isolated regions within the gastrocnemius were heavily represented, likely being associated with veins. The components of Subject 5 were exceptional, in that the timing was more rapid than other subjects, and shorter than the GM component in this subject. Spatially, the components of Subject 5 were also localized to regions in the anterior soleus rather than the GM.

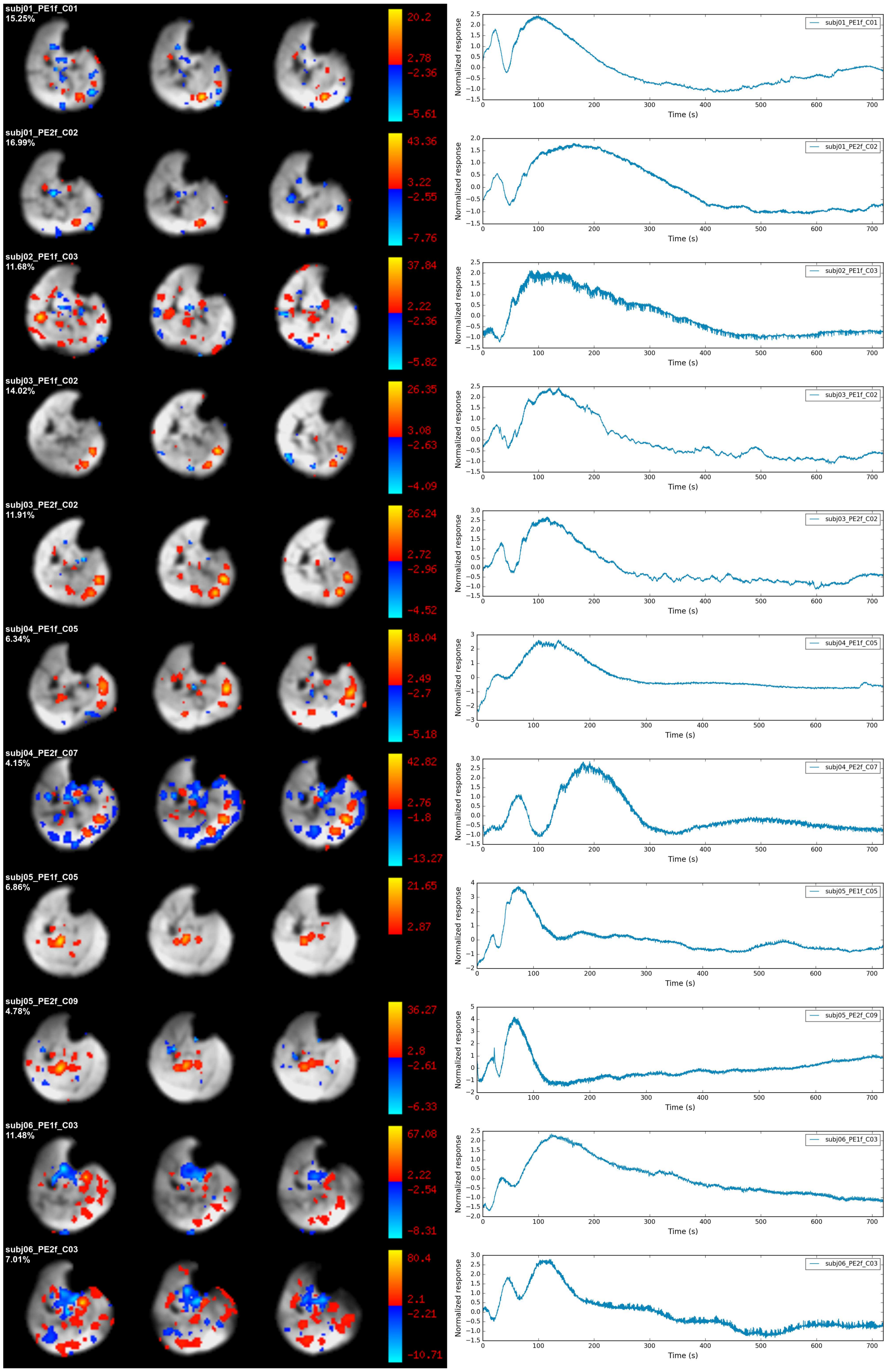

Figure 4.8: Example *two-crest* independent components. The highest ranked *two-crest* component identified from each trial is shown, with a full list given in the Appendix 4A.4. Labels as in Fig. 4.2.

PICA results considered

The PF exercise studied primarily works the TS, so it is not surprising that the components most correlated to muscle ROIs came from this region. More interesting was the difference in shape between the soleus and gastrocnemius components, observed when comparing subjects. Possible explanations for this difference include the varying workload from the two muscles, and also the differing blood vessel organization. The venous structure of the gastrocnemius runs in a well ordered fashion along the muscle fibres from distal to proximal, while the soleus venous structure is less ordered, more like a mesh (Hara, 2008). The soleus muscle also contains a greater number of venous sinuses for blood collection (Meissner, 2005). This difference in the amount of deoxy-hemoglobin (HHb) in the ROI and it's rate of outflow is likely to have a large effect on the BOLD signal characteristics within muscles, given the high signal sensitivity to blood (Zhao et al., 2007).

The PICA components that are correlated to muscles define functional units at the subject level. These ROIs follow anatomical boundaries to a large extent, which is important to muscle researchers who are looking for a uniform ROI to study. In other words, this study validates to a certain extent the method some authors use, selecting a small rectangular ROI from a muscle and assuming uniformity (e.g. Caterini et al., 2015). Care must be taken in the vicinity of blood vessels, however, as draining veins often seem to follow the *two-crest* temporal characteristic. Even small veins that are difficult to identify from a structural scan can cause large areas within the muscle to have a very different measured response (Fig. 4.9). This is likely to cause problems when a large swath of muscle is taken as a representative ROI, but actually contains a mixture of muscle and vessel signals (e.g. Muller et al., 2016). Also, completely different post-exercise signal responses can be expected between SM and GM, despite high activation of both in this exercise.

The GM ICs have the general signal shape previously reported in studies of single contractions, but with much broader peak in time. These components could be analyzed in the conventional way, with measures such as peak magnitude and half time-to-peak. However, the form of the *decay* soleus component from most subjects appears unique: it involves a decay with an undulation. This precludes conventional peak based analysis of the signal, though it may be possible to characterize it using the model of blood volume and oxygenation previously described for single contractions by Towse et al. (2011).

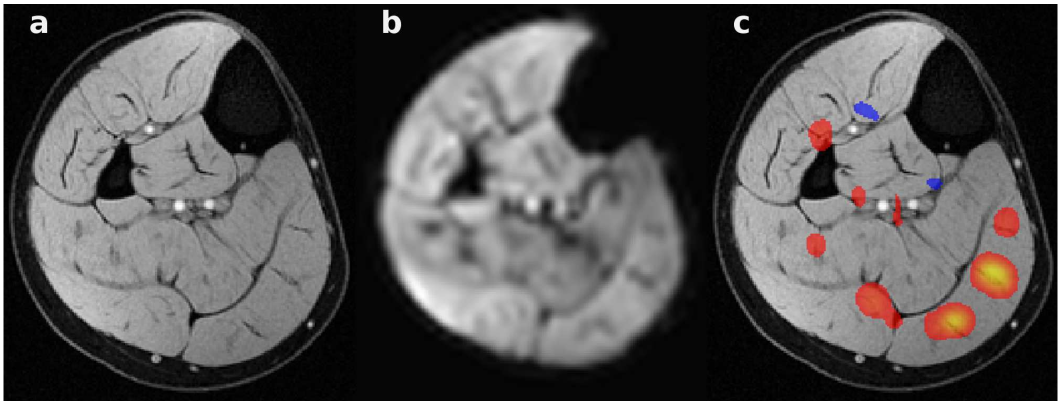

Figure 4.9: Vascular signal extents. Images show the same slice from one trial (*subj03-PE2f_C02*): **(a)** T_1-weighted structural image with fat-saturation; **(b)** mean *post-ex* functional image, after motion correction and registration with with the anatomical, but before smoothing; **(c)** overlay of a thresholded vascular independent component on the structural image. The spatial extent of the venous signal in the medial gastrocnemius is broader than one might expect based on the other two images. Non-linear registration was used to bring the *post-ex* functional images into alignment with the structural one (Klein et al., 2010).

Rest ICA

Figure 4.10 gives examples of typical and atypical ICA results from the *rest* data set. A component similar to the top one was produced in all trials within the first three results, as ordered by unique variance explained. The spatial weights of the component are in the anterior and posterior regions of the leg, and it has a linear temporal trend. Spatially, it does not appear physiological, and has a striped pattern with opposing signs similar to one reported previously by Beckmann and Smith (2004, Fig. 10). The component likely represents an anterior-posterior image ghosting effect, which may have occurred due to hardware effects. Other components typically found were arterial components with a pulsatile time course, and components with sharp transitions that appeared to originate from gross motion.

Based on examining the *rest* data, motion components were identified as having spatial maps with significant clusters primarily at the edges, sometimes appearing to be a vessel near the edge. Components due to vessels were also very prominent, appearing as point sources that sometimes had a surrounding ring with opposite correlation.

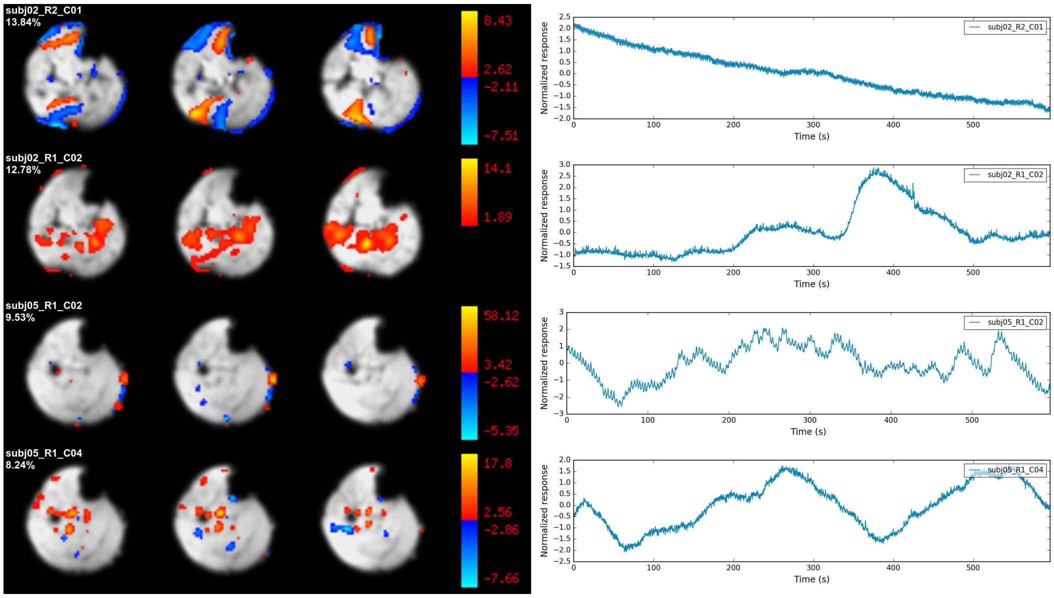

Figure 4.10: Components from rest data. (**a**) Typical component with spatial weights in the anterior and posterior of the leg and linear time course; (**b**) in some trials, soleus-correlated components such as this one were observed; (**c**) vascular component with power around 0.2 Hz; (**d**) saw-tooth component with arterial spatial map and frequency of about 0.003 Hz. Component labels as in Fig. 4.2.

Motion parameters and their regression

Upon close examination across trials and subjects, motion parameters were noted to be highly correlated (Fig. 4.11). The median correlation of motion parameters across trials in rotation, left-right (LR) translation and anterior-posterior (AP) translation were found to be 0.71, 0.73, and 0.47, respectively. Examining the parameter plots visually, it was evident that motion spikes occurred randomly, but that the parameters exhibited long slow trends that were similar across trials.

The correlation of *rest* motion parameters was also examined, after removing initial volumes (Fig. 4.12). In this data the trend in correlations was the opposite. There was very little correlation in rotation and LR translation, with median PCC of 0.03 in both cases. However, AP translation parameters were highly correlated, with median $PCC = 0.78$.

The proportion of variance remaining after motion parameter regression is shown in Figure 4.13. The mean ± SD values of SS_{rel} in GM were 0.09 ± 0.07, and 0.23 ± 0.11 in SM. This indicates that regression with motion parameters removed

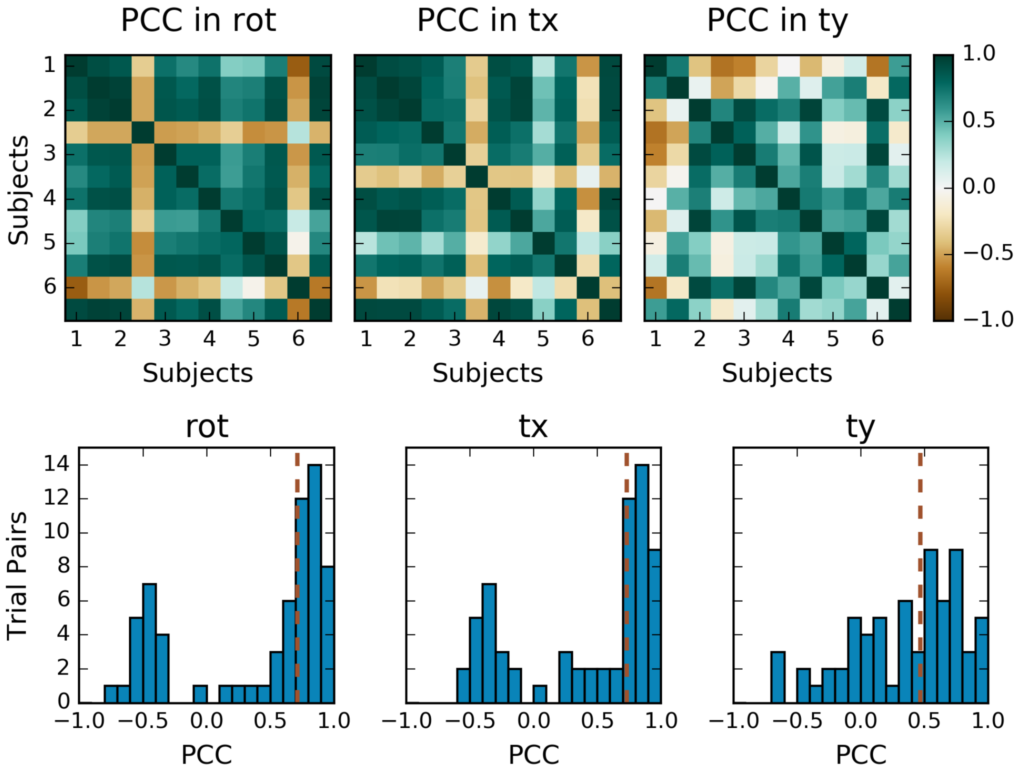

Figure 4.11: Temporal correlation of motion correction parameters in *post-ex* trials. In the matrices, *Subjects* ticks refer to the first trial of a subject, with the second trial adjacent. In the histograms, dotted vertical lines indicate median PCC. Rotation and LR motion parameters were highly correlated across trials (median PCC of 0.71 and 0.73, respectively), with AP showing moderate correlation (0.47). PCC, Pearson's correlation coefficient; *tx*, left-right translation; *ty*, anterior-posterior translation; *rot*, in-plane rotation.

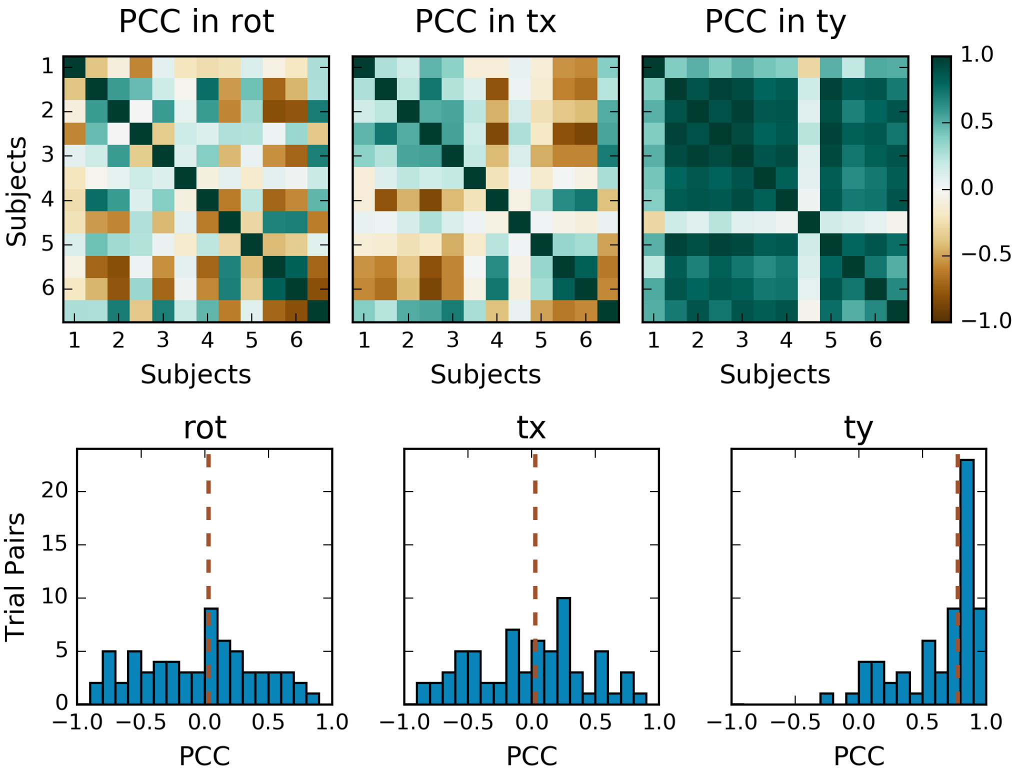

Figure 4.12: Temporal correlation of motion correction parameters in *rest* trials. Rotation and LR motion parameters were uncorrelated (median *PCC* = 0.03 in both), but there was high correlation in AP translation across trials median *PCC* = 0.78. Labels as in Figure 4.11.

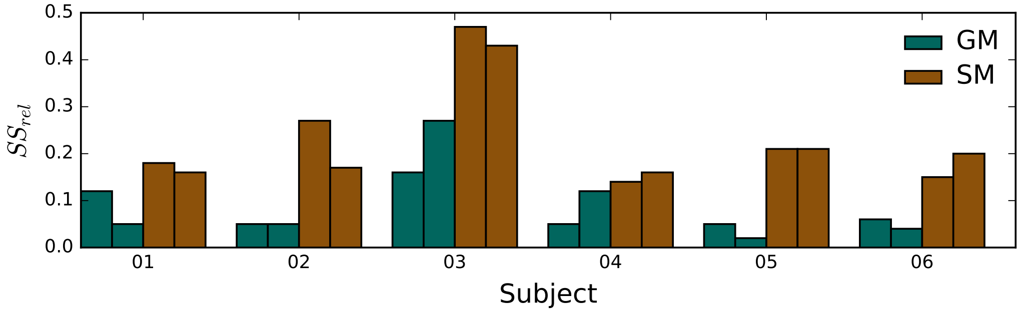

Figure 4.13: Residual variance after motion regression. Relative sum of squares (SS_{rel}) of GRE EPI signal from the gastrocnemius and soleus muscles (GM and SM, respectively). This quantity indicates the proportion of variance remaining in the residual data after regression of motion components in the *post-ex* data for the two trials of each subject.

most of the variance from the signal in these two ROIs. Using this regression technique, a standard way of dealing with motion in brain imaging, would leave very little signal to examine and model in further analysis. Clearly, the validity of using it in the present context should be carefully considered.

Given the large amount of variance removed from the *post-ex* signal by regression of the motion parameters noted in the results, the relationship was further studied in an effort to determine the more likely of several possibilities: (i) motion may have caused the signal change of interest in the PICA results; (ii) a change in image contrast affected the motion correction parameters; (iii) an external element such as a change in background field (B_0) played a role in both effects; (iv) the similar trends are unrelated, their correlation is just a coincidence.

Contrast Modifications

Efforts were made to determine whether changes in image signal and contrast were affecting motion correction parameters. The images of Figure 4.14 demonstrate two of the image transformations generated to try to confirm the motion correction parameters. None of the image transformations or registration variants appreciably changed the motion correction parameters, indicating that the identified motion did not come from a change in contrast.

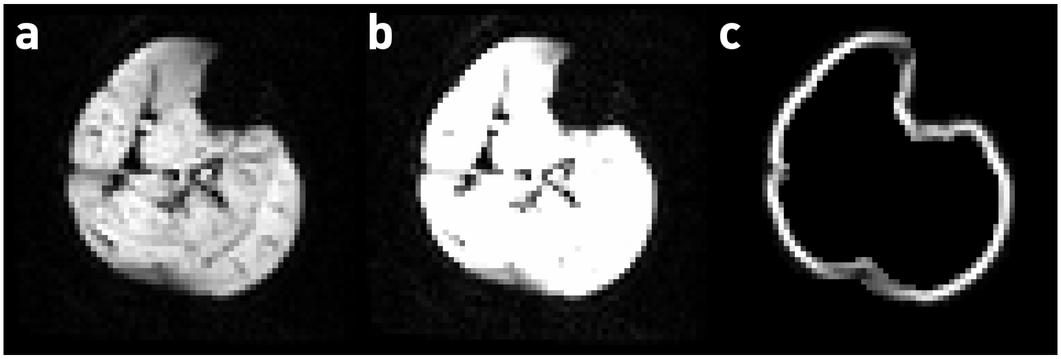

Figure 4.14: Transformed images for contrast modification. Examples: **(a)** original image; **(b)** upper histogram compressed; **(c)** high pass filtering (Scharr) with masking of central region and background.

Peak magnitude and timing analysis

The question of how much signal change may have arisen from gross motion was considered. Figure 4.15 contains the *MCD* and *NTRg* results. The correlation of the *MCD* and *NTRg* was 0.57 at *rest* and 0.04 in *post-ex* data. This indicates that in *post-ex* data, increased motion parameter magnitudes did not appreciably increase the signal fluctuations in GM. This implies that the GM components originated from a physiological source rather than motion. The sharp anatomical boundary of the GM components also supports this notion.

Nevertheless, the typical temporal shape for motion parameters and GM ICs were qualitatively similar. Both often had a peak early in the time course with a long decrease for the remainder of the scan. This similarity lead to the low variance remaining in the GM signal after regressing motion components. For quantitative comparison between the motion correction parameters and the component most correlated to GM, the peak time was recorded from the plots of both data series (Figure 4.16). The mean ± SD peak times for GM ICs and motion correction parameters were 70 ± 20 and 130 ± 80, respectively, with the motion parameters almost always peaking later than the GM signal. This was a significant difference ($p = 0.03$, 2-tailed independent t-test). This indicates that although the shapes were similar between the motion correction parameters and the GRE EPI signal, the motion did not appear to cause the signal changes.

Next, a trial was sought that had significant motion, but very little physiological contribution to the signal. The *rest* trial *subj04_rest1* was identified as one with

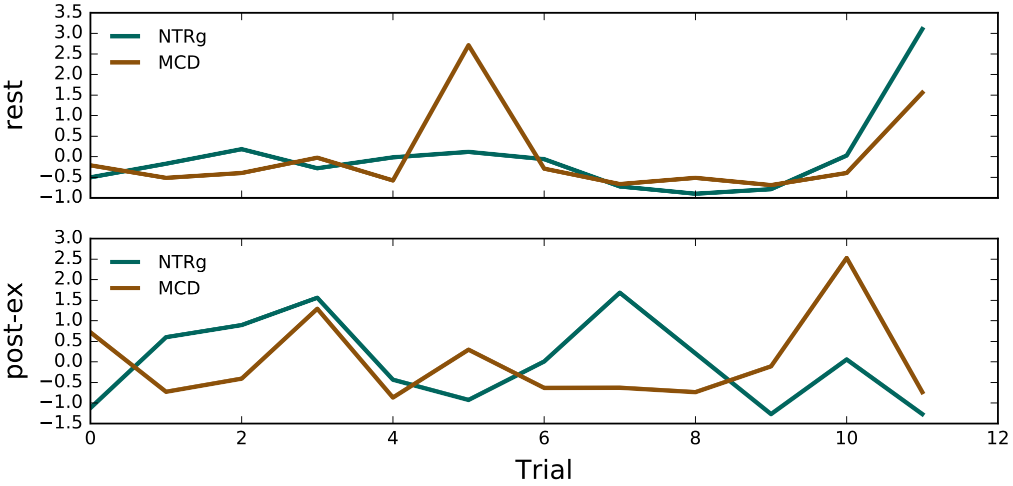

Figure 4.15: Signal and motion parameter ranges. Comparison of *NTRg* (mean normalized temporal range of signal in the gastrocnemius ROI) and *MCD* (maximum range of motion correction parameters converted to displacement units) in the *rest* and *post-ex* conditions. All data was mean-centred and variance normalized before plotting. Trials were plotted sequentially from trial 01 of *subj01* to trial 02 of *subj06*. The correlation of the curves was 0.57 for *rest* and 0.04 for *post-ex* data.

gradual, relatively large magnitude motion similar to that observed in most *post-ex* trials. The components that appeared correlated with motion were 4, 5, and 12 (components can be viewed in Section 4A.4). In this trial, component 1 was a long term temporal trend (linear decrease) in the tibialis anterior, while 2 and 3 were pulsatile components focused on the arteries. This means the first motion component produced less variance than the pulsatile ones for this significant but gradual motion. In *post-ex* trials, the pulsatile components contributed far less to the total variance than the GM components, providing more evidence that motion did not cause the GM components.

Overall, motion effects were evident in the signal through specific components produced by ICA. However, clearly aspects of the signal were unrelated to motion, since they survived even the aggressive 24 parameter detrending procedure. The GM and SM components of interest cannot be directly selected by band-pass filtering, as is commonly done for model-free analysis of resting state fMRI in the brain. This is because the slow motion trend has similar spectral characteristics

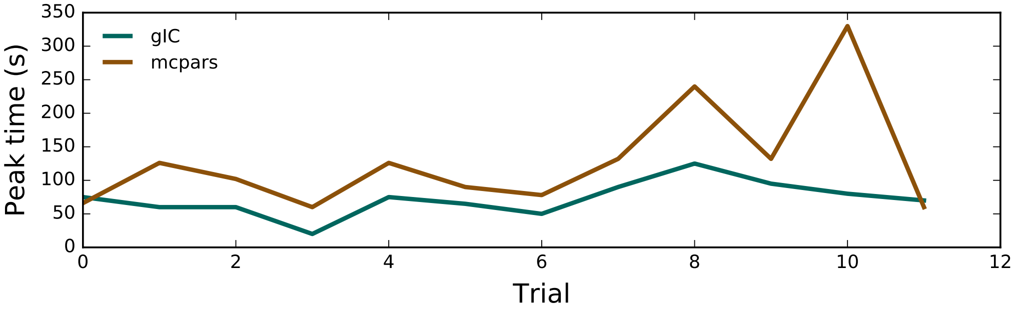

Figure 4.16: Motion parameter and gastrocnemius component peak times. Two peak times are plotted from each trial (two *post-ex* trials each from six subjects). Peak times were determined from visual examination of the curves: (i) *gIC*, the independent component most correlated with gastrocnemius ROI (see Fig. 4.4); (ii) *mcpars*, the motion correction parameters. The motion parameters almost always peaked later than the signal.

to the components of interest. The main variation in these GM and SM ICA components occurred over several minutes, which was similar to the timing of blood volume and oxygenation changes in a similar exercise study using near-infrared spectroscopy (NIRS) (Torricelli et al., 2004). Further, the technique of regressing motion parameters from the data assumes that motion correction has been completely accurate. For these reasons, BSS methods of analysis such as PICA are recommended for use in future studies, rather than a combination of motion parameter regression and peak analysis, or simply ignoring the likely possibility that some of the signal originates from motion.

Possible causes of the correlation

To summarize, multiple pieces of evidence indicate that motion parameters and the GRE EPI ICA components of interest are unrelated, despite their correlation and the qualitative similarity of their shape. The reason for the similarity of the two time courses is unknown, though the authors present the following suggestions:

- The apparent motion could be caused by varying signal in the superficial vasculature of the lower leg, changing the partial volume signal from the marginal voxels in a time varying manner. However, no such source component was observed from ICA, so this doesn't seem to be the case – the component that would match the motion parameters most closely, the gastrocnemius component, seems to specifically exclude voxels at the margin.

- The massive influx of blood, in particular paramagnetic HHb in the exercised muscle, caused a change in B_0 that induced an image distortion in the EPI images. The veracity of this idea is difficult to assess with the information at hand. It can be noted, however, that no peaks in the post-exercise physiological signals were observed in the aforementioned NIRS study (Torricelli et al., 2004). The only way to ascertain whether this is a significant contribution to the results would be to run a different experiment in which a time series of field maps were acquired under the same experimental conditions.
- Mechanical changes may have caused motion while the muscle and tendon complexes relaxed after the stresses of the intense exercise. The best way to verify this would likely be using ultrasound to record a time series of images for several minutes following exercise in a similar study to this one.

4.4 Conclusions

The analysis presented in this paper represents an exploratory investigation of the post-exercise muscle BOLD signal. One of the challenges of doing muscle imaging of this type is that the signals of interest are low-frequency, in the same range as scanner drift and slow motion effects. Motion may have played a part in generating the signal changes seen here, but was not the primary source of variance. In the components produced from this study, several aspects bear further consideration, such as the source of difference between the gastrocnemius and soleus components in most subjects, and the *two-crest* components that originated from the deep veins of the triceps surae.

In this study, a preprocessing work flow was developed for the PICA multivariate analysis strategy. This method produces consistent components from subjects, and represents a mechanism for defining functionally related regions of muscle tissue following exercise. The clusters and their time courses may be further studied to look for differences in the response among subject populations or apply physiological models.

To a large extent, the results of this study validate the practice of selecting ROIs in muscles and taking them to be representative of the total muscle response. Of note, however, is that draining veins within the muscle can disrupt the signal in a broad region surrounding them. Particular care must be taken to avoid these areas when selecting ROIs, especially because they are difficult to identify from T_1-weighted structural images.

4A Appendix

4A.1 PICA preprocessing

Before settling on PICA, other multivariate analysis strategies were attempted. Initial investigations examined PCA alone and with various rotation methods, as well as factor analysis. ICA was also attempted, but components were difficult to interpret due to overfitting of a large number of components. Finally, PICA was used, in the form of FSL's *Melodic* tool. Various preprocessing steps were investigated and optimized, some of which made a large difference in the components returned. Considerations that may be of interest to the reader:

- **Spatial smoothing.** This was found to significantly impact the thresholded ICA weight maps, and substantially reduced the number of components returned (from >200 to ~15). Spatial smoothing seemed to reduce the number of temporally correlated components returned, combining them into a single component. Smoothing was applied in-plane only, due to the limited through-plane FOV and thick slices.

- **Temporal filtering.** Low-pass filtering with decimation was found to have significant impact on the number of components: the more filtering applied, the fewer components returned by PICA. It removed cardiac components and simplified the temporal appearance of remaining components. This was not applied, as it was not known whether high frequency components would be of interest. High-pass filtering, as recommended in the melodic technical report (Beckmann and Smith, 2004), was not carried out, as the signals of interest in muscle were thought to be at low frequencies. This comes at the cost of increasing the rank of the mixing matrix (i.e. the estimate of the number of components).

- **Masking.** This was applied to remove background. Using a conservative mask, not including partial volume voxels at the edges of the leg, was found to reduce the number of PICA components by about one third. A more liberal mask was used, to ensure edge effects were apparent from gross motion.
- **Slice timing correction**. This was not found to significantly impact components. It was applied to the data based on the idea that it should do no harm.
- **Normalization**. This was considered in this study but not performed, as registration among subjects is problematic. Non-linear registration with particularly tuned parameters would be required.
- **Number of components**. When the number was manually chosen, it had a dramatic effect on the outcome. With a large number, components seemed to *split*, with many components returned that had high temporal correlation. This also made interpretation difficult. With too few components, the data space was reduced, and components accounted for less of the overall variance, while also losing components of possible interest.

4A.2 Signal variance

As discussed in Section 4.2, the imaging data was mean-centred and variance normalized in preprocessing before ICA components were generated. Thus, information on the spatial distribution of variance in the signal cannot be inferred from the ICA results. This information is potentially useful as an indicator, since one would expect much larger changes in BOLD signal in areas of working muscle than in less active muscle, assuming the signal measures physiological changes and not motion. Indeed, the variance results from Subject 5 (Fig. 4.17) indicate large variance in the gastrocnemius muscles and lateral compartment, as well as localized variance in the soleus. The anterior and posterior tibial muscles exhibit very little variance by comparison. This figure is consistent with a map of physiological changes following exercise, whereas in a map of motion one would expect the highest variance to be at the tissue boundaries with air and bone.

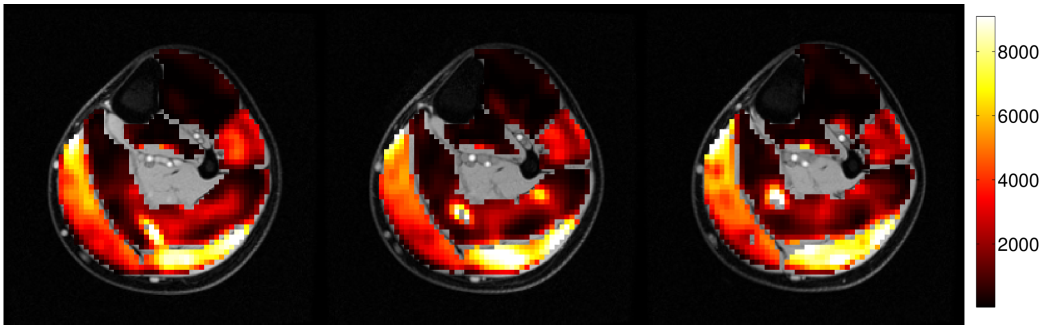

Figure 4.17: Variance of *post-ex* signal. The colour represents the variance associated with the *post-ex* signal from three slices of one subject (Subject 5). The highest variance occurs in the gastrocnemius and near vessels that were only partially excluded from the ROIs. Muscles not involved in plantar flexion exhibit the lowest variance.

4A.3 PCA results

Sample results from PCA analysis of *post-ex* data are shown in Figure 4.18. The components demonstrate that PCA was somewhat successful at extracting components of interest in this trial. The lower two components, numbers 7 and 9, especially demonstrate spatial weight maps that can be interpreted anatomically. However, the upper plot of component 3 demonstrates an inherent weakness of PCA that was outlined in Section 1.6: the component is a mixture of cardiac pulsatility and a signal that may be of more interest. PCA has combined two signals into a single component, whereas having two separate maps would be of greater value.

4A.4 Subject level component results

Table 4.5 lists the components that were regressed from the data after the first ICA run, as well as the components identified as having a *two-crest* temporal shape.

The following section details all independent components from the runs of 15 components from every subject. Percentage values on figures are the percent uniquely explained by the component of the total explained variance.

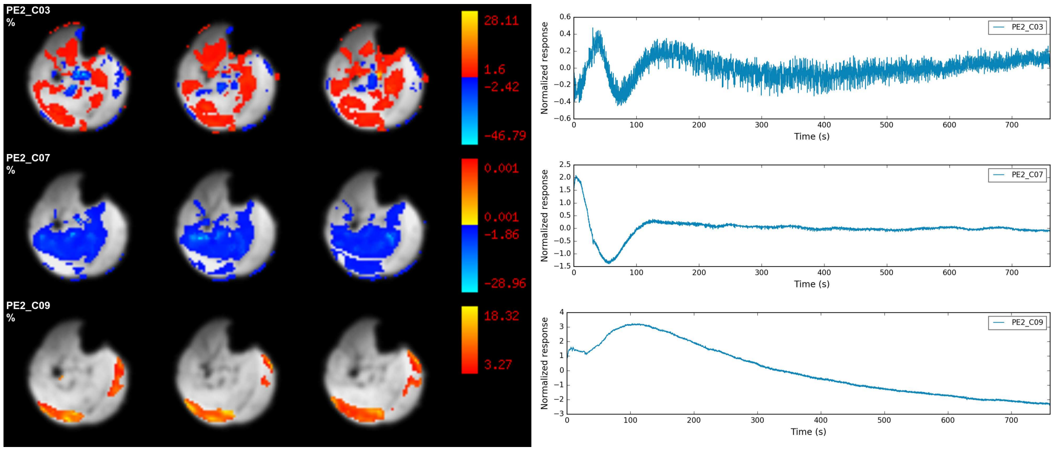

Figure 4.18: Example PCA results. Depicted are three components from PCA analysis of *post-ex* data from a single trial. The upper component, number 3, is a mixture of cardiac pulsatility and an unknown lower frequency signal. The lower components are more coherent in their temporal and spatial structure.

	Regressed	Two-crest
subj01_PE1	1,2,8	1,3,4
subj01_PE2	8,9	2,3,4,12
subj02_PE1	15	3,5
subj02_PE2	11,13,14,15	
subj03_PE1	9	2
subj03_PE2	1,7,10,13,14	2,9
subj04_PE1	3	5
subj04_PE2	10	7,9
subj05_PE1	10,11	5
subj05_PE2	2,3	9,10
subj06_PE1	14	3
subj06_PE2	2	3,11

Table 4.5: ICA component numbers: regressed, two-crest. Ranked component numbers of signals regressed after the first ICA run and visually identified *two-crest* type components. Regressed component numbers refer to pre-filtered data in the following figures, while *two-crest* components refer to filtered data.

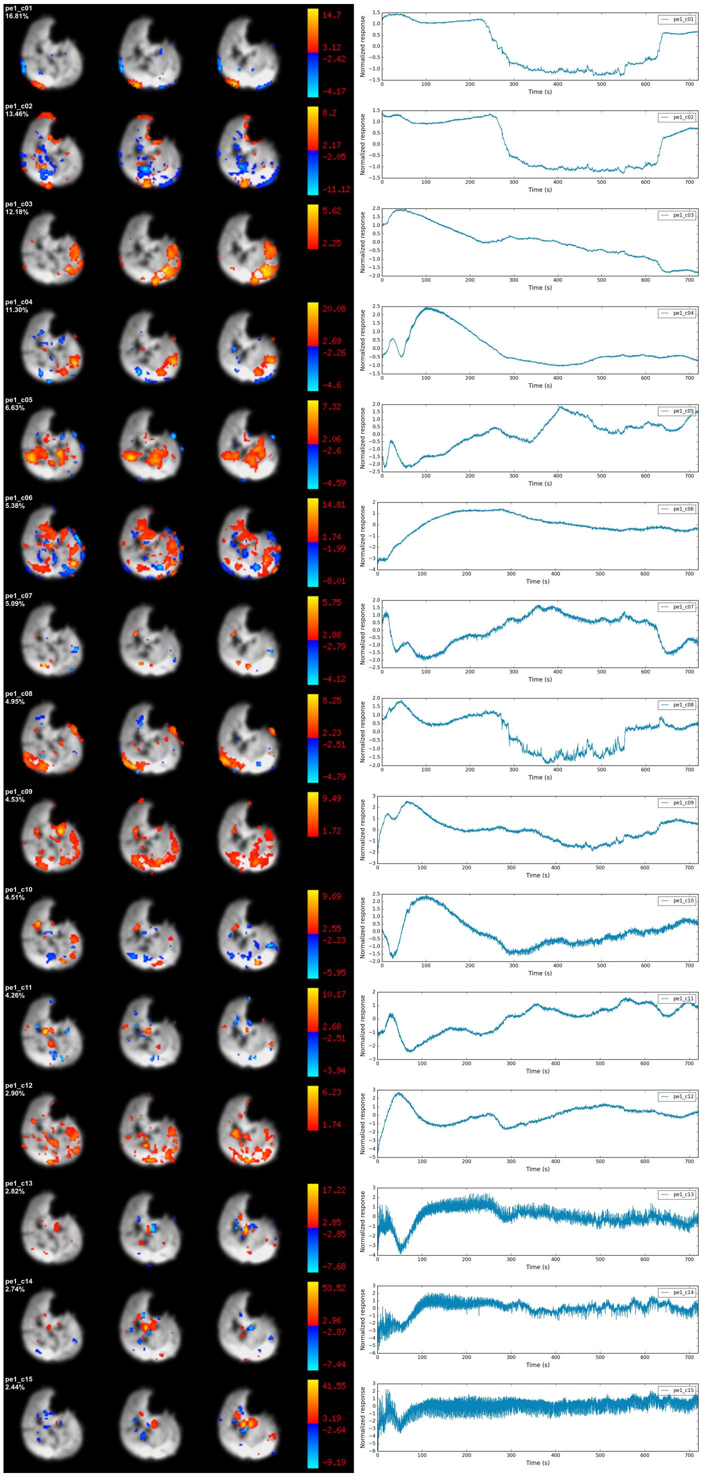

Figure 4.19: Trial *subj01_PE1*

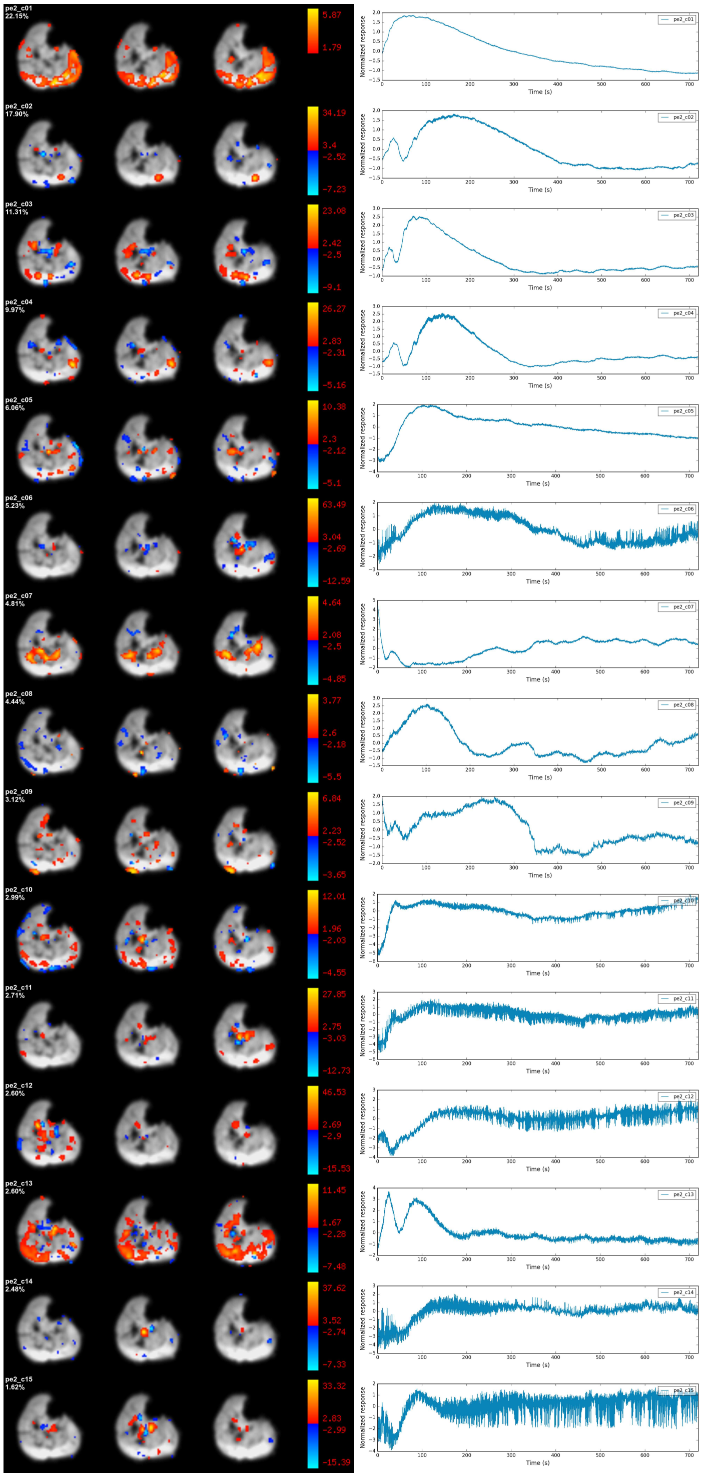

Figure 4.20: Trial *subj01_PE2*

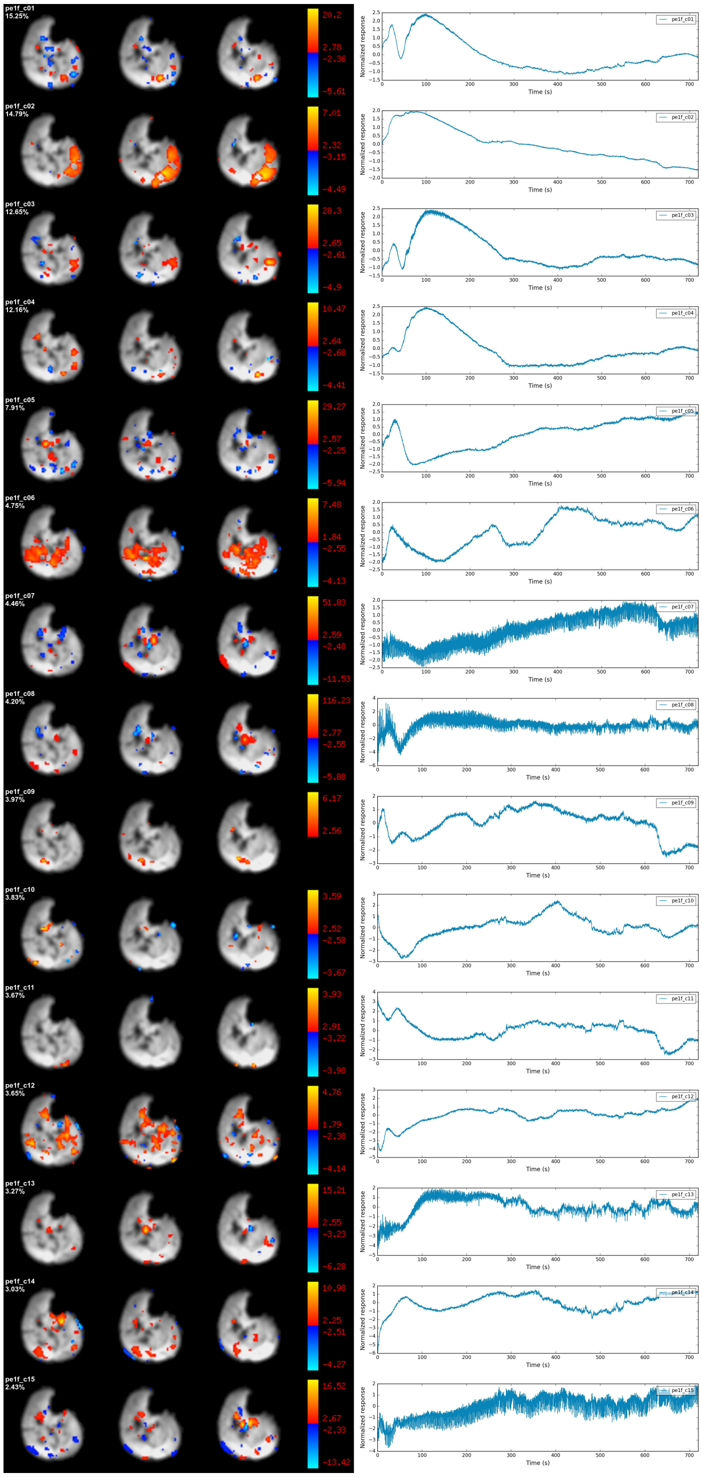

Figure 4.21: Trial *subj01_PE1* filtered, retaining 97.4% of variance

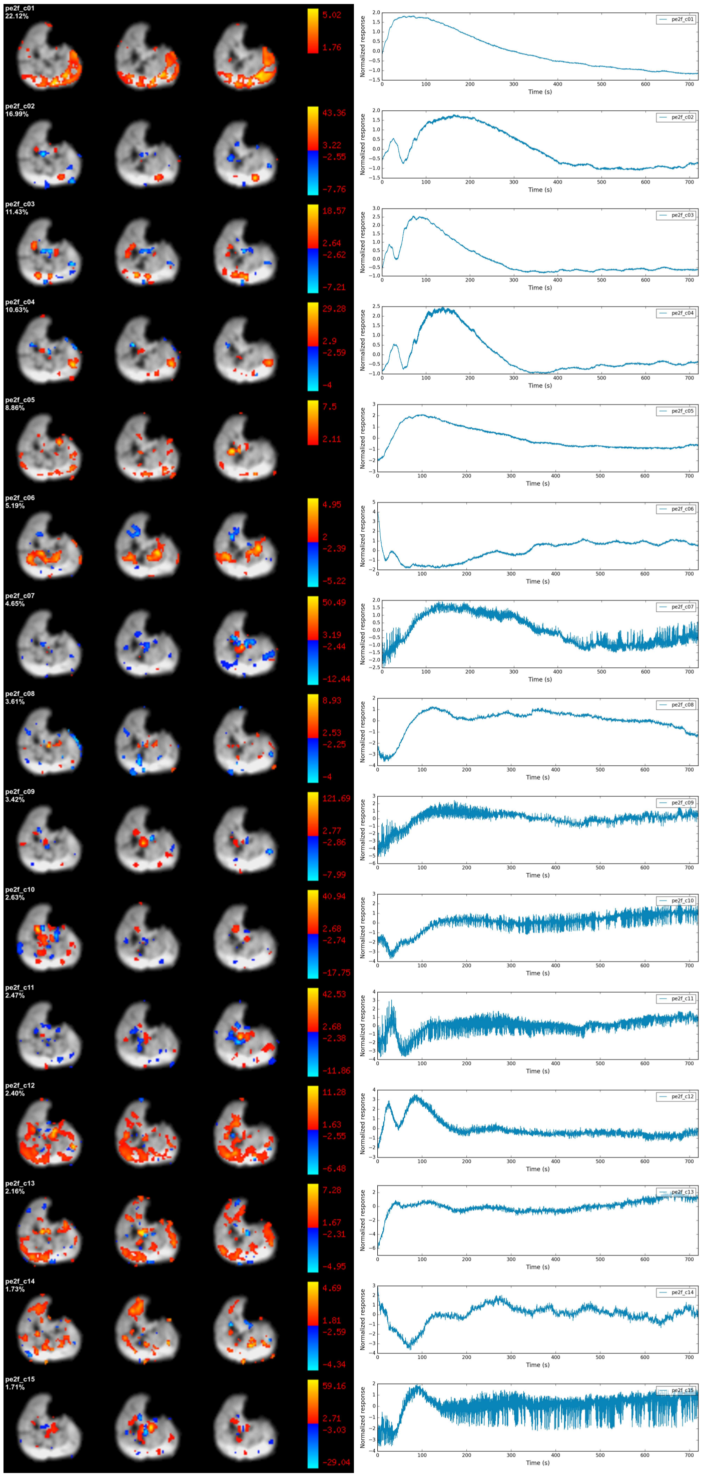

Figure 4.22: Trial *subj01_PE2* filtered, retaining 98.4% of variance

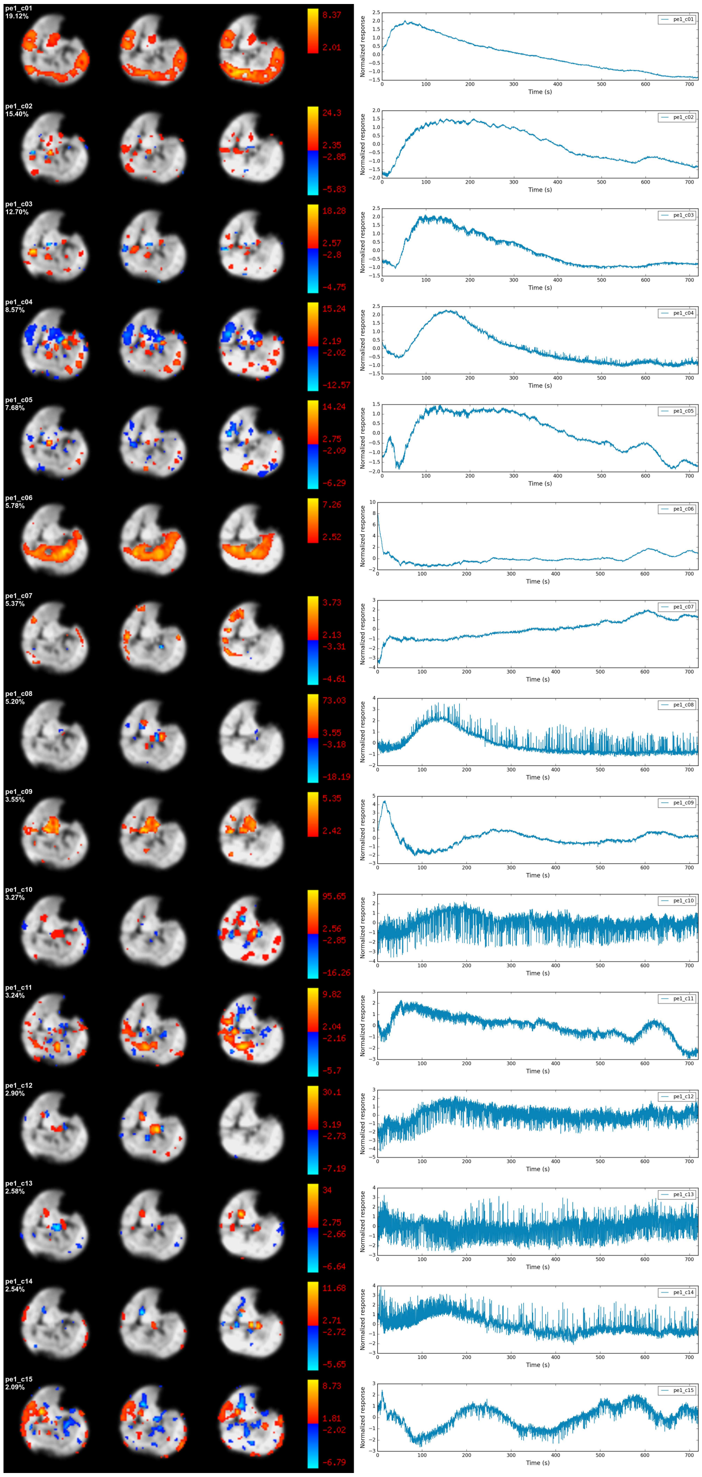

Figure 4.23: Trial *subj02_PE1*

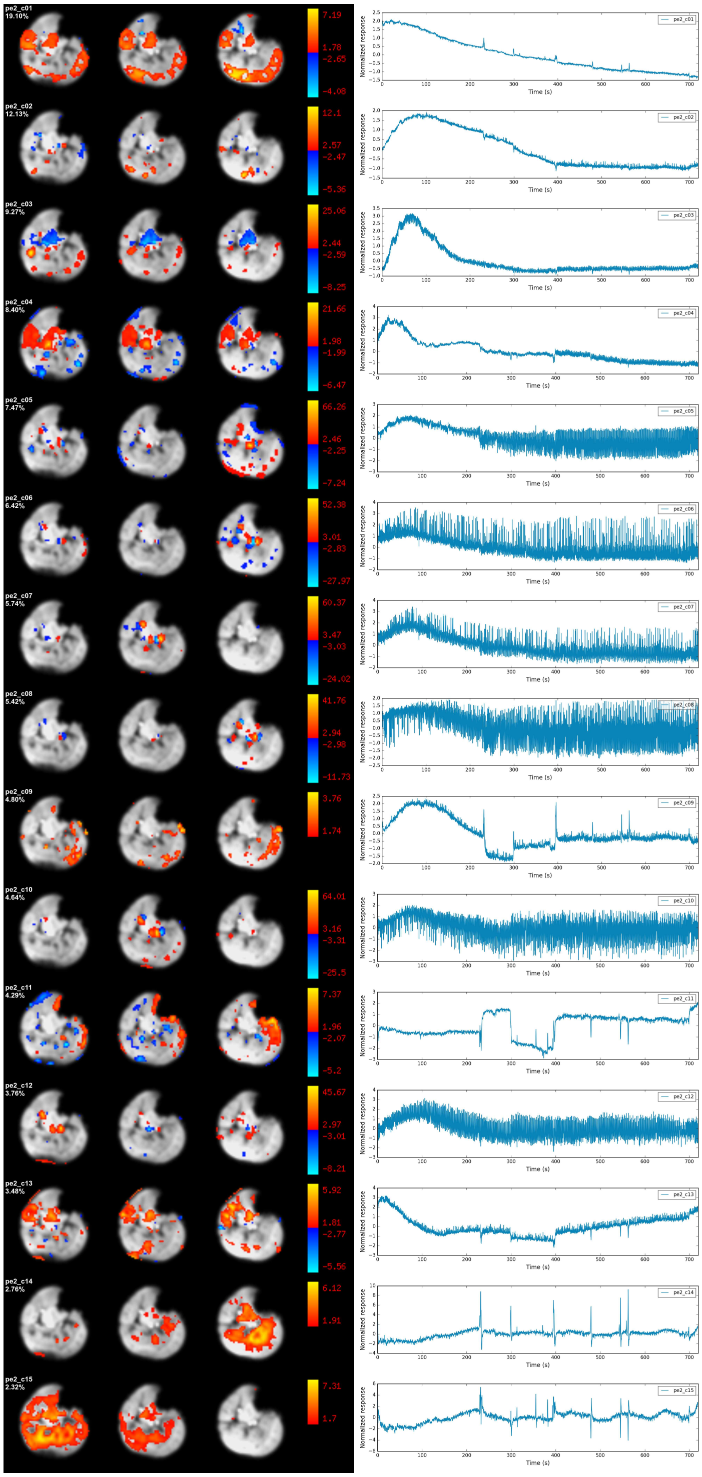

Figure 4.24: Trial *subj02_PE2*

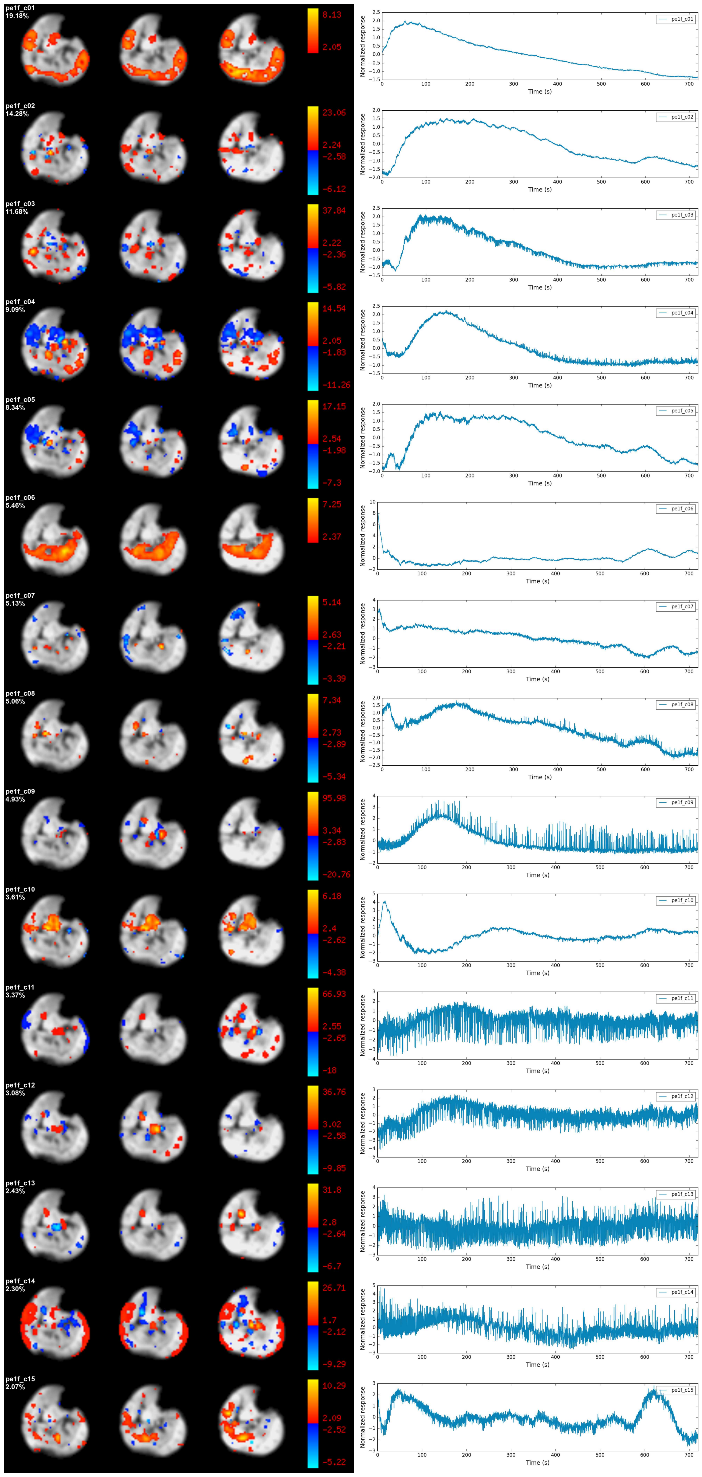

Figure 4.25: Trial *subj02_PE1* filtered, retaining 97.4% of variance

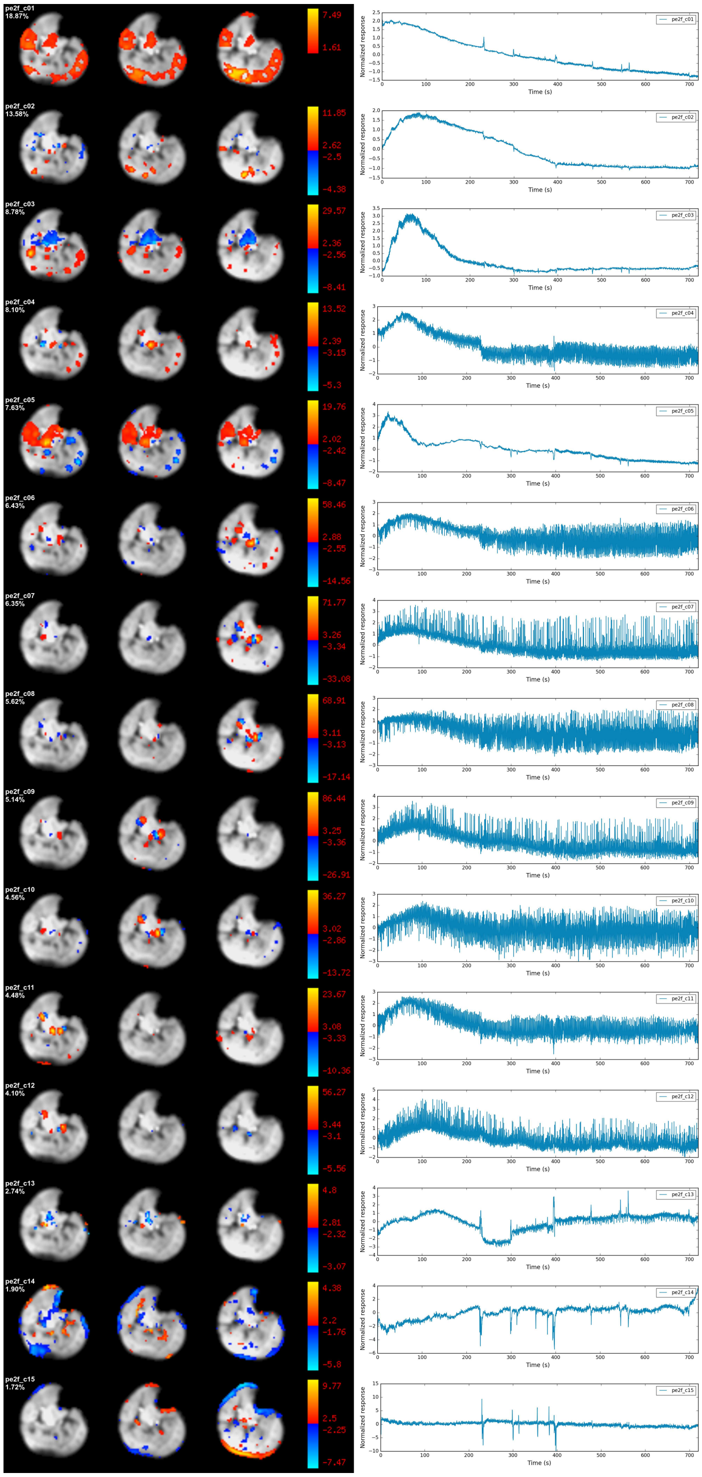

Figure 4.26: Trial *subj02_PE2* filtered, retaining 98.4% of variance

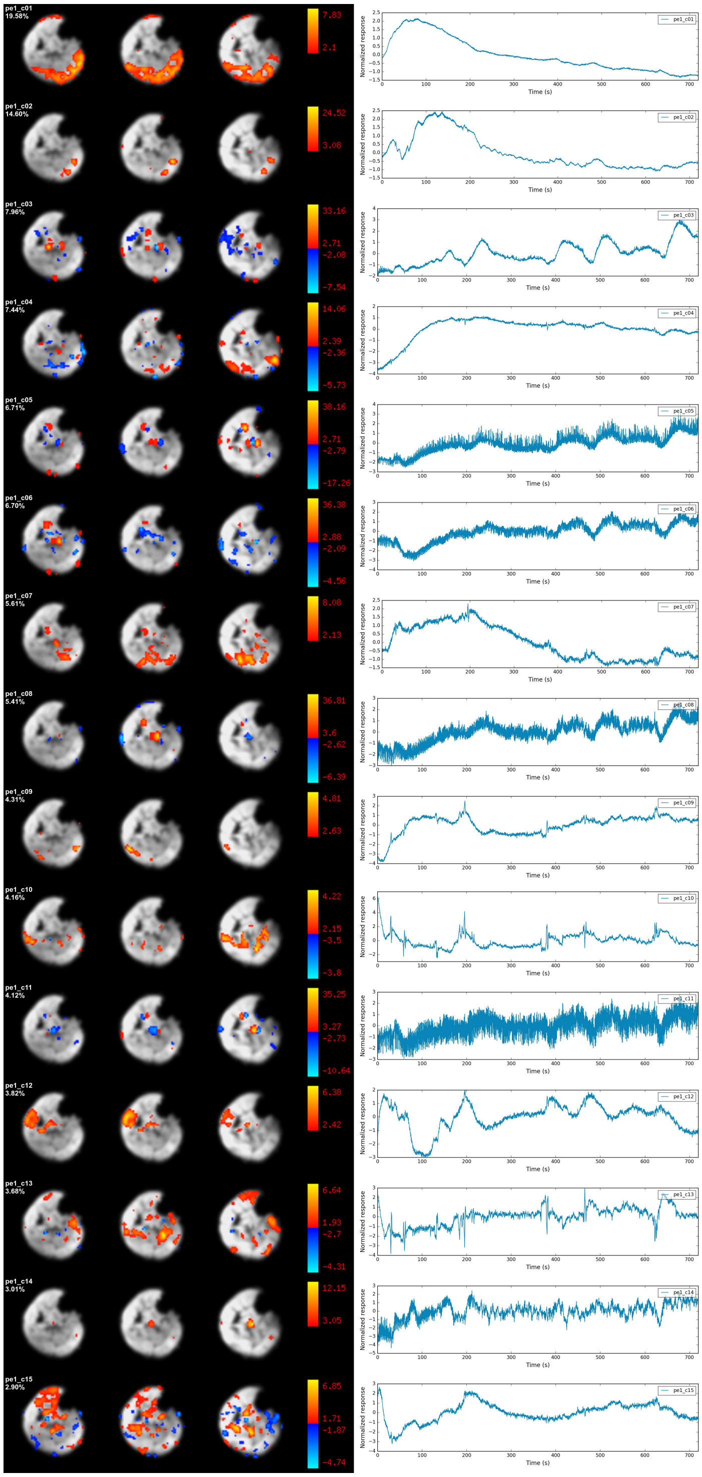

Figure 4.27: Trial *subj03_PE1*

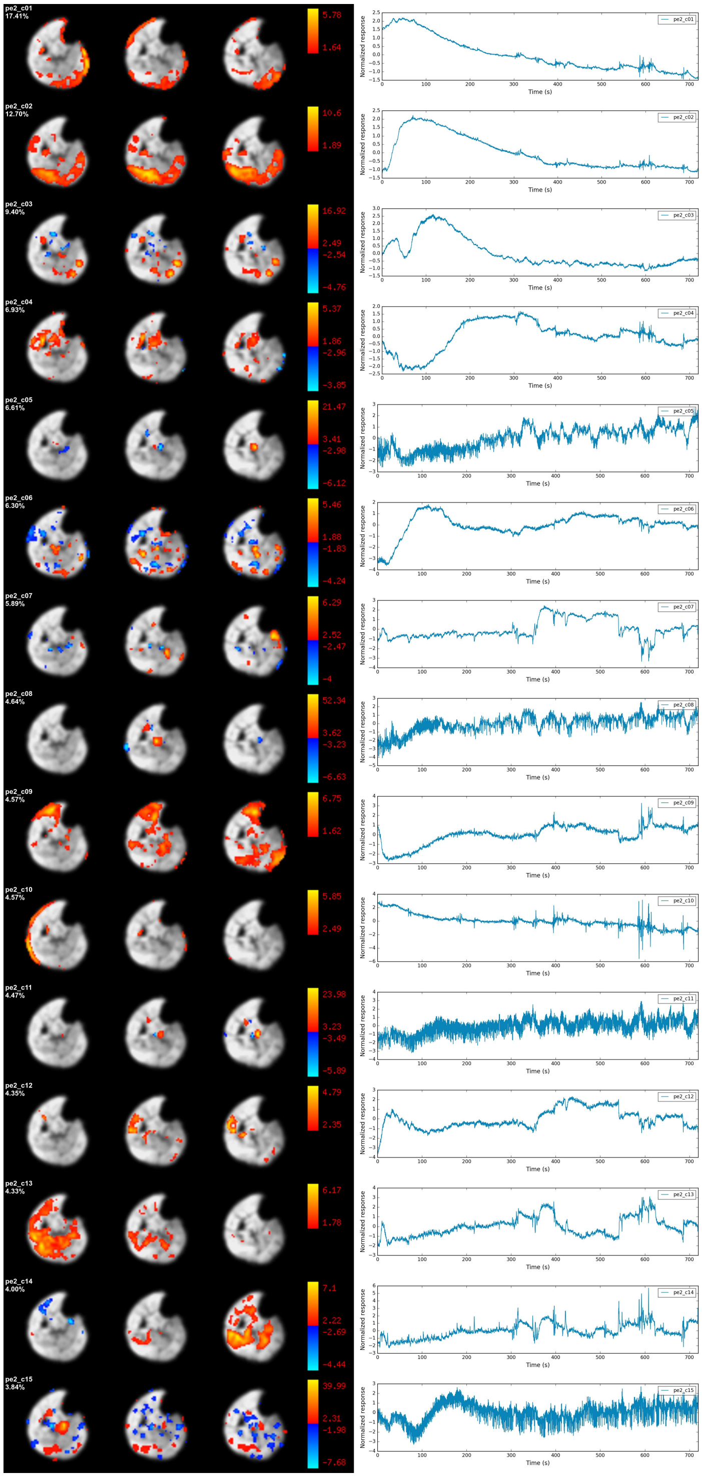

Figure 4.28: Trial *subj03_PE2*

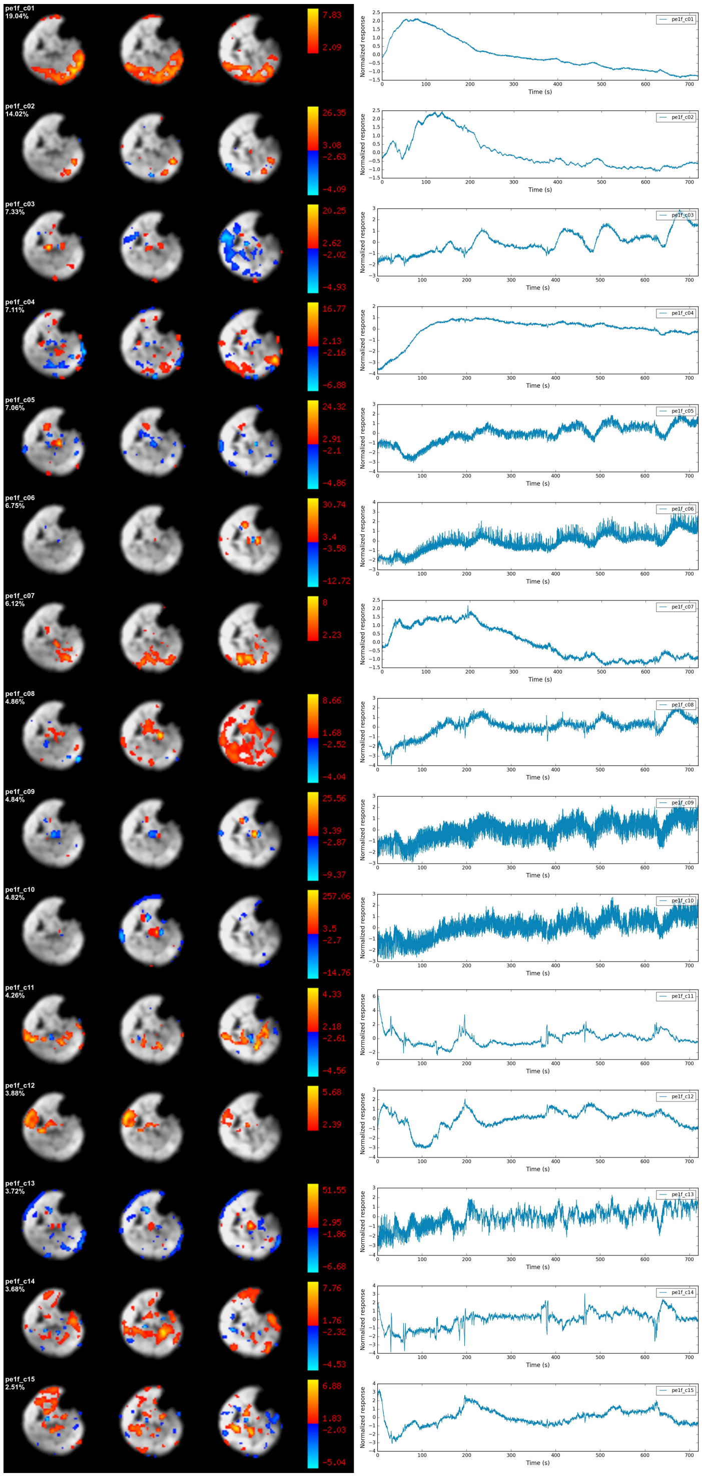

Figure 4.29: Trial *subj03_PE1* filtered, retaining 97.4% of variance

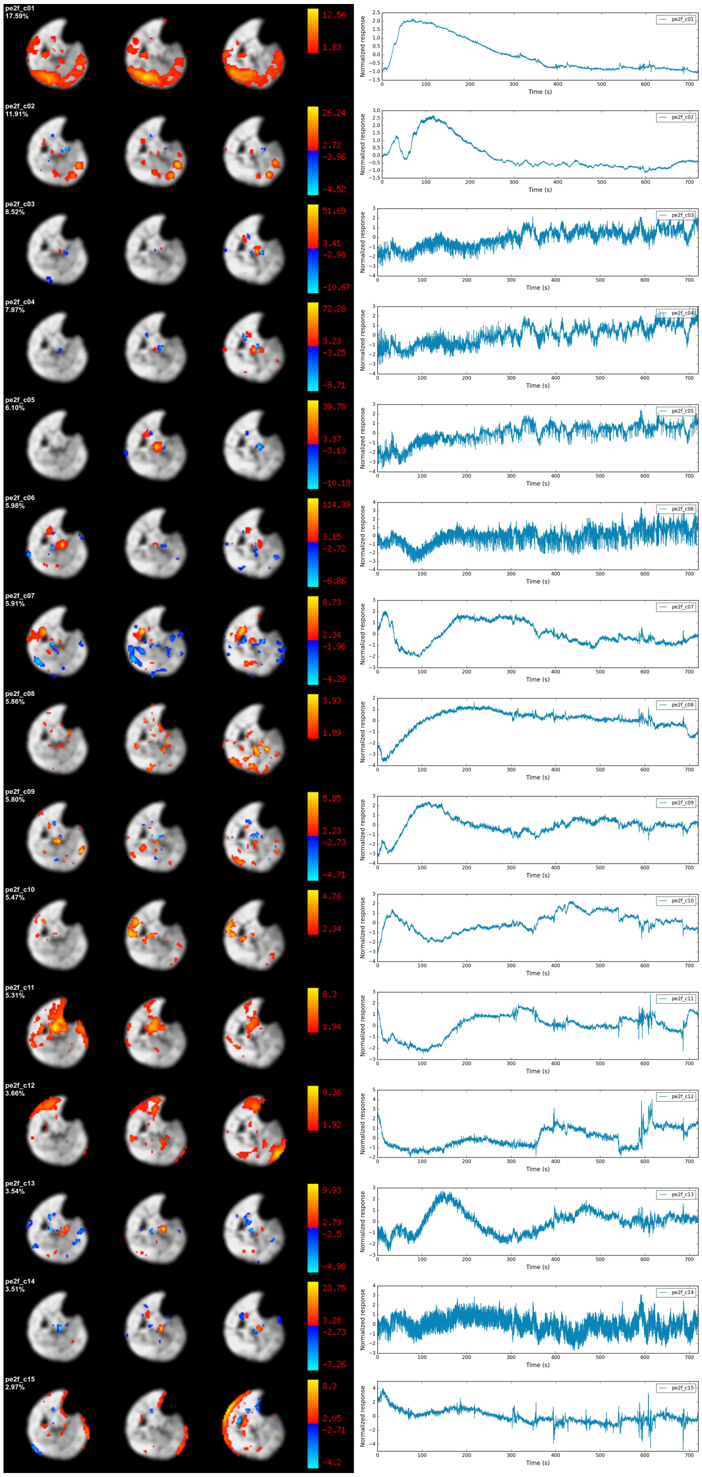

Figure 4.30: Trial *subj03_PE2* filtered, retaining 98.4% of variance

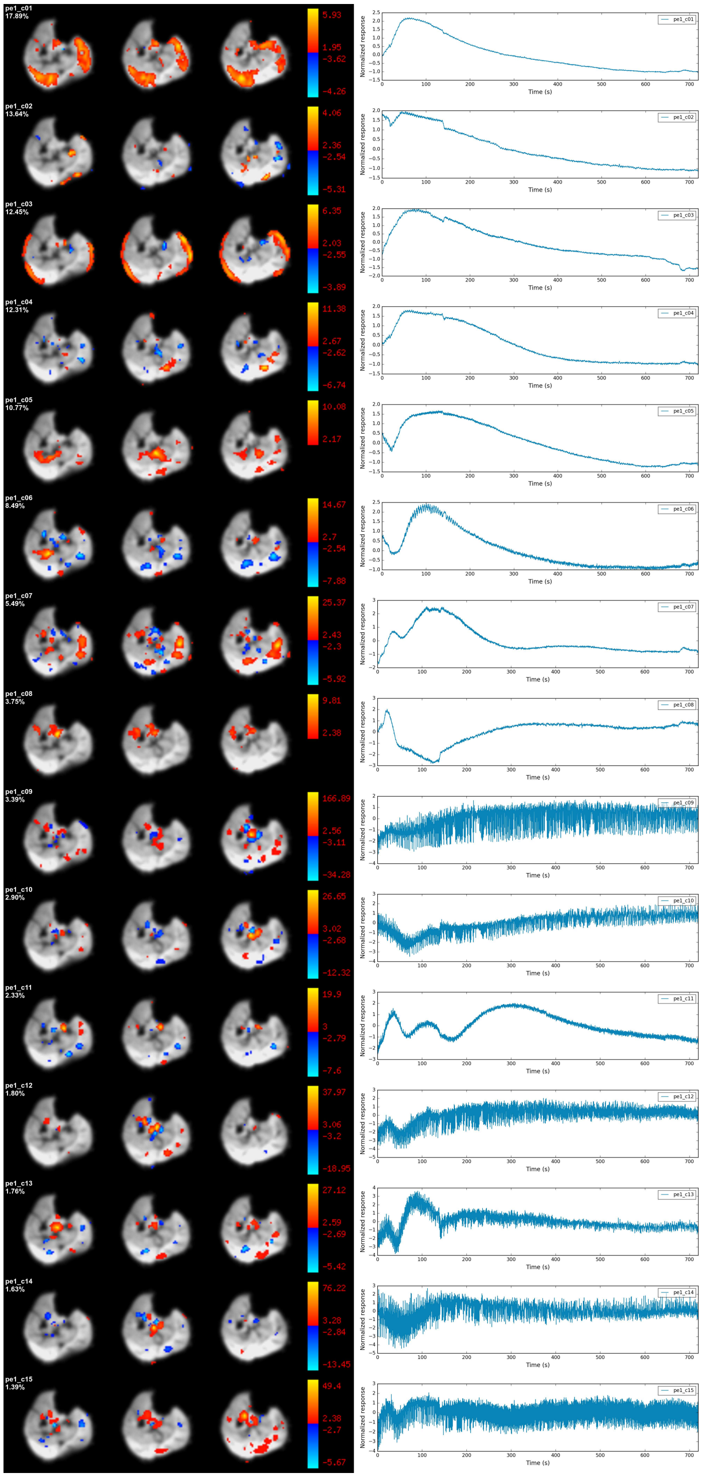

Figure 4.31: Trial *subj04_PE1*

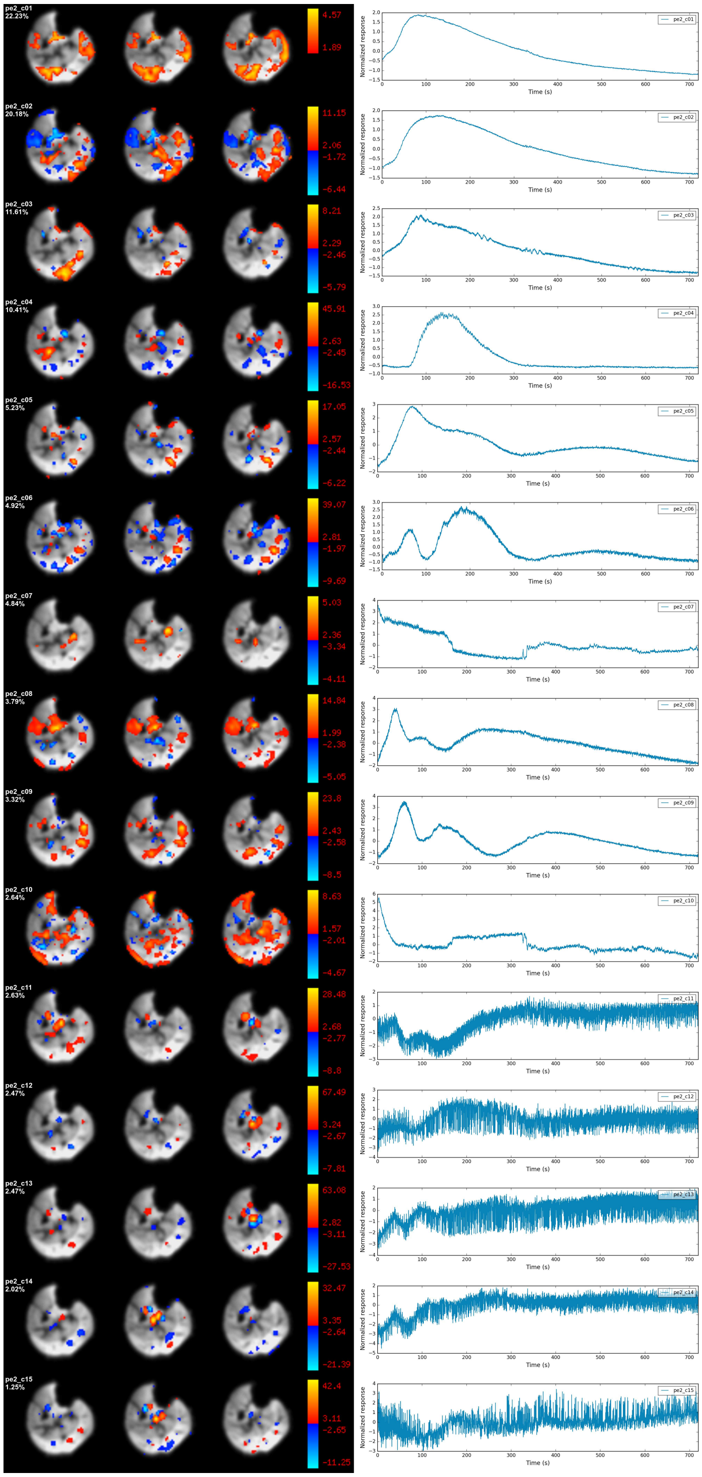

Figure 4.32: Trial *subj04_PE2*

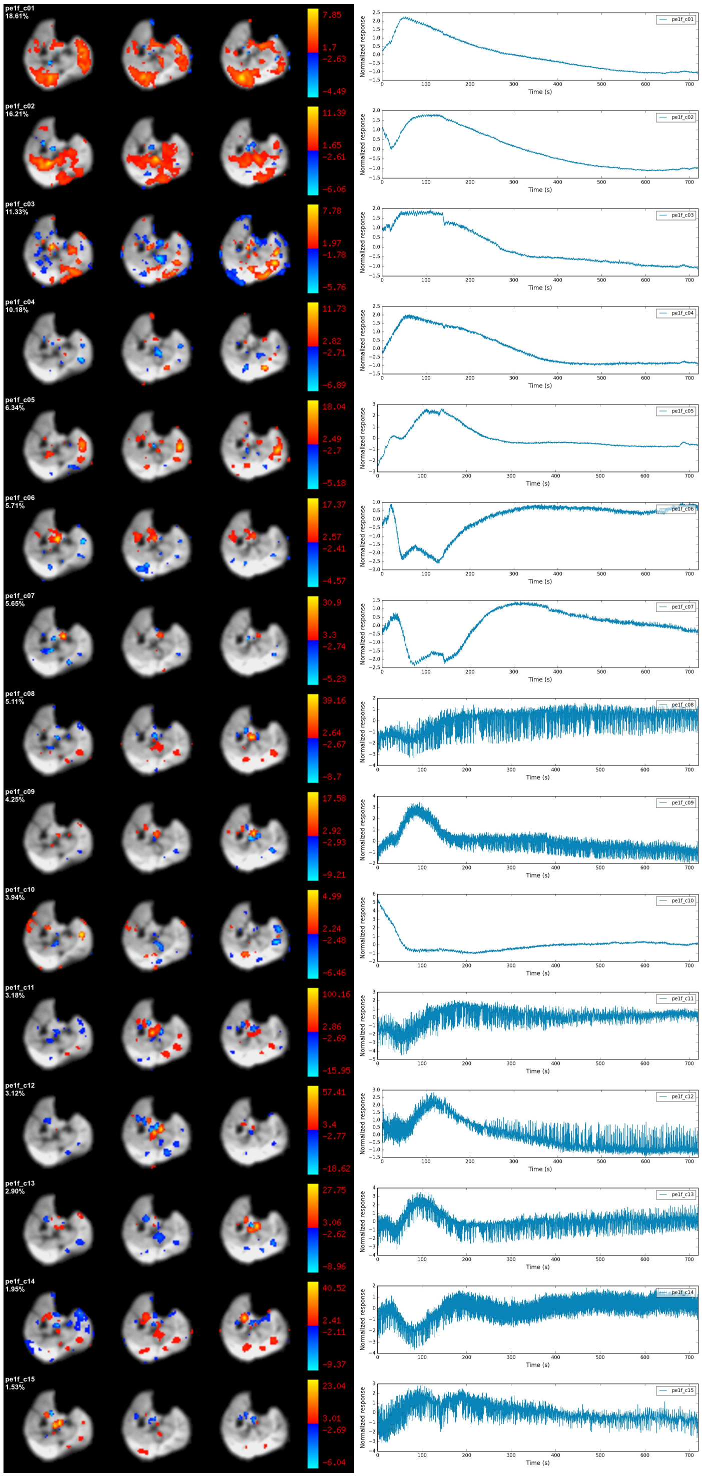

Figure 4.33: Trial *subj04_PE1* filtered, retaining 97.4% of variance

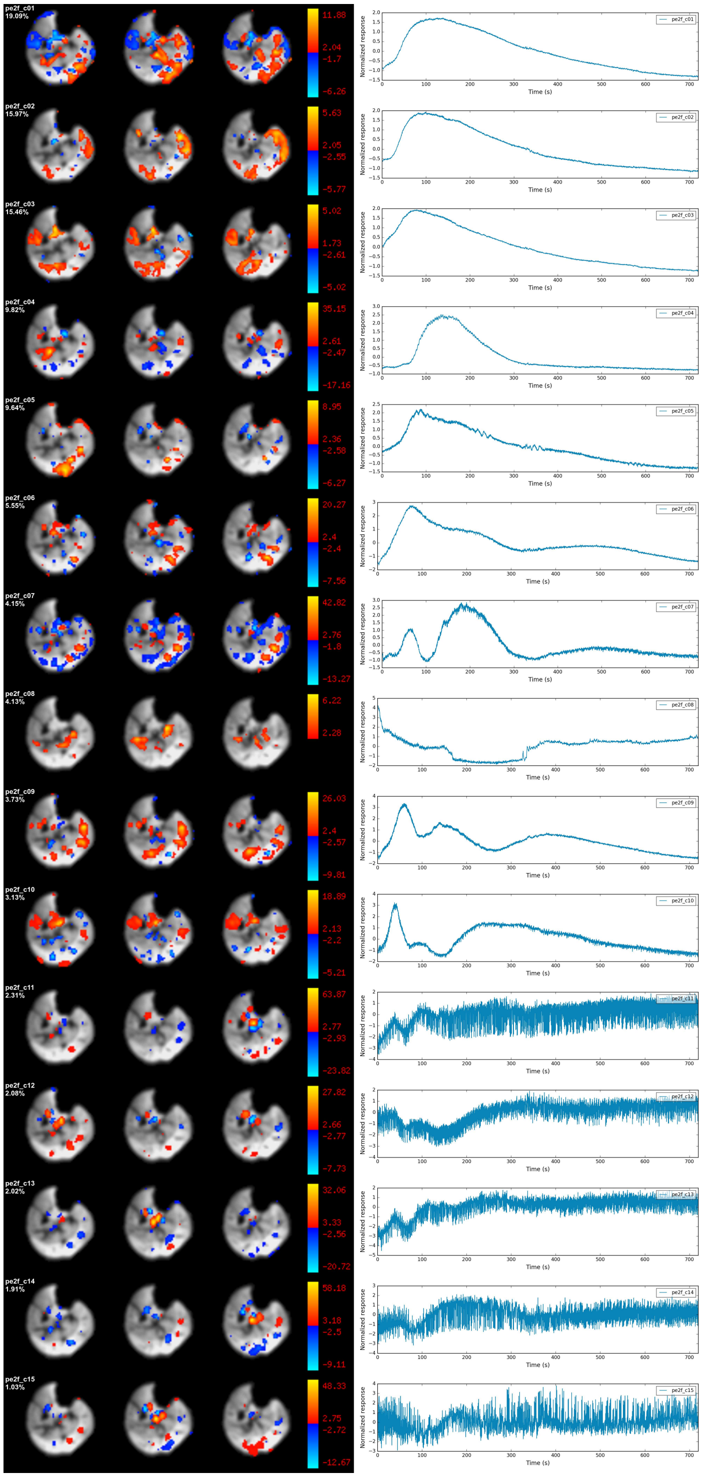

Figure 4.34: Trial *subj04_PE2* filtered, retaining 98.4% of variance

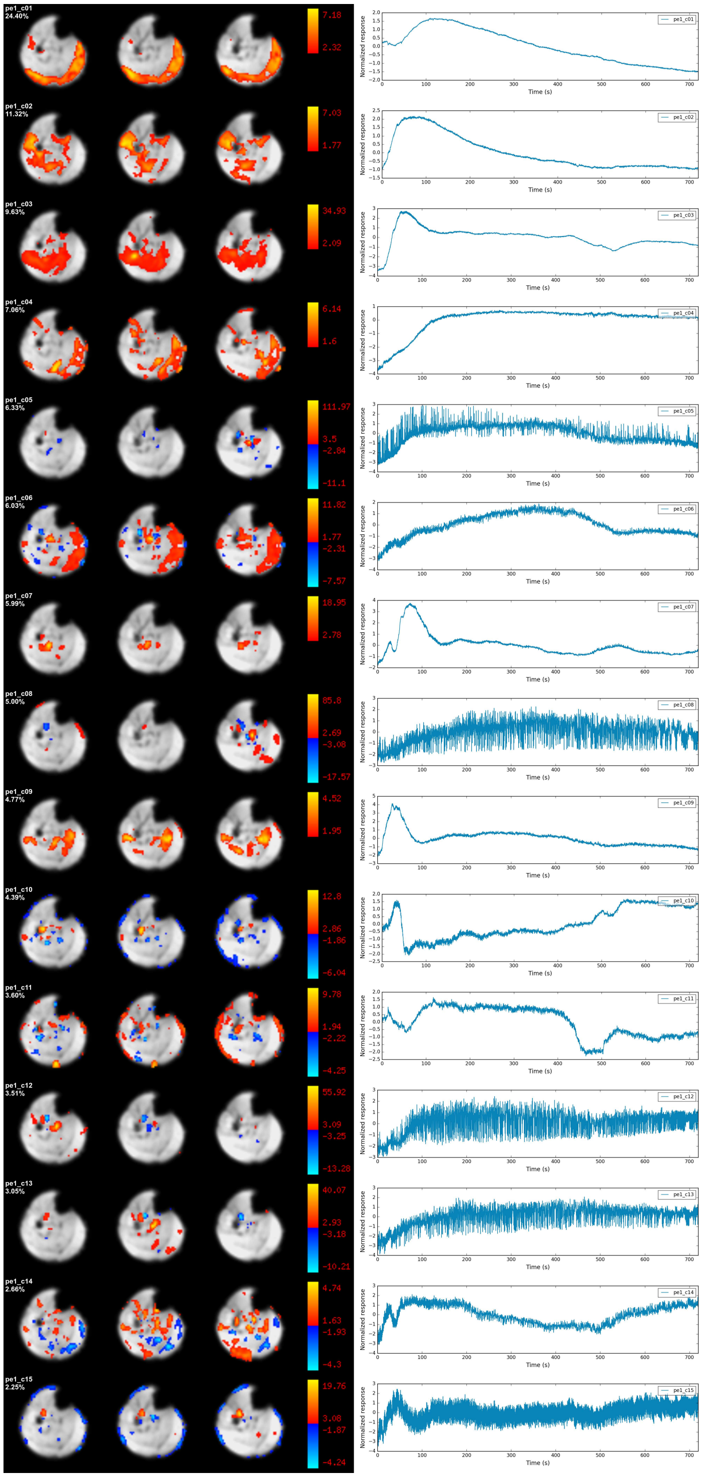

Figure 4.35: Trial *subj05_PE1*

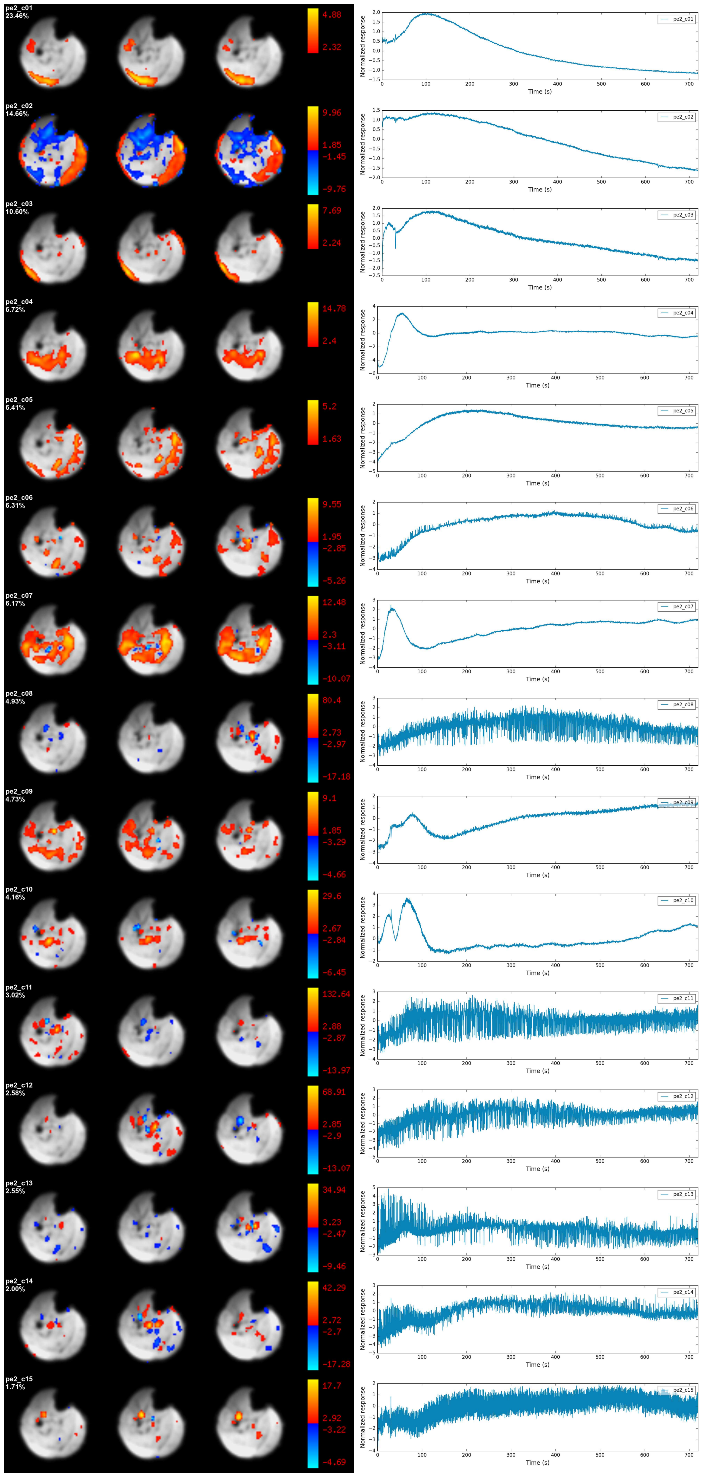

Figure 4.36: Trial *subj05_PE2*

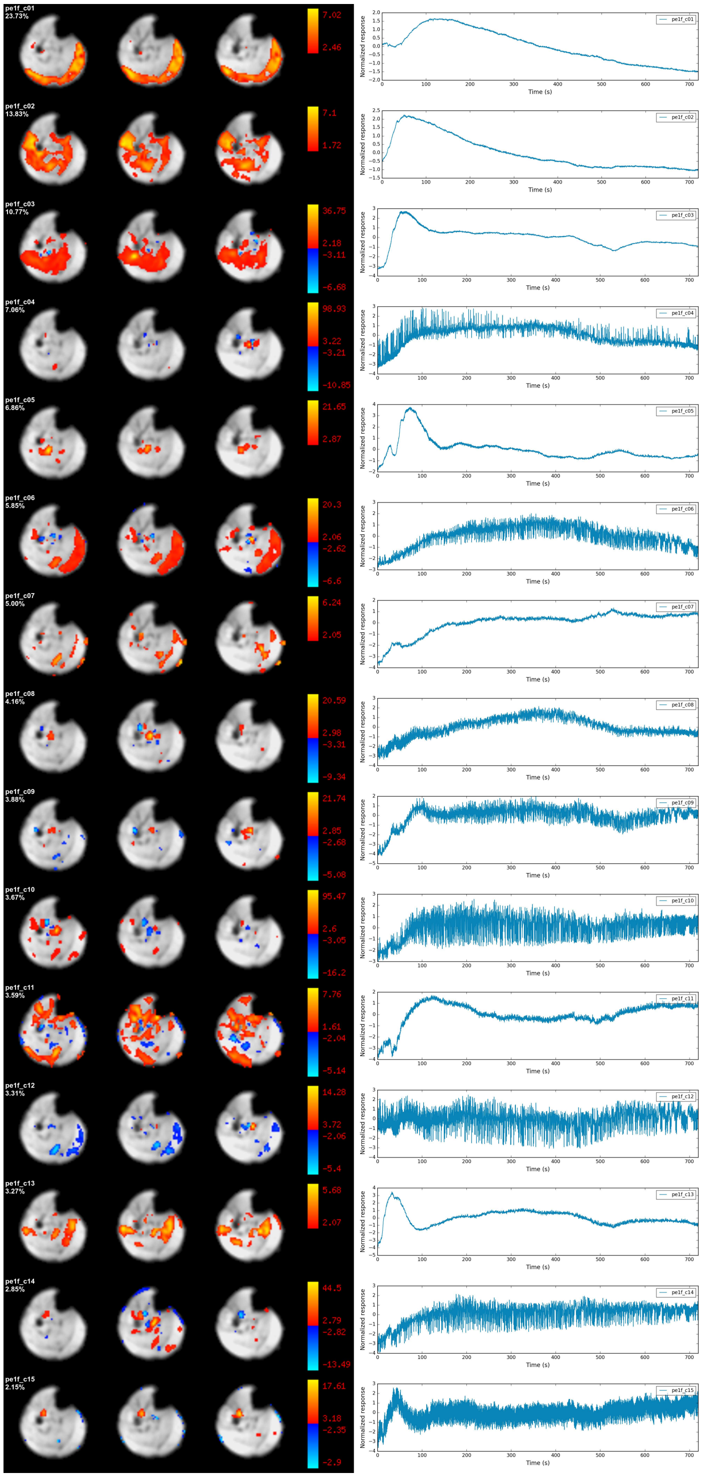

Figure 4.37: Trial *subj05_PE1* filtered, retaining 97.4% of variance

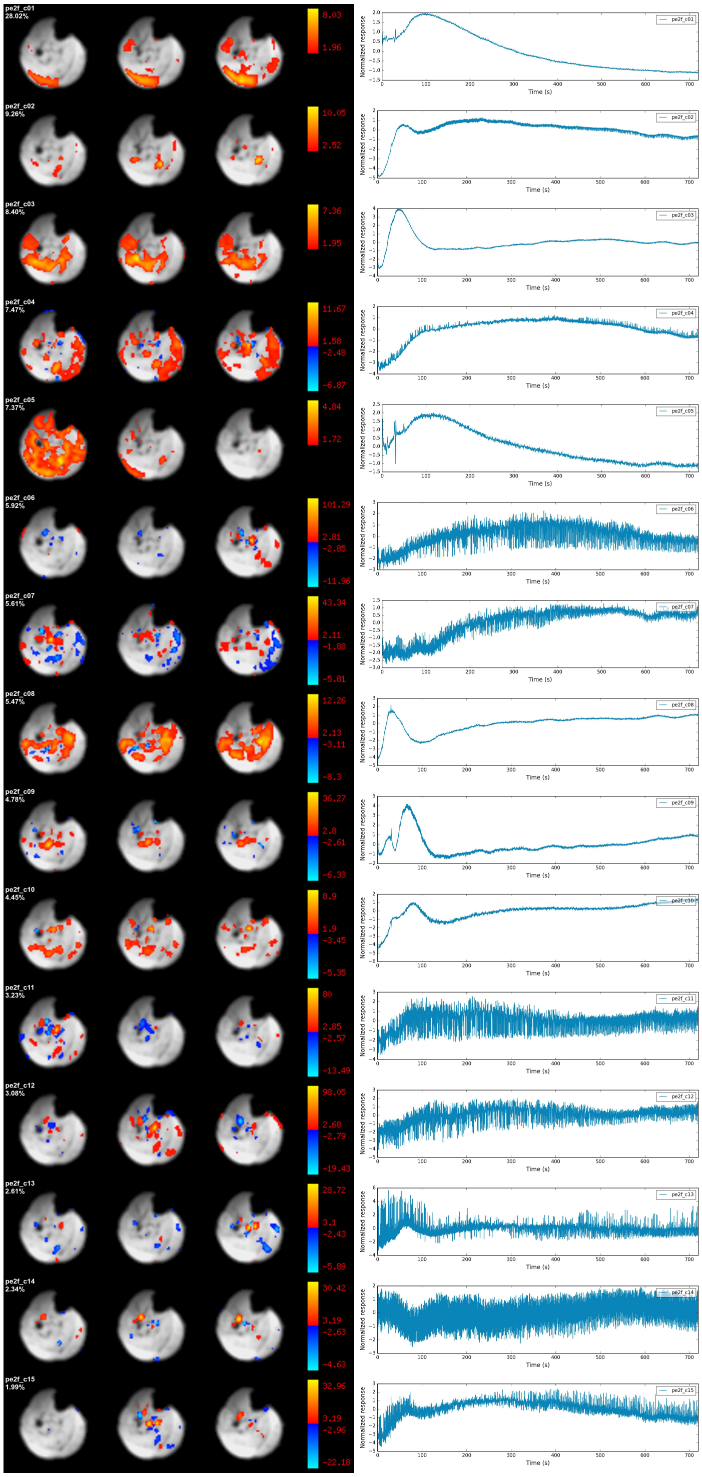

Figure 4.38: Trial *subj05_PE2* filtered, retaining 98.4% of variance

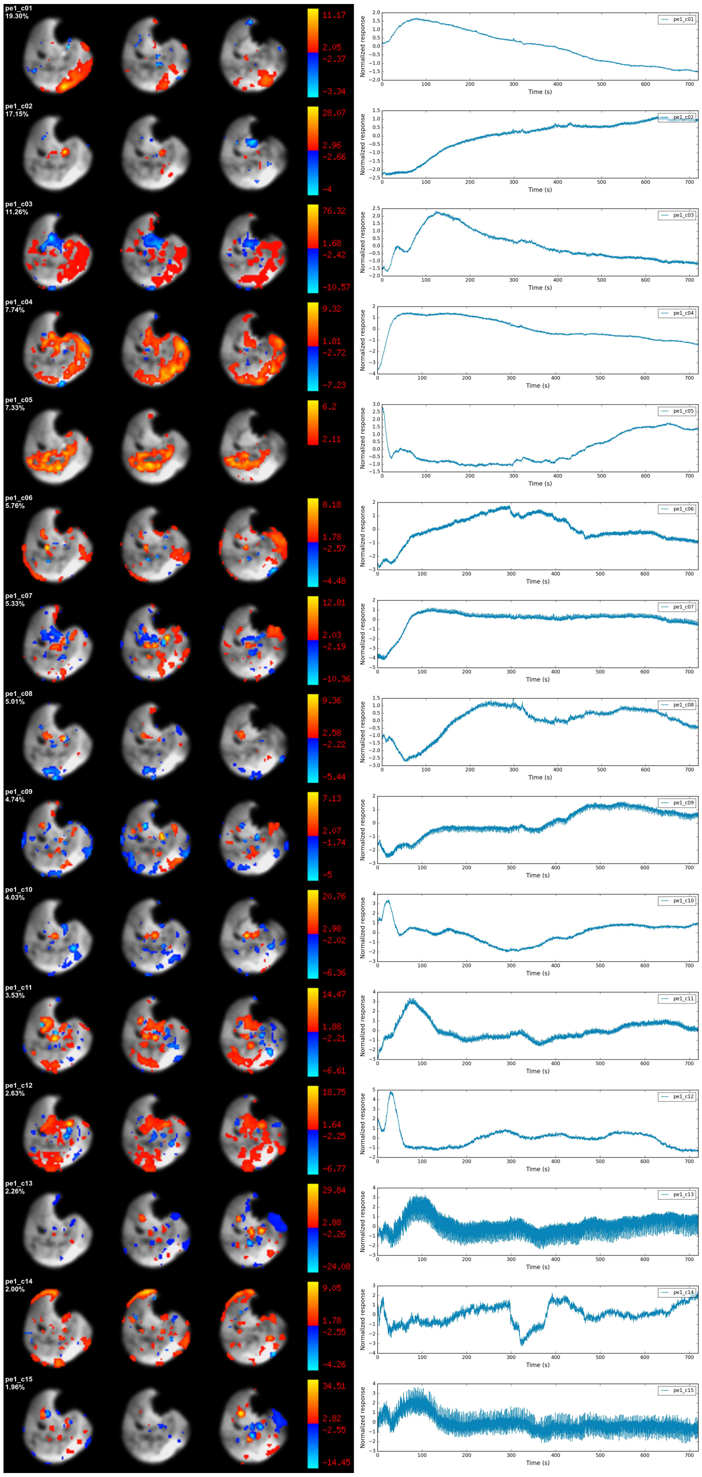

Figure 4.39: Trial *subj06_PE1*

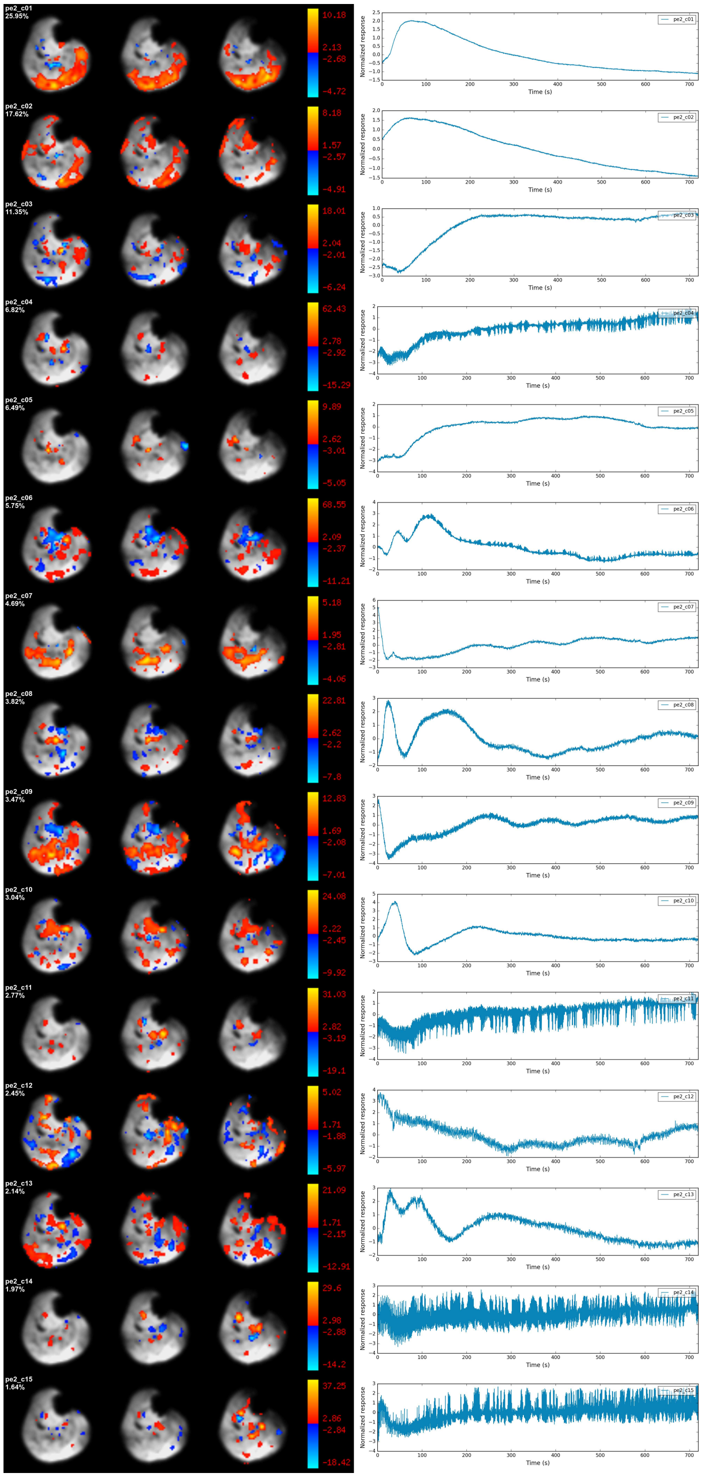

Figure 4.40: Trial *subj06_PE2*

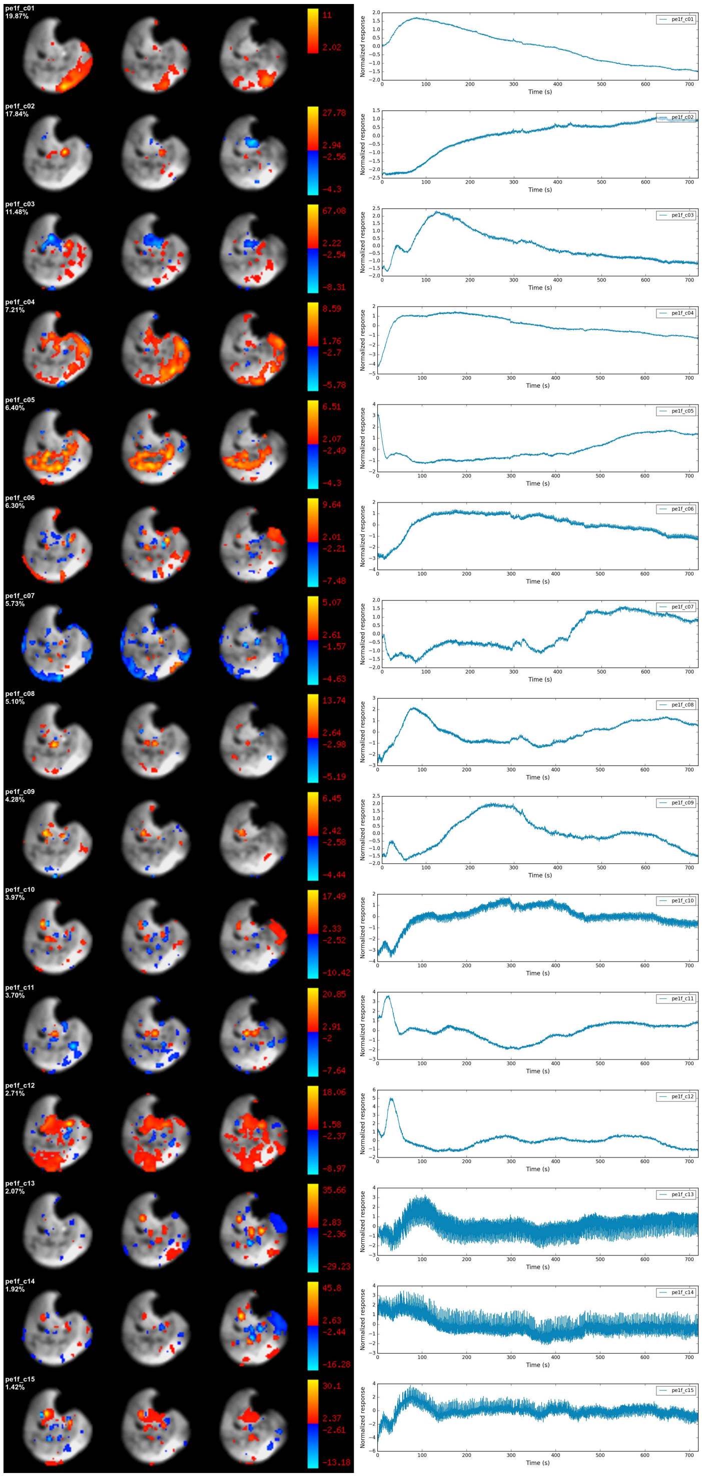

Figure 4.41: Trial *subj06_PE1* filtered, retaining 97.4% of variance

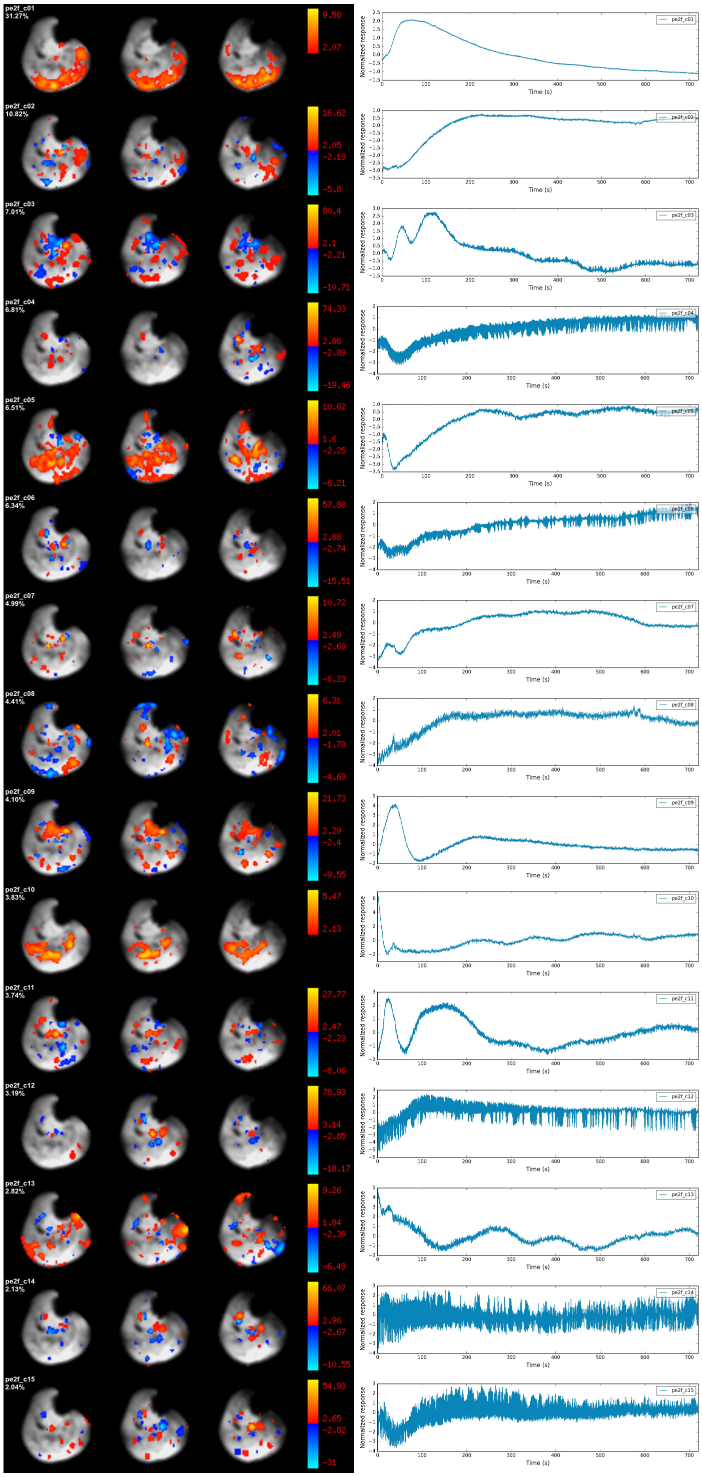

Figure 4.42: Trial *subj06_PE2* filtered, retaining 98.4% of variance

References

Beckmann, C. F. and S. M. Smith. 2004. “Probabilistic independent component analysis for functional magnetic resonance imaging.” *IEEE Trans Med Imaging* 23: 137–152.

Buxton, R. B. 2009. *Introduction to Functional Magnetic Resonance Imaging: Principles and Techniques.* 2nd edition. Cambridge, UK: Cambridge University Press.

Carlier, P. G., D. Bertoldi, C. Baligand, C. Wary, and Y. Fromes. 2006. “Muscle blood flow and oxygenation measured by NMR imaging and spectroscopy.” *NMR Biomed* 19: 954–967.

Caterini, J. E., A. H. Elzibak, E. J. S. Michel, B. W. McCrindle, A. N. Redington, S. Thompson, M. D. Noseworthy, and G. D. Wells. 2015. “Characterizing blood oxygen level-dependent (BOLD) response following in-magnet quadriceps exercise.” *MAGMA* 28: 271–278.

Cox, R. W. 1996. “AFNI: software for analysis and visualization of functional magnetic resonance neuroimages.” *Comput Biomed Res* 29: 162–173.

Damon, B. M., J. L. Hornberger, M. C. Wadington, D. A. Lansdown, and J. A. Kent-Braun. 2007. “Dual gradient-echo MRI of post-contraction changes in skeletal muscle blood volume and oxygenation.” *Magn Reson Med* 57: 670–679.

Damon, B. M., D. M. Wigmore, Z. Ding, J. C. Gore, and J. A. Kent-Braun. 2003. “Cluster analysis of muscle functional MRI data.” *J Appl Physiol* 95: 1287–1296.

Davis, A. D. and M. D. Noseworthy. 2013. “Haemoglobin-derived curve fitting to post-exercise muscle BOLD data.” In “Proc Int Soc Magn Reson Med Sci Meet Exhib,” volume 21, p. 1648.

Davis, A. D. and M. D. Noseworthy. 2016. “Motion and distortion correction of skeletal muscle echo planar images.” *Magn Reson Imaging* 34: 832–838.

Friston, K. J., S. Williams, R. Howard, R. S. Frackowiak, and R. Turner. 1996. “Movement-related effects in fMRI time-series.” *Magn Reson Med* 35: 346–355.

Griffanti, L., G. Salimi-Khorshidi, C. F. Beckmann, E. J. Auerbach, G. Douaud, C. E. Sexton, E. Zsoldos, K. P. Ebmeier, N. Filippini, C. E. Mackay et al. 2014. "ICA-based artefact removal and accelerated fMRI acquisition for improved resting state network imaging." *Neuroimage* 95: 232–247.

Hara, Y. 2008. "Deep venous thrombosis in stroke patients during rehabilitation phase." *Keio J Med* 57: 196–204.

Hyvärinen, A. and E. Oja. 2000. "Independent component analysis: algorithms and applications." *Neural Netw* 13: 411–430.

Jacobi, B., G. Bongartz, S. Partovi, A.-C. Schulte, M. Aschwanden, A. B. Lumsden, M. G. Davies, M. Loebe, G. P. Noon, S. Karimi, J. K. Lyo, D. Staub, R. W. Huegli, and D. Bilecen. 2012. "Skeletal muscle BOLD MRI: From underlying physiological concepts to its usefulness in clinical conditions." *J Magn Reson Imaging* 35: 1253–1265.

Jutten, C. and J. Herault. 1991. "Blind separation of sources, part i: An adaptive algorithm based on neuromimetic architecture." *Signal Process* 24: 1–10.

Kinugasa, R., Y. Kawakami, and T. Fukunaga. 2005. "Muscle activation and its distribution within human triceps surae muscles." *J Appl Physiol* 99: 1149–1156.

Klein, S., M. Staring, K. Murphy, M. A. Viergever, and J. P. Pluim. 2010. "Elastix: a toolbox for intensity-based medical image registration." *IEEE Trans Med Imaging* 29: 196–205.

Ledermann, H.-P., A.-C. Schulte, H.-G. Heidecker, M. Aschwanden, K. A. Jäger, K. Scheffler, W. Steinbrich, and D. Bilecen. 2006. "Blood oxygenation level-dependent magnetic resonance imaging of the skeletal muscle in patients with peripheral arterial occlusive disease." *Circulation* 113: 2929–2935.

Meissner, M. H. 2005. "Lower extremity venous anatomy." *Semin Intervent Radiol* 22: 147–156.

Muller, M. D., Z. Li, C. T. Sica, J. C. Luck, Z. Gao, C. A. Blaha, A. E. Cauffman, A. J. Ross, N. J. Winkler, M. D. Herr et al. 2016. "Muscle oxygenation during dynamic plantar flexion exercise: combining BOLD MRI with traditional physiological measurements." *Physiol Rep* 4: e13004.

Noseworthy, M. D., A. D. Davis, and A. H. Elzibak. 2010. "Advanced MR imaging techniques for skeletal muscle evaluation." *Semin Musculoskelet Radiol* 14: 257–268.

Otsu, N. 1979. "A threshold selection method from gray-level histograms." *IEEE Trans Syst Man Cybern* 9: 62–66.

Partovi, S., A.-C. Schulte, B. Jacobi, M. Klarhöfer, A. B. Lumsden, M. Loebe, M. G. Davies, G. P. Noon, C. Karmonik, L. Zipp, G. Bongartz, and D. Bilecen. 2012. "Blood oxygenation level-dependent (BOLD) MRI of human skeletal muscle at 1.5 and 3 T." *J Magn Reson Imaging* 35: 1227–1232.

Potthast, S., A. Schulte, S. Kos, M. Aschwanden, and D. Bilecen. 2009. "Blood oxygenation level-dependent MRI of the skeletal muscle during ischemia in patients with peripheral arterial occlusive disease." *Rofo* 181: 1157–61.

Power, J. D., K. A. Barnes, A. Z. Snyder, B. L. Schlaggar, and S. E. Petersen. 2012. "Spurious but systematic correlations in functional connectivity MRI networks arise from subject motion." *Neuroimage* 59: 2142–2154.

Power, J. D., K. A. Barnes, A. Z. Snyder, B. L. Schlaggar, and S. E. Petersen. 2013. "Steps toward optimizing motion artifact removal in functional connectivity MRI; a reply to carp." *Neuroimage* 76: 439–441.

Rockel, C. and M. D. Noseworthy. 2016. "An exploration of diffusion tensor eigenvector variability within human calf muscles." *J Magn Reson Imaging* 43: 190–202.

Satterthwaite, T. D., M. A. Elliott, R. T. Gerraty, K. Ruparel, J. Loughead, M. E. Calkins, S. B. Eickhoff, H. Hakonarson, R. C. Gur, R. E. Gur et al. 2013. "An improved framework for confound regression and filtering for control of motion artifact in the preprocessing of resting-state functional connectivity data." *Neuroimage* 64: 240–256.

Schulte, A.-C., M. Aschwanden, and D. Bilecen. 2008. "Calf muscles at blood oxygen level-dependent MR imaging: aging effects at postocclusive reactive hyperemia." *Radiology* 247: 482–489.

Smith, S. M., M. Jenkinson, M. W. Woolrich, C. F. Beckmann, T. E. J. Behrens, H. Johansen-Berg, P. R. Bannister, M. D. Luca, I. Drobnjak, D. E. Flitney, R. K. Niazy, J. Saunders, J. Vickers, Y. Zhang, N. D. Stefano, J. M. Brady, and P. M. Matthews. 2004. "Advances in functional and structural MR image analysis and implementation as FSL." *Neuroimage* 23 Suppl 1: S208–S219.

Torricelli, A., V. Quaresima, A. Pifferi, G. Biscotti, L. Spinelli, P. Taroni, M. Ferrari, and R. Cubeddu. 2004. "Mapping of calf muscle oxygenation and haemoglobin content during dynamic plantar flexion exercise by multi-channel time-resolved near-infrared spectroscopy." *Phys Med Biol* 49: 685.

Towse, T. F., J. M. Slade, J. A. Ambrose, M. C. DeLano, and R. A. Meyer. 2011. "Quantitative analysis of the postcontractile blood-oxygenation-level-dependent (BOLD) effect in skeletal muscle." *J Appl Physiol* 111: 27–39.

Towse, T. F., J. M. Slade, and R. A. Meyer. 2005. "Effect of physical activity on MRI-measured blood oxygen level-dependent transients in skeletal muscle after brief contractions." *J Appl Physiol* 99: 715–722.

Van der Walt, S., J. L. Schönberger, J. Nunez-Iglesias, F. Boulogne, J. D. Warner, N. Yager, E. Gouillart, and T. Yu. 2014. "scikit-image: image processing in Python." *PeerJ* 2: e453.

Van Dijk, K. R., M. R. Sabuncu, and R. L. Buckner. 2012. "The influence of head motion on intrinsic functional connectivity MRI." *Neuroimage* 59: 431–438.

Van Leeuwen, B., G. Barendsen, J. Lubbers, and L. De Pater. 1992. "Calf blood flow and posture: Doppler ultrasound measurements during and after exercise." *J Appl Physiol* 72: 1675–1680.

Wigmore, D. M., B. M. Damon, D. M. Pober, and J. A. Kent-Braun. 2004. "MRI measures of perfusion-related changes in human skeletal muscle during progressive contractions." *J Appl Physiol* 97: 2385–2394.

Zhao, J. M., C. S. Clingman, M. J. Närväinen, R. A. Kauppinen, and P. van Zijl. 2007. "Oxygenation and hematocrit dependence of transverse relaxation rates of blood at 3T." *Magn Reson Med* 58: 592–597.

Chapter 5

Conclusions and future directions

Researchers have endeavoured to use muscle gradient echo (GRE) echo planar imaging (EPI) data to study people with diseases such as peripheral vascular disease (PVD) and diabetes (e.g. Ledermann et al., 2006; Slade et al., 2011), and athletes (Stacy et al., 2016). These studies differentiate atypical subjects from healthy controls. The literature associated with these studies has lacked a clear methodology for dealing with motion and distortion in skeletal muscle images. There was also a lack of any description of the spatial uniformity of the signal within a muscle following exercise, especially following an extended exercise protocol as opposed to single contractions. The research described in this thesis has helped to fill this void by providing tools for preprocessing and a scheme for analysis of the data.

5.1 Main findings

This thesis has presented three research chapters that detail aspects of a strategy for the analysis of skeletal muscle GRE EPI images. The analysis approach has been very different in each chapter, but each one has in some way addressed the effects of motion as a confound to the time series signal.

The work in Chapter 2 was motivated by the fact that prior studies examining skeletal muscle GRE EPI data have either used preprocessing tools intended for brain images (e.g. Schewzow et al., 2013), or they avoided discussion of image preprocessing steps, such as motion correction, entirely (e.g. Towse et al., 2011). The chapter revealed limitations in the existing software tools and described replacements developed to improve preprocessing techniques on muscle GRE EPI data. In particular, it was demonstrated that conventional motion correction tools can actually introduce spurious motion in the time series of images. This resulted from the apparent motion of the bright inflowing arterial blood, an artifact that occurred due to the interaction of flow and magnetic resonance imaging (MRI) gradients. A cost function masking scheme for the motion correction registration was described and implemented, which greatly improved the results. A fieldmap unwarping scheme was also implemented that reduced distortion and improved the registration of EPI and structural images. This work and the software developed should prove useful for researchers to improve preprocessing in future skeletal muscle imaging studies.

Chapter 3 was centred around a motion-related artifact that occurs in GRE EPI images after exercise. Previous studies have briefly noted this artifact, but managed it only by treating affected time points as missing data and removing them from analysis (e.g. Towse et al., 2011). The chapter included a description of the origins of the artifact, as it results from the recovery of longitudinal magnetization. This occurs because tissue leaves and re-enters the imaged volume during muscle contractions. It also included a method for exploiting the artifact to map the motion that caused it. First, this work provides a resource to explain the nature of the artifact for future researchers who will inevitably encounter the large, rapid signal change and wonder whether it has a physiological origin. Given the explanatory model for the signal change, the work also provides a rationale for removing the rapid signal change from the data using regression of a mono-exponential curve. Finally, the technique may prove useful for motion mapping by researchers already performing GRE EPI muscle studies.

Chapter 4 included an examination of the post-exercise GRE EPI signal using a multivariate approach. Previous studies have mostly extracted signals with single regions of interest (ROIs) selected from muscle tissue, assuming that it represented an entire muscle (e.g. Partovi et al., 2012). Prior studies have also directly modelled the resultant signal without considering whether motion played a role in generating it (e.g. Damon et al., 2007). Our previous abstract has revealed local differences in signal spectral content due to the presence of vessels (Davis and Noseworthy, 2011). The research in Chapter 4 has revealed the spatial maps and temporal dynamics of the vascular signal within the body of a muscle. Previous authors, such as Partovi et al. (2012), have generally noted that they avoided vessels visible in structural scans when defining their ROIs. However, the results of Chapter 4 revealed that the signal effects of vessels are spatially extensive due to T_2^* weighting of the signal, even from vessels small enough that they were not visualized in structural scans prior to exercise. The work also revealed major differences in signal temporal characteristics between muscles involved in the exercise (gastrocnemius and soleus), though differences were not found within the muscle tissue of a particular muscle that was not near a vessel.

Furthermore, motion has not really been investigated as a confound to analysis of muscle GRE EPI images before. Chapter 4 presented an argument that motion in most subjects was highly correlated with the post-exercise signal, but was still not the primary *cause* of signal variance. Overall, the probabilistic independent component analysis (PICA) method of analysis was shown to provide valuable insights with GRE EPI muscle data. The fact that the method is able to extract regions of interest closely resembling the muscle and vessel boundaries in the leg is an indicator of quality, considering the underlying software was given no prior information about the data in question, and was developed for brain functional magnetic resonance imaging (fMRI). A major strength of a multivariate approach such as independent component analysis (ICA) is that it takes into account spatial correlations in the data without making assumptions about an underlying model. The ICA method gave consistent results from each subject, with multiple components from various areas of the leg exhibiting similar temporal and spatial characteristics. The gastrocnemius muscle and the vessels it contains gave especially consistent results. The method can be applied to subjects with various disease states to assess how the spatial maps and time courses change compared to healthy controls. A limitation of this study is that the subject cohort was relatively small, and consisted of healthy male young adults. A study of subjects with PVD would need to confirm the results demonstrated here in a healthy cohort that is age-matched to the subject population. A larger field-of-view in the inferior-superior direction would also be desirable in PVD subjects, to reveal local areas of inadequate blood supply.

5.2 Future directions

Group results Though the results in Chapter 4 demonstrate reliable results from the PICA method between and within subjects, the act of selecting, collating and comparing components generated by separate runs of the software is labour intensive and somewhat subjective. This limits the feasibility of larger group studies following the same scheme. In brain studies, this challenge is addressed by registering all subjects to a common spatial template (normalization). Then functional data may be temporally concatenated to generate a common set of group-level components, and a dual-regression approach is used to generate subject level maps (Zuo et al., 2010). This allows for direct comparison of component maps within or among subject populations, with the knowledge that what's being compared is truly shared. In muscle, however, the registration scheme upon which the dual-regression method rests has never been developed, and would face significant challenges due to the high variance in size and shape of the lower leg muscles between individuals. This is a potential avenue for research.

Curve fitting The temporal signal associated with the ICA components extracted is of interest to those who would model the signal and attempt to glean physiological information from the blood oxygenation level dependent (BOLD) signal, which is known to be sensitive to perfusion, oxygenation, and blood volume. Analysis schemes that fit curves to the GRE EPI time series data help to define curve shape parameters and standardize reporting of results (e.g. Schewzow et al., 2013; Davis and Noseworthy, 2013a). However, without an underlying model, such strategies do not aid in physiological interpretation of the signal. Our previous abstract began development of a scheme for curve fitting a model based on oxygenation and blood volume, regularized by the curve shapes evident from near-infrared spectroscopy (NIRS) data (Davis and Noseworthy, 2013b). Further development of this strategy is warranted, and would benefit from the addition of ICA to define components for fitting.

Spatial and temporal independence The ICA method used in Chapter 4 generates components representing spatial maps, and it is over these spatial representations that independence is sought. No restrictions are placed on the time courses, so the temporal components associated with spatial maps may be highly correlated

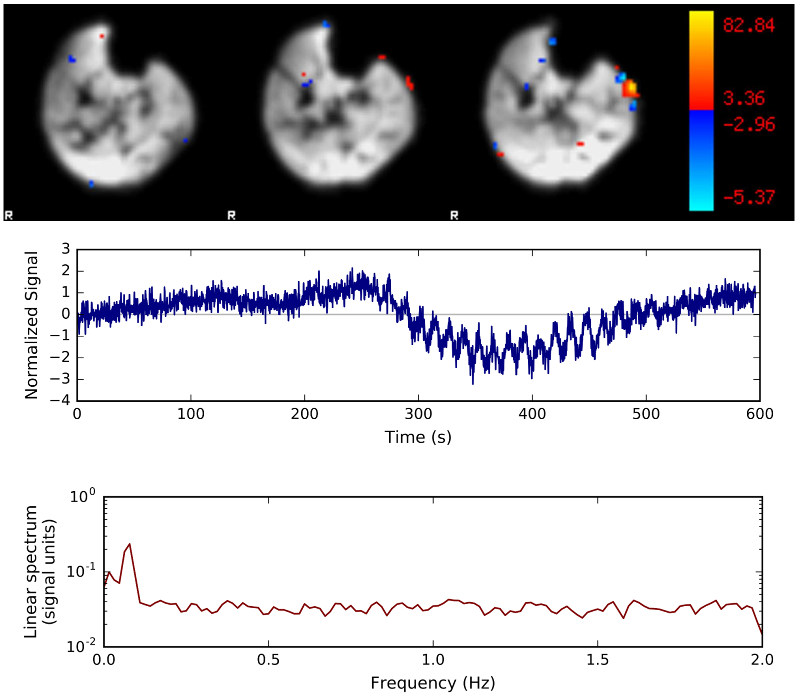

Figure 5.1: Periodic signal at 0.1 Hz. This component came from *rest* data in Subject 4, session 2. It contains a periodic signal evident in a small, superficial ROI, likely a vessel. The power spectrum has a peak near 0.08 Hz. The statistical map represents thresholded z-scores with alternative hypothesis testing at $p > 0.5$.

with one another, as long as they are not perfectly temporally synced (Beckmann and Smith, 2004). Indeed, some of the components within runs represented in the plots of Section 4A.4 are very similar in qualitative shape, having mostly differences in timing. If a model fitting scheme is to be applied to the temporal signal, it may be beneficial to examine the temporal independence of the data as well. This may be done after identifying a region of interest with spatial ICA. Temporal ICA is not possible in *Melodic*, but is implemented in the *GIFT* software package (Medical Image Analysis Laboratory, 2017).

Vascular components Both the rest and post-exercise data-sets yielded components with high power around 1 Hz, and spatial maps mapping mainly to blood vessels. Such components presumably reflect cardiac pulsatility and are unlikely to be of much interest to researchers. Other vascular components observed in resting state ICA bear further investigation. For example, Component 62 of *subj04_r2* had a striking sinusoidal component in a small superficial area, likely a vein (Fig. 5.1).

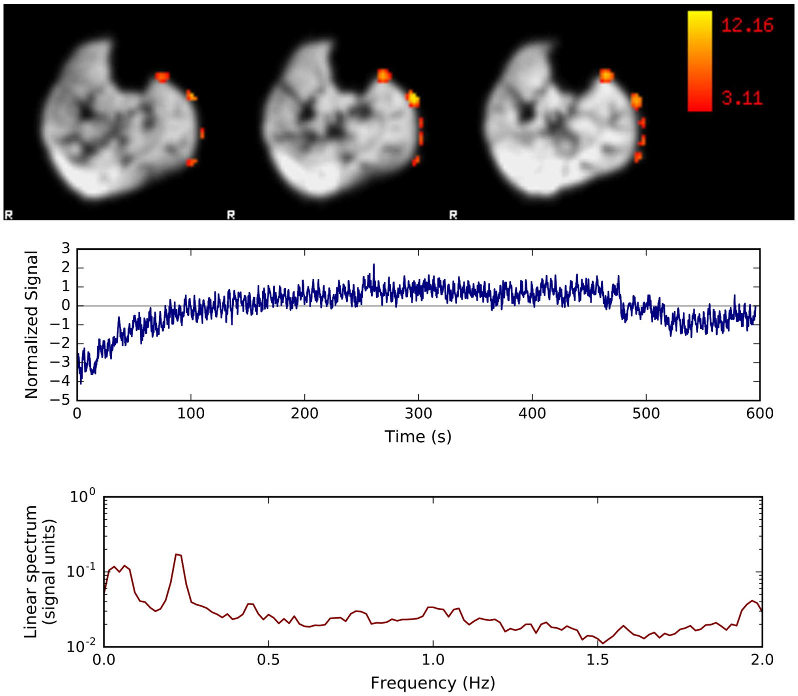

Figure 5.2: Periodic signal at 0.2 Hz. This component shows a sinusoidal signal in multiple superficial vessels, with power near 0.23 Hz. The data source was *rest* data in Subject 4, session 1.

Similar components were also seen in the *r1* results from this subject, with the sinusoid occurring at approximately 0.1 Hz. A study employing laser doppler flowmetry (LDF) indicated that the likely origin of the signal is the intrinsic myogenic activity of vascular smooth muscle (Kvandal et al., 2006). Oscillations in that frequency range have previously been detected with fMRI in the brain, as well as optically during surgery (Rayshubskiy et al., 2014).

When analyzing *subj04_r1* with 15 components, a 0.2 Hz signal was identified in the vasculature (Fig. 5.2), which has also been observed previously by optical means (LDF) (Benditt et al., 1995)). Such signals may be of interest to researchers since they are difficult to record from whole leg cross sections by other means. Temporal filtering of the data is likely required to detect the signals reliably. Extracting fewer components from the *rest* data set would improve the practicality of the method as well, since searching through 300–400 component results per subject is very time consuming.

5.3 Concluding remarks

Interest in performing GRE EPI studies of muscle in health and disease continues to increase (Noseworthy et al., 2010; Tonon et al., 2012). To date, the analysis techniques used in most studies have manually delineated regions of interest from muscles and examined the resulting signals. The work in this thesis represents an improvement to analysis methodology that will help to remove the effects of motion and reveal the physiological signals of interest. This study has also revealed that healthy muscles can have very different curve shapes resulting from the same exercise, making it difficult to predict exactly what a *healthy* muscle response looks like, as differentiated from an unhealthy one. The independent component analysis technique used here represents a data-driven way to reveal the underlying physiological response features in GRE EPI muscle data that should prove useful in examining unhealthy subject populations.

References

Beckmann, C. F. and S. M. Smith. 2004. "Probabilistic independent component analysis for functional magnetic resonance imaging." *IEEE Trans Med Imaging* 23: 137–152.

Benditt, D. G., M.-Y. Chen, R. Hansen, J. Buetikofer, and K. Lurie. 1995. "Characterization of subcutaneous microvascular blood flow during tilt table-induced neurally mediated syncope." *Journal of the American College of Cardiology* 25: 70–75.

Damon, B. M., J. L. Hornberger, M. C. Wadington, D. A. Lansdown, and J. A. Kent-Braun. 2007. "Dual gradient-echo MRI of post-contraction changes in skeletal muscle blood volume and oxygenation." *Magn Reson Med* 57: 670–679.

Davis, A. D. and M. D. Noseworthy. 2011. "Fourier analysis of muscle BOLD data after exercise." In "Proc Int Soc Magn Reson Med Sci Meet Exhib," volume 19, p. 7153.

Davis, A. D. and M. D. Noseworthy. 2013a. "Consistency of post-exercise skeletal muscle BOLD response." In "Proc Int Soc Magn Reson Med Sci Meet Exhib," volume 21, p. 1640.

Davis, A. D. and M. D. Noseworthy. 2013b. "Haemoglobin-derived curve fitting to post-exercise muscle BOLD data." In "Proc Int Soc Magn Reson Med Sci Meet Exhib," volume 21, p. 1648.

Kvandal, P., S. A. Landsverk, A. Bernjak, A. Stefanovska, H. D. Kvernmo, and K. A. Kirkebøen. 2006. "Low-frequency oscillations of the laser doppler perfusion signal in human skin." *Microvascular research* 72: 120–127.

Ledermann, H.-P., A.-C. Schulte, H.-G. Heidecker, M. Aschwanden, K. A. Jäger, K. Scheffler, W. Steinbrich, and D. Bilecen. 2006. "Blood oxygenation level-dependent magnetic resonance imaging of the skeletal muscle in patients with peripheral arterial occlusive disease." *Circulation* 113: 2929–2935.

Medical Image Analysis Laboratory. 2017. "Group ICA/IVA of fMRI toolbox (GIFT) manual." `http://mialab.mrn.org/software/gift/docs/v4.0b_gica_manual.pdf`. Accessed: 2017-08-31.

Noseworthy, M. D., A. D. Davis, and A. H. Elzibak. 2010. "Advanced MR imaging techniques for skeletal muscle evaluation." *Semin Musculoskelet Radiol* 14: 257–268.

Partovi, S., A.-C. Schulte, B. Jacobi, M. Klarhöfer, A. B. Lumsden, M. Loebe, M. G. Davies, G. P. Noon, C. Karmonik, L. Zipp, G. Bongartz, and D. Bilecen. 2012. "Blood oxygenation level-dependent (BOLD) MRI of human skeletal muscle at 1.5 and 3 T." *J Magn Reson Imaging* 35: 1227–1232.

Rayshubskiy, A., T. J. Wojtasiewicz, C. B. Mikell, M. B. Bouchard, D. Timerman, B. E. Youngerman, R. A. McGovern, M. L. Otten, P. Canoll, G. M. McKhann et al. 2014. "Direct, intraoperative observation of ~0.1 hz hemodynamic oscillations in awake human cortex: implications for fmri." *Neuroimage* 87: 323–331.

Schewzow, K., M. Andreas, E. Moser, M. Wolzt, and A. I. Schmid. 2013. "Automatic model-based analysis of skeletal muscle BOLD-MRI in reactive hyperemia." *J Magn Reson Imaging* 38: 963–969.

Slade, J. M., T. F. Towse, V. V. Gossain, and R. A. Meyer. 2011. "Peripheral microvascular response to muscle contraction is unaltered by early diabetes but decreases with age." *J Appl Physiol* 111: 1361–1371.

Stacy, M. R., C. M. Caracciolo, M. Qiu, P. Pal, T. Varga, R. T. Constable, and A. J. Sinusas. 2016. "Comparison of regional skeletal muscle tissue oxygenation in college athletes and sedentary control subjects using quantitative BOLD MR imaging." *Physiol Rep* 4: e12903.

Tonon, C., L. L. Gramegna, and R. Lodi. 2012. "Magnetic resonance imaging and spectroscopy in the evaluation of neuromuscular disorders and fatigue." *Neuromuscul Disord* 22: S187–S191.

Towse, T. F., J. M. Slade, J. A. Ambrose, M. C. DeLano, and R. A. Meyer. 2011. "Quantitative analysis of the postcontractile blood-oxygenation-level-dependent (BOLD) effect in skeletal muscle." *J Appl Physiol* 111: 27–39.

Zuo, X.-N., C. Kelly, J. S. Adelstein, D. F. Klein, F. X. Castellanos, and M. P. Milham. 2010. "Reliable intrinsic connectivity networks: test–retest evaluation using ICA and dual regression approach." *Neuroimage* 49: 2163–2177.